THE UNIVERSITY *of* EDINBURGH

Three-dimensional imaging of bacterial microcolonies

Alexander M^{c} Vey

A thesis submitted in fulfilment of the requirements
for the degree of Doctor of Philosophy
to the
University of Edinburgh
July 2015

Abstract

Previous research into microbial colonies and biofilms shows a significant gap in our current understanding of how bacterial structures develop. Despite the huge body of research undertaken into the formation, genetic makeup, composition, and optimal growth conditions of colonies, no study has been successful in identifying all individual bacteria in a colony in three-dimensions as a function of time. This lack of bacterial cell lineage in such a simple class of organisms is conspicuous in the light of what is known about other organisms, such as *Caenorhabditis elegans* [1]. In this thesis I show that using laser scanning confocal microscopy in conjunction with developments in sample preparation and post acquisition image analysis, it is possible to fully reconstruct all individual bacteria within an *Escherichia coli* (*E. coli*) microcolony grown in viscoelastic media. Additionally, I show that by further pushing the resolution of confocal microscopes, commercial systems are capable of extracting three-dimensional information on protein structures inside bacteria at early stages of growth.

This thesis is in three parts.

The first part shows that by pushing the resolution of a commercial laser scanning confocal microscope system it is possible to achieve single cell resolution of a bacterial colony growing in three dimensions in a viscoelastic medium (agarose) from a seed bacterium. The growth of individual bacteria is examined as the concentration of agarose in the media is altered. Results show there is a nonlinear dependence between the rate of growth of a bacterium and the concentration of the agarose in the media with a peak in growth rate at 3 % (weight) concentrations of agarose in M9 media.

The second part of this work presents a study of how an initially two-dimensional colony growing between a glass slide and agarose gel suddenly invades the third spatial dimension by buckling. The results show that the cells within the centre of the colony flex and buckle, due to confinement by their neighbours, creating additional layers. Indeed, flexing is not limited to the buckling event but occurs throughout the early

growth cycle of a colony.

The final part of this thesis shows that by further pushing the resolution of confocal microscopes, commercial systems are capable of extracting three-dimensional information about the temporal evolution of the spatial distribution of the FtsZ septation ring within the cell. As the bacterial colony grows from a seed bacterium to a microcolony, the error in placing the division accurately at the cell centre is seen to increase as the number of bacteria within the colony increases and spatial confinement occurs.

Declaration

Except where otherwise stated, the research undertaken in this thesis was the unaided work of the author. Where the work was done in collaboration with others, a significant contribution was made by the author.

Alexander M^c Vey
July 2015

Acknowledgements

Firstly, I wish to thank my supervisor Professor Wilson Poon for the assistance and guidance he has provided since the second year of my PhD. Thank you also to Dr Bartek Waclaw and Dr Rosalind Allen for useful discussions and input throughout my studies.

I particularly wish to acknowledge Dr Angela Dawson and Dr Jana Schwarz-Linek for their help and support in all things biological, Dr Alys Jepson for assisting with use of the FLUOstar Optima and analysis of the curves and Dr Job Thijssen and Dr Jochen Arlt for showing me some of the tricks of confocal imaging. I would also like to thank my collaborators in the School of Engineering, Ibrahim Albaijan and Dr Vasileios Koutsos for their atomic force measurements of the Young's modulus of agarose and Dr Diarmuid Lloyd for his enthusiastic interest for bacterial colony measurements, both single cell and otherwise.

I am indebted to the other inhabitants of Room 1510, Dario and Kuba, for providing an interesting place to work and similarly to others on the corridor for allowing me to talk with them when things weren't going as planned. Thank you to my friends in Edinburgh and elsewhere for their interest in my work, genuine or otherwise, and particularly for providing distractions when they were needed. Thank you also to both my parents for their support and for free proof-reading services throughout the writing process.

Finally, thanks to Helen for her support throughout.

Contents

List of Figures

List of Tables

Chapter 1

Introduction

Bacteria are the most prevalent organisms on Earth with a collective terrestrial biomass considerably greater than that of plants and animals combined [2]. They are constantly meeting new environmental conditions and consequently have evolved highly sophisticated ways of adapting and changing. This results in bacteria exhibiting a wide range of attributes, being capable of swimming [3] and collective motion [4], as well as forming complex structures at interfaces [5], and surviving in exceptionally hostile conditions [6–9]. Individual bacteria are also capable of communicating with each other (a process known as quorum-sensing) in order to maximise their chance of survival by collaborating to form more complex multi-cellular structures [10, 11]. Exhibiting such a diverse set of abilities means bacteria are exceptionally useful to humans, in the fermentation of wine [12, 13], cheese [14] and yoghurt [15, 16] and as pesticide [17]. Similarly, bacteria are vital in aiding digestion in the human gut, particularly in releasing vitamins from food [18, 19]. Additionally, as a result of their ability to utilise a wide-range of sources as food, bacteria have also been used to clear oil spills [20] and clean toxic waste [21] as well as producing chemicals such as ethanol and acetone [22] and have recently been found to boost crop production through conversion of nitrogen in the air to a form suitable for rapid growth in trees [23].

Unfortunately, bacteria are also capable of causing great distress and harm to their hosts and are the cause of many infections in plants [24], animals [25] and humans [26]. One of the main determinants of infectivity is their ability to adhere to surfaces, forming colonies and biofilms, which offer increased resistance to drugs (antimicrobials) as a result of the reduction in surface area and the excretion of extracellular polymeric substance (EPS) [27, 28]. The rise in antimicrobial resistance (AMR) of bacteria is increasingly a cause of concern, with the World Health Organisation (WHO) citing it as a significant threat to modern medicine [29]. The report produced by the WHO

into the scale of AMR across the 6 regions of the world shows that in many cases common bacterial infections are resistant to at least one antimicrobial more than 50 % of the time. Many bacteria showing AMR form biofilms as one of their primary methods of combatting antimicrobials, *E. coli* causing urinary tract infections, and *Staphylococcus pneumoniae* causing pneumonia being two examples [30]. Therefore, gaining an understanding of how colonies and biofilms form, their makeup, types of structures, and EPS excretion, as well as the method of nutrient uptake is essential in combatting AMR in bacteria.

The definitions of microcolony, colony and biofilm are somewhat muddled throughout scientific literature. For the purposes of clarity, I will define what I mean when referring to biofilm, colony and microcolony in this thesis. A colony is a single-species structure growing on nutrient rich agarose. Colonies are larger than microcolonies, which refers to the early stages of colony formation. Large colonies are visible by eye but in the context of this thesis both colonies and microcolonies require a microscope in order to visualise them. In contrast, a biofilm is a more complex structure consisting of bacterial cells (often multiple species) as well as extracellular proteins and EPS. Experiments in this thesis deal only with microcolony and very early colony formation to a point beyond the development of secondary layers on the agarose surface.

Unsurprisingly, colonies and biofilms have been a focal point for microbiological research for the last half century, with experiments aimed at probing all aspects of the systems. A significant proportion of biofilm investigation has been centred around obtaining an understanding of the genetic basis of biofilm formation [31], notably in major biofilm models such as *Pseudomonas aerouginosa* [32] and in pathogenically important strains such as *E. coli* [33]. In a similar vein, research has also been conducted into understanding the role of different factors in the environment where biofilms exist. For example, a study by Song *et al.* found that an increase in the concentration of magnesium ions initially led to an increased abundance of bacteria cells attached to a glass surface [34]. The study also found that as the biofilm matured the concentration of magnesium ions did not influence the number of *Pseudomonas fluorescen* cells present in the biofilm, leading Song *et al.* to conclude that magnesium is important for the initial binding of bacteria to a surface but not in the formation of bonds between bacterial cells [34]. Additionally, the mechanical properties of biofilms have been probed by groups such as Hohne *et al.* who investigated the Young's modulus of both *Staphylococcus epidermids* and *Klebsiella pneumoniae* biofilms using a thin poly (dimethyl) siloxane (PDMS) membrane sited above the sample to compress the biofilm. They found the Young's moduli of the biofilms to be 3.2 kPa and 1.1 kPa

respectively [35].

In a concurrent strand of research, rather than focussing on the environment in which biofilms exist, or their genetic makeup, there have been several studies into the identification of the constituent parts of biofilms both spatially and temporally using microscopy. Initially, three-dimensional spatial reconstruction was conducted using electron microscopy (EM) [36]. However, the preparation of samples for EM requires the sample to be fixed and dried either in ethanol for 72 hrs, or in buffer for 2 hrs followed by air at room temperature for 120 hrs [37]. As biofilms are up to 97 % water [38] this produced a very simplistic and unrealistic view of biofilm makeup in early studies [39]. To image hydrated samples in a more realistic environment, it was necessary for new methods to be applied, and with extensive application already in biology, confocal microscopy was an obvious candidate. Lawrence *et al.* were the first group to successfully image fully hydrated microbial biofilms using confocal microscopy. They were able to resolve individual bacterial cells in the biofilm in three-dimensions when the cells were well dispersed. But, as the density of the bacterial cells increased, they were unable to resolve individuals successfully [40]. In their concluding remarks Lawrence *et al.* state their belief that optical techniques such as confocal microscopy will be of sufficient resolution to allow full "3D, and potentially 4D (time course) reconstructions of biofilm characteristics" [40]. Unfortunately, despite more than two decades passing since Lawrence *et al.* made this statement, the realisation of this prediction has yet to occur [41–43]. Caldwell *et al.* attempted to further improve this method, resolving individual cells, however, they were, like Lawrence, only able to identify individual cells in the biofilm when they were well dispersed in the EPS [44].

In the study by Song *et al.* mentioned above [34], the group used confocal microscopy to image the three-dimensional distribution of cells as the biofilm formed. Although their confocal images successfully show dense collections of bacterial cells in the body of the biofilm, they appeared unable to resolve individual bacteria at a sufficient resolution to successfully track individuals in the biofilm as a function of time. Similarly, Lakins *et al.* used multiphoton microscopy to identify areas of live and dead bacterial cells within the biofilm but found that the intensities required to image at this level caused necrosis to the bacteria cell [45]. However, they were able to selectively remove bacteria in the biofilm by using the laser to ablate a section of the whole [45].

In two papers published at the beginning of this decade, a collaborative group from Taiwan used phase contrast and laser scanning confocal microscopy to identify individual bacteria grown on a viscoelastic surface. The studies, focussing on early

colony formation [46] and larger colony growth [47], were able to successfully visualise individual bacteria in densely formed colony structures but appeared unable to extract quantitative information from these images, relying instead on arguments of total colony expansion to determine growth models of these systems [46, 47]. Similarly, last year, Grant *et al.* used confocal microscopy to image bacterial colonies grown on viscoelastic media (agarose gels) around the point where they develop into three-dimensional structures (with the generation of a second layer of bacteria) [48]. Again, despite being able to identify individual bacteria in the images, the group relies on colony area expansion as a whole rather than individual bacterial growth to show that mechanical forces are the main driving force for developing a second layer [48].

Recently, Berk *et al.* successfully reconstructed biofilms in three spatial dimensions as a function of time using laser scanning confocal fluorescence microscopy. They used four different fluorescent markers to identify different constituent cells in biofilms, identifying cell clusters and protein concentrations in the biofilm. The study showed that rather than being individual cells surrounded by EPS in a biofilm, bacteria form in dense, tight-knit clusters with constant widths of $2.2 \pm 0.3\,\mu m$ and lengths from $2\,\mu m$ to $8\,\mu m$ [49]. Berk *et al.* also found evidence that no bacterium in these clusters was entirely surrounded by other bacteria, meaning that all bacteria were able to directly absorb nutrients from the EPS and surroundings without nutrients needing to pass across other bacteria. However, none of the studies discussed above have proved to be capable of identifying individual bacteria in the biofilm environment, particularly when the cells are densely packed together in clusters.

Stewart *et al.* successfully identified individual bacteria in a colony and used this to track the growth of individual cells over time [50]. They showed a clear increase in the growth rate over several generations for *E. coli* originating from the newly formed pole (formed in the most recent septation) when compared to cells which originated from an old pole (formed in an earlier division). However, despite being successful in temporally tracking the bacteria over several generations, the group did not extract spatial information on the colony formation and development [50].

When compared to other similar fields of research this deficiency is quite conspicuous. In *Caenorhabditis elegans*, a small roundworm used as a model eukaryotic system, for example, the location of all cells within the worm was identified as early as the 1980's culminating in Sulston *et al.* in 1983 successfully providing a full cell lineage of all cells from embryonic state to fully hatched larva [1]. There are several factors that have led to the inability to provide a cell lineage for bacterial colonies, one of which is

the close proximity of the diffraction limit to the physical size of individual bacteria, particularly along the optical axis. In this thesis I show that, despite the dimensions of bacteria being very close to the diffraction limit of optical microscopes, using confocal microscopy it is possible to successfully identify single bacteria (micron sized particles) in a microcolony (densely packed system) in three spatial dimensions and discuss some of the resulting information that can be obtained from tracking the growth of such systems as they develop from disperse individuals to fully formed colonies. Additionally, I show that by pushing the resolution of confocal microscopy further it is possible to image structures within micron sized bacteria in three spatial dimensions as a function of time.

The thesis structure is as follows:

Chapter 2 sketches the theory of confocal microscopy and its application to bacterial imaging.

Chapter 3 outlines the specifics of sample preparation and confocal microscopy that are used for experiments in this thesis.

Chapter 4 details the developments made to the confocal microscopy protocols and in image acquisition and processing in order to achieve single bacterial resolution within microcolonies in three-dimensions.

Chapter 5 describes results of experiments conducted to determine physical parameters of the seed bacterium used to initiate colony growth for these experiments.

Chapter 6 evaluates the effectiveness of confocal microscopy in the reconstruction of bacterial colonies where central bacteria are confined in all directions by the coverslip, agarose and adjacent bacteria.

Chapter 7 provides results of the development of confocal microscopy to image at a sub cellular level, namely the FtsZ protein in a single bacterium, and in bacteria in a microcolony.

The results I present have relevance to many disparate disciplines. The following section is included here to seek to facilitate the reader in identifying those aspects of most relevance to them. Microbiologists, for example, will be especially interested in Chapters 5, 6 and 7 where I show that using confocal microscopy, a technique

already widely used in the field, it is possible to obtain far more detailed information from the technique than is extracted in current studies. The results, particularly those in Chapter 5 and 6, show more complicated systems, such as multiphoton microscopy [51], are not necessary in order to extract quantitative information on the spatial and temporal properties of micron sized cells. Similarly, the microbiology community interested in protein formations in bacterial cells, and who conduct single cell measurements on bacteria, will be interested in the results showing that colony growth changes the distribution of protein structures in individual bacteria. This is of particular relevance since almost all microbiology groups focus on isolated bacteria, not the predominant state for natural bacteria which prefer to collect together to form colonies or biofilms.

The study of complex bacterial formations is also of particular interest to medical biologists treating antimicrobial resistant bacteria, as many pathogens form colonies and biofilms. Being capable of fully reconstructing the spatial and temporal properties of cells within colonies and biofilms using confocal microscopy, (Chapter 6), will offer increased insight into many pathogens which use these mechanisms as a way of resisting treatment when inhabiting a host (patient).

Additionally, since equilibrium thermodynamic theory is now largely a complete body of work [52, 53], since the end of the 19th century efforts in thermodynamics have been focussed on systems which are removed from equilibrium [54, 55]. In condensed matter physics there is therefore a requirement for model systems which are out of equilibrium in order to test the resulting theories. A system is in thermodynamic equilibrium when the free energy of the system is at a minimum. There are three ways in which systems out of equilibrium can be produced. Firstly, a system in thermodynamic equilibrium can be driven out of equilibrium from a single exertion of force and the relaxation of the system back to equilibrium can be observed. Secondly, a system in thermodynamic equilibrium can be continually driven away from equilibrium by an external force and the adaptation of the system probed. Thirdly, a system which is intrinsically out of equilibrium, through chemical reactions or the flux of energy or of matter, can be observed directly. Bacteria, like most systems found in nature, are intrinsically out of thermodynamic equilibrium and as such are an excellent model for studies of this sort. Therefore, extracting spatial information from bacterial colonies as a function of time is vital if bacteria are to be used to test non-equilibrium theory.

Chapter 2

Three dimensional imaging techniques

2.1 Introduction

There are several methods of generating three-dimensional (3D) images, many of which have been used extensively in biological systems. Many, such as ultrasound [56, 57], computerised tomography (CT) [58], magnetic resonance imaging (MRI) [59, 60] and positron emission tomography (PET) [61–64] have found uses in clinical environments [65]. However, the resolution of these techniques ranges from tens of microns to a few millimetres [66–72] meaning that while they are suitable for organ and human cell study they are not suitable for bacterial cellular studies. Two techniques that do offer suitable resolution for imaging bacterial cells are atomic force microscopy (AFM) and electron microscopy (EM). The improved resolution, both being of the order of nanometers [73, 74], means the techniques can probe samples at the required length scale for bacterial cultures but both methods are limited to surface (AFM) or near surface (EM) investigations due to the short penetration depth obtainable from the probes [65]. Additionally, as previously discussed, the protocol used for EM sample preparation leads to oversimplified and unrealistic models of biological samples [39].

With developments in light microscopy, there are now many methods for achieving optical resolution on the micrometre scale, and therefore of obtaining 3D information from living biological samples (commonly known as sectioning) through optical microscopes. These include confocal microscopy, and nonlinear microscopy methods such as multi-photon fluorescence [51], second-harmonic generation [75] and coherent anti-Stokes Raman scattering [51]. Nonlinear microscopy methods are so called because in order to cause an excitation of the sample (and therefore induce a signal photon from

the sample) two or more photons have to be incident on the sample at the same time and spatial location, which means that nonlinear optical methods are inherently 3D. Since the excitation of the sample can only occur at very high concentrations of input photons (the photons must be incident on the sample within 10^{-18} seconds and within $\lesssim \lambda^3$ of each other [76]), in practice, the excitation is limited to a very tight focal spot in the sample [77]. Unfortunately, the laser systems and optical setup required to generate nonlinear signals are complex to construct, maintain and operate, especially as there are very few examples of off-the-shelf commercial systems capable of producing these signals. Additionally, as a result of needing two or more photons to be incident on the sample in order to produce a signal, the peak power of light focussed on the sample either needs to be relatively high ($10^{20} - 10^{30}$ photons/cm^2 for two-photon microscopy [76]) when compared to linear microscopy methods, or the excitation must occur over a longer period of time (i.e. the dwell time must be far longer). High laser powers are unfavourable when imaging biological samples, as they lead to photodamage and necrosis (death) of the sample. Similarly, reducing the peak power of the laser and imaging the sample over extended periods of time in order to obtain a suitable signal intensity, is inconvenient when examining live biological samples due to variations over time, particularly in growth and division. This is especially evident when examining bacterial samples, which in optimal growth conditions have a generation time of around 30 min. Consequently, nonlinear optical microscopy techniques are still limited in their application to biological samples, especially when high time resolution is desired.

In contrast, laser scanning confocal microscopy is a widely available commercial microscope technique which offers many of the advantages of nonlinear microscopy techniques, such as three-dimensional capability, while reducing the complexity of the system for the user. After an initial delay from when Marvin Minsky first showed confocal microscopy was capable of sectioning a sample [78, 79], the technique has become extensively used in the imaging of biological samples, particularly since the combination of the technique with laser scanning technology in the late 1980's [80, 81]. In this chapter I outline the physical principles associated with laser scanning confocal fluorescence microscopy.

2.2 Confocal fluorescence microscopy

2.2.1 Overview

Conventional microscopy techniques, such as brightfield, darkfield and phase-contrast are powerful methods of imaging samples on the microscopic scale. In a traditional

microscope the sample is placed on a translational stage and light is projected onto it from a collimated beam; the sample being viewed through an objective placed on the other side of the sample stage. In microscopy of this sort, the entire sample is illuminated continuously during imaging meaning light from areas of the sample other than the focal plane is also directed through the objective and viewed at the image plane (Figure 2.1). Out of focus light (red and blue light rays in Figure 2.1) distorts the image, reducing the quality, and means that brightfield microscope methods are incapable of resolving objects in the third spatial dimension (along the optical axis).

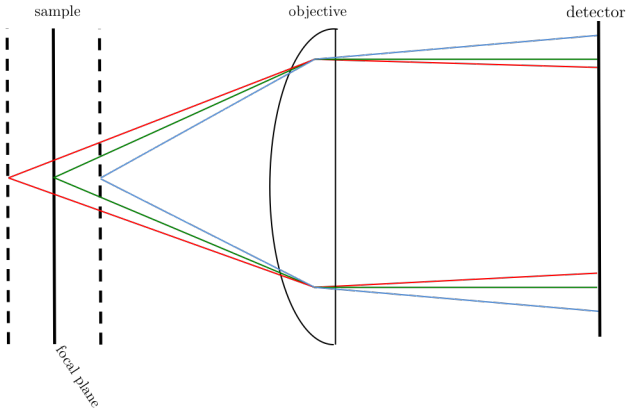

Figure 2.1: Schematic of light rays from brightfield imaging incident on detector. Light from planes not in the focal plane (red and blue) are incident on the detector as well as light from the focal plane (green) causing noise and distorting the image.

Despite this, brightfield microscopy systems are capable of reaching the fundamental diffraction limit in the object plane

$$r_{\mathrm{xy}} = 0.61\frac{\lambda}{\mathrm{NA}} \tag{2.1}$$

where λ is the wavelength of the incident light and NA is the numerical aperture of the objective, defined as

$$\mathrm{NA} = n\sin\theta \tag{2.2}$$

where n is the refractive index of the imaging media between the objective and the sample (air, water or oil usually) and θ is half the angle of the cone of light that can enter the objective.

The diffraction limit, (Eq. 2.1), is a fundamental limit which determines how close two objects can be to one another and still be resolvable. It cannot be improved upon in conventional microscope techniques, such as brightfield. Two objects close to one

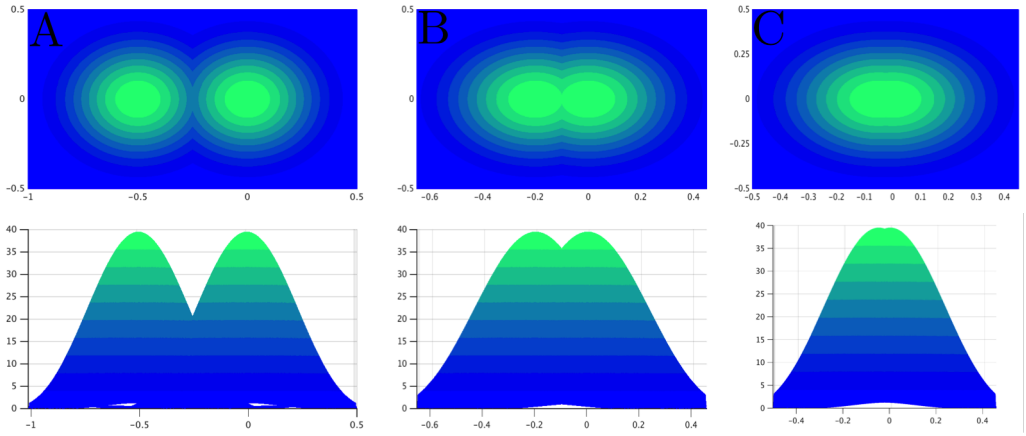

Figure 2.2: Schematic of two point sources emitting diffraction patterns (known as Airy disks) with accompanying intensity profiles (bottom images). At distances far larger than the diffraction limit (r_{xy}) the two objects are easily distinguishable from each other (A). As the distance between objects approaches r_{xy} (B) the distinction becomes more difficult. (C) when two objects are separated by a distance less than r_{xy} the two diffraction patterns interfere, making separation of the two objects impossible (they are unresolvable). All axes are arbitrary units

another in a sample can be viewed as independent point sources of light, which are brought to a focus through the objective. Light from each of these point sources, when passing through the objective, is diffracted, creating a diffraction pattern. For a point source this takes the form of a collection of Airy rings (Figure 2.2). If the two point sources are well separated in the sample it is still possible to identify (resolve) the two individual objects (A). However, as the distance between the objects approaches r_{xy} (B), the diffraction patterns overlap, causing interference in the two patterns. When objects are separated by a distance less than r_{xy} (C), the objects are indistinguishable.

In confocal microscopy, like brightfield, the entire sample is illuminated by the incident light source [80]. However, unlike brightfield microscopy, the incident light is focussed through an objective onto the sample in a tight focal spot,[1] effectively illuminating the sample from a point source rather than a collimated beam of light. This increases the resolution in the focal plane (the lateral resolution) by a theoretical factor of 1.525, a value obtained by dividing the constant in Eq. 2.1 with that in Eq. 2.3 [82]. The lateral resolution of confocal microscopes ($r_{confocal}$) is therefore

$$r_{confocal} = 0.4\frac{\lambda}{NA} \tag{2.3}$$

[1]The focal spot and plane are in fact thin three-dimensional volumes of light limited by diffraction.

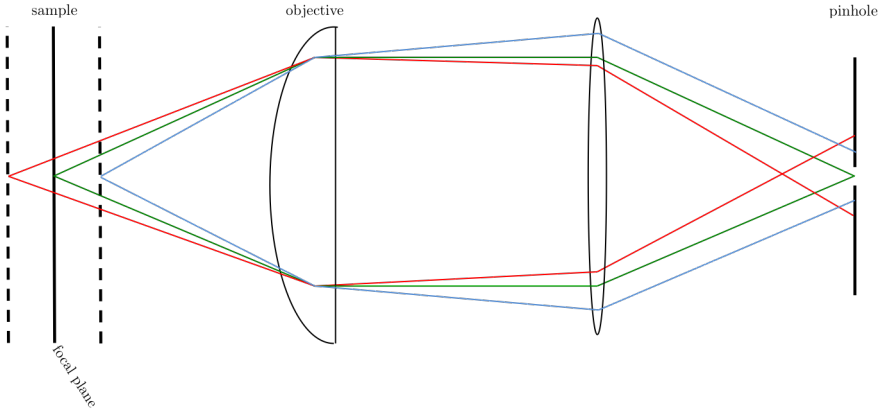

Figure 2.3: Schematic of light rays from confocal imaging. The introduction of a pinhole means that light generated at the focal spot (green) is the only light able to pass through to the detector. Light generated away from the diffraction-limited focal spot (red and blue) is cut off by the pinhole.

However, as with brightfield, a relatively large volume is illuminated in the sample and is incident on the detector. In order to reduce the noise from out of focus light, in confocal microscopy a pinhole (of the correct diameter) is positioned between the objective and the detector at the conjugate focal plane of the objective, stopping out of focus light from entering the detector and limiting the light to a small optical section of the focal volume (Figure 2.3), providing a point-like detection mechanism. Unsurprisingly, the size of the optical volume incident on the detector is heavily dependent upon the diameter of the pinhole [83]. The introduction of a point-like illumination and point-like detection means that using this method it is possible to specifically select a small three-dimensional plane in the sample for precise imaging. But, in order for confocal microscopes to achieve improvements in the resolution limit it is necessary for the incident light to be spatially coherent. One of the simplest methods of achieving this is through the use of coherent light sources such as lasers.

2.2.2 Laser scanning confocal microscopy

Most confocal systems which are commercially available utilise laser radiation to excite the sample due to laser radiation's inherent spatial coherence and the ability to focus easily to tight focal spots. Additionally, using raster scanning mirrors the beam can be scanned quickly across the sample moving the focal spot around the focal (xy) plane to illuminate different areas of the sample, therefore allowing the detector, usually a photomultiplier tube (PMT), to build up an image of the sample one pixel at a time. Similarly, by altering the distance between the sample stage and the objective, by moving the objective (or the sample) up or down the optical axis (also known as the

axial or z direction), it is possible to transfer the focal plane of the incident light through the sample, providing the ability to optically section a sample in three-dimensions.

Figure 2.4 shows a schematic of the confocal microscope used for experiments conducted as part of this thesis. Incident light (blue) from the laser source is brought to a focus on the sample through the objective. Before being brought to a focus on the sample, scanning mirrors allow rapid scanning of the focal spot in the xy plane. The emitted

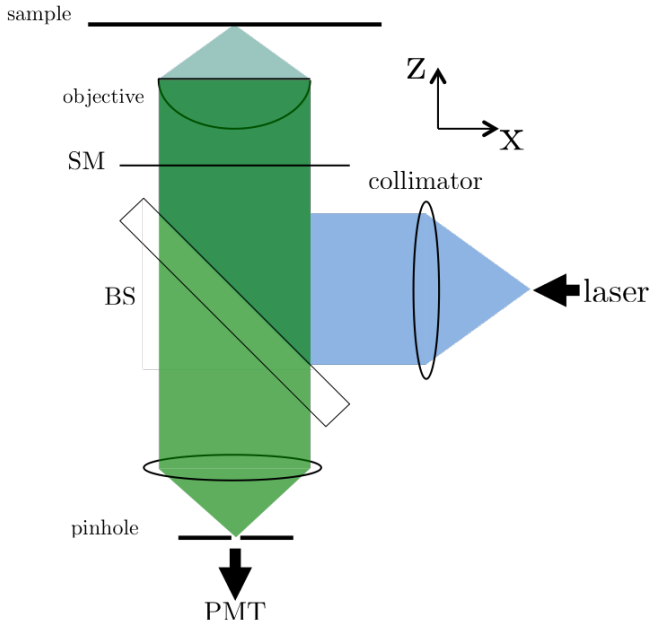

Figure 2.4: Schematic of the confocal microscope setup used for three-dimensional optical sectioning of bacteria and bacterial colonies as part of this thesis. Incident light (blue) of specific wavelength is directed into the microscope body and brought to a focus on the sample through an objective. Emitted light (green) from the sample is collected through the objective and passes through the bandpass filter before being brought to a focus again on the conjugate focal plane. A pinhole placed at the conjugate focal plane stops light not from the focal plane from entering the PMT. A beamsplitter (BS) allows simultaneous acquisition of two different wavelengths in two PMTs. Rapid scanning of the scanning mirrors (SM) translates the focal spot across the xy plane allowing acquisition of an image by the PMT one pixel at a time. The objective can be moved in the axial direction (z) in order to allow alteration of the focal plane through the sample, providing the capability for optical sectioning of the sample. Specific alterations to the setup are discussed in the relevant results chapters.

light is reflected back through the objective and directed through the pinhole onto a PMT.

However, as Eq. 2.1 shows, the resolution of microscopes is of the order of hundreds of nanometres (taking the wavelength of incident light, λ, to be 500 nm (central in the

visible spectrum) and with an NA of 1.4 the resolution in the focal plane is $r_{xy} \simeq 220\,\text{nm}$). The resolution of optical microscopes being so close to the physical size of a bacterium means resolving individuals in a densely packed population is a nontrivial task, *E. coli* for example, have a diameter of 800 nm and range from 1.0 µm to 10.0 µm in length.

2.2.3 Resolution of confocal microscopy

While the lateral resolution of brightfield microscopes is sufficient, given a high enough magnification objective ($> 40\times$), to resolve individual cells the lack of axial resolution means the technique is unsuitable for full 3D reconstruction. Given that the resolution of optical microscopes is of the order of hundreds of nanometres, a full consideration of the limits of resolution of a confocal microscope is necessary.

Lateral resolution

For incident light of wavelength 500 nm through an objective with NA = 1.4, the lateral resolution of a confocal microscope is 145 nm. The improvement in resolution in the focal plane, whilst only a small improvement over brightfield, is still advantageous as it increases the difference between the physical size of an *E. coli* bacterium and r_{confocal}. This improvement is not exclusive to confocal microscopy but is the result of using point-like illumination [84]. Consequently, identifying individual cells in the focal plane (2D) is also possible in a conventional microscope adapted for fluorescent imaging [85].

Despite the improvement in the lateral resolution, caused by focussing of the incident light onto the sample, when objects are separated by a distance below the improved resolution (i.e. smaller than 145 nm), it is still possible for them to be indistinguishable. Figure 2.5 shows two fluorescent beads (Tetraspeck) with a diameter of 200 nm imaged using a Zeiss Confocal LSM 700. As with brightfield imaging, when the two objects (beads in this case) are separated by a distance well above the diffraction limit, 145 nm, (A), they are clearly resolvable. However, as the distance between the objects approaches 145 nm it becomes more difficult to distinguish individual beads from one another (B), until two beads separated by a distance below the diffraction limit of 145 nm (C) are indistinguishable.

2.2.4 Axial resolution of confocal microscopes

The real advantage of confocal microscopy is the ability to resolve in the axial direction (along the optical axis) through the positioning of a pinhole at the conjugate focal plane, which allows only light from the focal plane to be directed onto the detector.

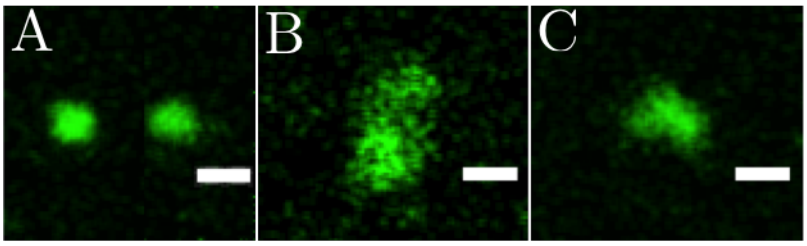

Figure 2.5: Two Tetraspeck fluorescent beads of diameter 200 nm imaged using a Zeiss confocal LSM 700. Beads well spatially separated within the sample are easily distinguishable (A). However, as the separation between the two beads, $l \rightarrow r_{\text{confocal}}$ (B) it becomes more difficult to resolve the individual beads from one another until the beads are too close together ($l < r_{rmconfocal}$) and are no longer separable from one another (C). Scale bars are 500 nm

The axial resolution ($\Delta z_{\text{confocal}}$) is dependent upon the diameter of the pinhole, but can be estimated as

$$\Delta z_{\text{confocal}} \simeq \frac{n\lambda}{2\text{NA}^2} \tag{2.4}$$

where n is the refractive index of the sample medium, λ the incident wavelength and NA the numerical aperture of the objective [86]. This is the theoretical maximum axial resolution and assumes a pinhole with an infinitely small diameter, implying an infinitely small number of photons pass through the pinhole onto the detector. Consequently, the resolution of the microscope in the axial direction will not reach this level of resolution. However, assuming incident light of wavelength 500 nm on a largely aqueous sample ($n \simeq 1.33$) and imaging with an objective with a numerical aperture of 1.4, the greatest possible resolution in the axial direction is $\Delta z_{\text{confocal}} \simeq 170$ nm. The resolution in the axial direction is therefore approximately 4 times smaller than the minimum dimension of an *E. coli* bacterium (diameter $\simeq 800$ nm), meaning that, while very close to the fundamental resolution of a confocal microscope, it is possible, at least in principle, to resolve individual bacteria in the axial direction.

2.2.5 Pinhole

The diameter of the pinhole is critical in providing resolution along the optical axis. If the diameter of the pinhole is very large a confocal microscope reverts to a fluorescence microscope and axial resolution is lost. To achieve the theoretical maximum improvement in resolution for confocal microscopy the pinhole must be infinitely small, a physical impossibility. Since the pinhole limits the amount of light that is incident on the detector by removing light from areas of the sample not in the focal plane, an infinitely small diameter means the amount of light passing through

the pinhole (and therefore the signal incident on the detector) is infinitely small. Consequently, in practice a compromise is made between the diameter of the pinhole and the amount of light incident on the detector with the pinhole being set to a finite diameter which is typically equal to the size of the 1st order airy disk created by the diffraction of the system [87].

2.3 Maximising the resolution

A purely theoretical study of confocal microscopy suggests that the lateral and axial resolution (Eqs. 2.3 and 2.4) is suitable for imaging micron sized bacterial cells in three-dimensions. However, in reality the resolution achievable by confocal microscopes is poorer than the theoretical limits, due to both the optical elements in the sample and, more importantly, the media, (glass slide and the biological samples themselves) through which imaging occurs. Theoretical models assume optical elements such as lenses and mirrors are perfectly manufactured. In reality these elements introduce aberrations to the image, which are the result the variation of a lenses refractive index as a function of wavelength and the geometry of the optical element. The former is negated by using a monochromatic light source (such as a laser beam), but aberrations from the geometry of the optical element still occur. In the lateral direction these aberrations can be corrected through careful alignment and precision engineering of the optical elements (mirrors, filters and lenses) used in the construction of the microscope, so that the microscope resolution reaches the fundamental limit of diffraction. However, in the axial direction in particular the resolution is heavily dependent upon the changes in refractive index of the materials the light passes through.

Matching the refractive indices of materials through which the incident and emitted light must travel in order to illuminate the sample and be collected by the detector limits the effect of reflection and refraction at surface interfaces. One of the simplest ways of achieving this is through the use of oil, water or air specific microscope objectives, selected depending upon the nature of the sample under investigation. Air, water and oil have different refractive indices (1, 1.33 and approximately 1.4 respectively) and as such provide a way to match the refractive index of the objective to the initial interface in the sample, limiting the distortion of incident light by reflection or refraction at the barrier between the two materials. For example, samples which are unsealed and open to the environment are best viewed through an air objective in order to limit the number of interfaces through which the incident light must travel. Similarly samples which require an aqueous environment, in order to maintain hydration, for example, are best viewed with a water immersion objective and samples which require sealing or

imaging through a glass coverslip or slide are best viewed with an oil immersion lens, with the refractive index of the oil selected in order to match the refractive index of the objective or the initial glass interface of the sample. As well as limiting refraction and reflection of incident light at the interface, index matching of the objective in oil allows higher valued numerical apertures to be utilised (i.e. increasing the angle of the light cone the objective can focus) providing increased magnification of the sample.

While it is possible to match the refractive indices from the objective to the sample when imaging into living biological samples, in order for light to be brought to a focus at a point within the sample (rather than at the sample surface), the incident light must travel through part of the biological sample. Biological samples are highly disperse (light scattering)[2] and as a result the distance the incident light can travel through the sample without scattering (known as the mean free path of the light) is small. Consequently, imaging deep into biological samples (beyond the mean free path length) means there is an increased probability the incident light will scatter multiple times, reducing the light incident from the focal spot and increasing the probability that light from out-of-focus planes can pass through the pinhole and onto the detector. Figure 2.6 shows a schematic confocal set up where light from the focal spot is scattered in such a way as to restrict it from passing through the pinhole onto the detector (A). Similarly light from an out of focus plane in the sample can be directed towards the pinhole as a result of scattering in the sample (B). Both these scattering events mean there is a degradation in the quality of the image, which increases as the amount of biological material through which light must pass increases [89, 90]. These scattering events empirically decrease the resolution of confocal microscopes from the theoretical maximum 170 nm to 320 nm for dispersive media such as biological samples. Consequently, the distance between objects that the confocal microscope can resolve is only twice as small as the diameter of a bacterial cell. Therefore, although theoretically possible, in order to successfully perform optical sectioning of bacterial colonies in three-dimensions at single cell resolution it is necessary to push the resolution of confocal microscope systems to the limit.

2.4 Aim

The primary aim of this thesis is to develop the scope of confocal microscopy as an imaging tool for microbial systems in three dimensions, which has been achieved through a three-pronged approach (Table 2.1). Firstly, high-contrast 3D imaging

[2]Indeed an entire field of study utilises this phenomenon to its advantage (see [88] for a recent review)

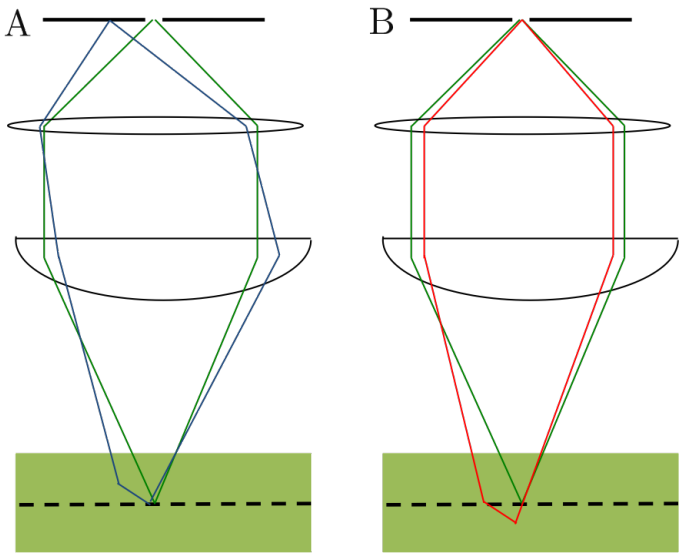

Figure 2.6: Scattering events in a biological sample when imaging with a confocal microscope. (A) Light (blue) from the focal plane of the sample is scattered within the sample and directed away from the pinhole reducing the signal from the focal plane on the detector as a result. (B) Light (red) from an out of focus plane within the sample is scattered in such a way as to direct the light through the pinhole and onto the detector increasing the noise and distorting the signal from the focal plane.

of single bacteria has been conducted in order to show the suitability of confocal microscopy as a method of imaging bacteria at a single-bacterium (and indeed sub-bacterium) resolution. Secondly, imaging of dense single layers of bacterial colonies close to a surface has been undertaken and finally full reconstruction of 3D bacterial colonies is achieved, showing the suitability of confocal microscopy to image densely packed 3D structures with sub-micron resolution.

Approach	Description	Chapter
High-contrast single-bacterium imaging	Maximising resolution of confocal microscopy to image bacterial colonies at single cell resolution and protein superstructures in a bacterium when in isolated and colony growth states	5 and 7
Single-layer dense system imaging	Probing maximum resolution of confocal microscopy to resolve individual bacteria which are in a tight packing formation (colony)	5 and 6
3D reconstruction	Reconstruction of 3D systems when tightly packed	6

Table 2.1: Summary of approach used throughout thesis to develop confocal microscopy for imaging of bacterial systems

Chapter 3

Methods

3.1 Introduction

The study of bacterial colonies has previously been undertaken in our group and many protocols for the preparation of bacteria for colony samples have already been developed [91]. In order to allow comparison between studies the protocols used for experiments in this thesis mirror those already established as much as possible, however, since the theoretical limit of resolution of confocal microscopy is very close to the physical size of single bacterial cells, it is imperative the protocols used to prepare bacterial colonies and to image them are optimised. It has therefore been necessary to adapt some of the current protocols used in the group. In this chapter I outline the general microbiology protocols used for experiments in this thesis and describe the basic confocal microscope set up.

3.2 Sample preparation

In order to obtain comparable data from the imaging of bacterial colonies it is vital that the preparation of bacteria used to seed a colony grown in viscoelastic media is reproducible. To achieve this, strict protocols must be followed, both on the initial growth of bacteria on working plates (plates grown from frozen stock and containing colonies of bacteria grown from a single cell and stored at 4 °C) and on the subsequent growth of these colonies in bulk (liquid media) to bring them into the exponential growth phase, in order to ensure the seed bacteria used to start the colony growth are in the same phase of growth between experiments.

3.2.1 Growth media

For all experiments, bacterial cultures were transferred from frozen stocks (stored at −80 °C) and plated onto petri dishes containing Luria-Bertani (LB) agar, where they were allowed to grow for a period of 16 hrs at 37 °C, resulting in visible, individual colonies being present on the plate. These working plates were then stored in the fridge (at 4 °C) and individual colonies removed and added to liquid media to grow into the exponential growth phase. This is done by picking an individual colony from the working plate and transferring it to a 10 ml liquid growth media solution, which is incubated overnight at 37 °C and shaken in order to allow thorough mixing of the solution. Once the culture has reached the stationary growth phase, 100 µl of the liquid culture is transferred into 10 ml of fresh liquid media and incubated to allow the bacteria in the sample to reach exponential phase.

Once the working plates have been prepared, in order to limit the degradation of the chromosome, and protein structures in the bacteria, each plate is kept for periods not exceeding 3 weeks, as is standard in the biology laboratories in our group. It was seen under the microscope that bacteria grown from plates kept beyond 3 weeks exhibited an increased tendency to form filamentous bacteria (where septation and division do not correctly occur, resulting in extended bacteria filaments beyond the normal 10 µm length).

For both liquid growth media and agarose pads[1] used in the sample chamber (§3.2.3, p. 26) a derivative of M9-glucose media was used. Both LB and M9 media provide a suitable nutrient environment to allow normal colony growth, but the content of LB media is poorly defined and varies across samples as a result of the extraction of LB from bovine serum. In contrast M9 medium is very well defined and therefore is far more reproducible than other media sources. M9 medium is prepared by adding 71.79 ml of de-ionised & distilled (d.d.) water to 25 ml of 4× M9 Salts.[2] The medium is then autoclaved and placed in a warm water bath at 50 °C for 15 min before 2 ml of 20 % glucose is added to the solution, along with 200 µl of 1M $MgSO_4$ and 10 µl of 1M $CaCl_2$. The medium was kept at 50 °C for this step to aid the mixing of $CaCl_2$, which forms a precipitate in the liquid when added at room temperature. For the production

[1] A layer of agarose situated on a microscope slide used to provide nutrients to growing bacteria during experiments.

[2] 4× M9 Salts are a concentrated stock solution containing 30 g Na_2HPO_4, 15 g KH_2PO_4, 2.5 g NaCl and 5 g NH_4Cl added to 750 ml d.d.H_2O. The pH of the solution is adjusted to 7.4 using 10 mol NaOH before topping the solution up to 1 l using d.d.H_2O.

of M9 agarose media, the required weight percent of UltraPure Agarose[3] is added before the solution is autoclaved. A detailed protocol for the production of M9-glucose media, both liquid and agarose is given in Appendix B.

Aside from M9 medium being well defined, the primary reason it is used in this thesis over other media is because it is a low-fluorescing media at 488 nm, the wavelength required for excitation of green fluorescent protein (GFP) [92]. This provides an increased contrast between the bacteria and the background signal. However, in order to investigate the 3D position of bacteria relative to the agarose in which it is growing, it is necessary to add external fluorophores to the agarose in order for the agarose to be visible in a PMT channel. For experiments of this nature Rhodamine B and Nile Blue fluorophores were selected, as both fluorophores can be excited using the confocal microscope and their respective emission spectra are well separated from the fluorescent signals of the GFP in the bacteria.

Fluorescent doping of agarose

For agarose doped with either Rhodamine B or Nile Blue the same protocol is followed for preparation of the agarose. But, at the point of melting the agarose, before placing on the microscope slide, concentrations of Rhodamine B or Nile Blue are added. In order to produce an analogous signal between the GFP fluorescence in the bacteria and the agarose media, and to allow imaging of both fluorophores simultaneously without bleaching or damaging the sample in any way, the concentration of the fluorophore in the agarose media must be carefully controlled. For Rhodamine B, a volume of 20 µl stock solution[4] of Rhodamine B is added to 2 ml of M9 agarose, and for Nile Blue doped agarose, 0.02 g of Nile Blue solid is added to 2 ml of M9 agarose to obtain analogous signals.

3.2.2 Bacterial cultures

All bacterial cultures used in this thesis are derivatives of *E. coli* K-12 which are initially grown on working plates from stock cultures. A colony from the working plate is then suspended in 10 ml of media and grown overnight for 16±2 hrs at 37 °C before being resuspended in 10 ml of fresh medium, at a dilution of 1:100, and grown into late exponential phase (Figure 3.1). Once the exponential phase has been reached the cultures are spun down using a centrifuge, removed from the medium and resuspended

[3] Obtained from Invitrogen `https://www.lifetechnologies.com/order/catalog/product/16500500`

[4] Stock solution of Rhodamine B was prepared by Dario Dell'Arciprete and Dr. Andrew Schofield by adding 20 mg of Rhodamine B to 100 ml ddH_2O giving a concentration of 0.02 % (weight/volume)

in phosphate buffered saline (PBS) to dilute the sample to concentrations of 10^7cells/ml. The samples are then pipetted onto the agarose pads (§3.2.3).

The cultures used in this thesis for different experiments have slight genetic variances between them, partly due to the need to include different fluorophores in the bacterial samples in order to image them. For experiments on bacterial growth on agarose surfaces, strains expressing green fluorescent protein (GFP) were used and two different methods of including GFP in bacterial cultures were explored, one being the insertion of GFP directly onto the chromosome of the bacterium and the other, the insertion of a tetracycline (TET) resistant GFP-expressing plasmid into the bacterium. For investigation of the division of bacteria on an agarose surface, a yellow fluorescent protein (YFP) fluorophore co-expressed by a plasmid with FtsZ (a protein directly associated with the septation (division) process of *E. coli*) was transformed in to the bacterium. In order to provide uniformity across all experiments, and to allow comparison, these variations have been limited as much as possible, however, the differences which exist are outlined below and summarised in Table 3.1 (p. 26).

E. coli K-12 MG1655 with GFP plasmid

E. coli K-12 MG1655 is a laboratory strain of *E. coli* closely related to wild-type K-12 (only 2 mutations), but is without the dangerous lambda phage. It was the first strain of *E. coli* selected by Blattner *et al.* for genome sequencing [93], the result being MG1655 has become one of the favourite strains of *E. coli* for bacterial studies. Our strain of MG1655 has the plasmid[5] pHC60, a tetracycline (TET) resistant plasmid which expresses green fluorescent protein (GFP), transformed (inserted) into the bacterium [94].[6] The copy number of pHC60 is large resulting in strong fluorescence across the colony as bacteria divide. Since the plasmid is TET resistant, it is necessary to include the antibiotic TET in the growth media, to ensure the bacteria include the plasmid when dividing. TET, dissolved in ethanol ($5\,\mu g\,ml^{-1}$), is used on the working plates and in liquid cultures at the working concentration of $10\,\mu l\,ml^{-1}$ specified in Molecular Cloning - A Laboratory Manual [95].

Cultures of *E. coli* MG1655 with pHC60 are incubated overnight in 10 ml M9(+TET)

[5] A plasmid is a loop of DNA independent of the chromosome. Plasmids have a small number of genes (usually fewer than 30) and replicate independently of the chromosome. The number of plasmids present in the bacterium is important in fluorescence imaging as the more there are within the bacterium (known as the copy number) the greater the fluorescence signal from each bacterium. Plasmids cost the bacterium additional energy to reproduce and consequently reduce the growth rate compared to wild-type or otherwise identical strains.

[6] All transformation of plasmids used in this thesis was performed by Dr. Angela Dawson

for 16±2 hours at 37 °C to bring the bacterial culture into the stationary growth phase, before a volume of 100 µl of the culture is transferred to 10 ml M9(+TET) and incubated until the culture reaches an optical density (OD) of between 0.3 and 0.4 when measured at 600 nm, ensuring the culture is in the late exponential phase of growth (Figure 3.1). Rather than the 1:100 dilution with which experimental cultures are seeded, the cultures in Figure 3.1 were seeded with a 1:1000 concentration of the overnight culture to ensure the contribution of the bacterial cultures to OD were below the detection limit of the plate reader. Doing this means it is possible to normalise OD measurements, by allowing

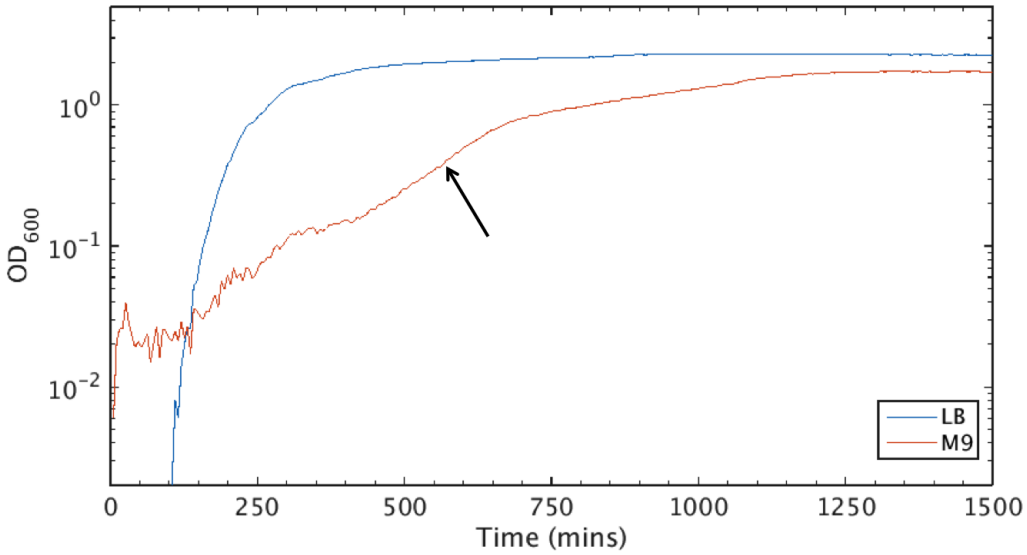

Figure 3.1: Growth curves measured for *E. coli* K-12 MG1655 with the addition of the GFP expressing pHC60 plasmid in LB (blue) and M9 (red) media. Growth curves were measured in triplicate with an inoculum of 1:1000 from stationary phase in order to be initially below the detection limit of the FLUOstar Optima plate reader. For experiments, cultures were removed at OD's between 0.3 and 0.4 (black arrow). This corresponds to 4 hrs (240 min) for an inoculum of 1:100.

the removal of the contribution provided by the growth media. However, a consequence of this is that the time for the OD to reach the required level, between 0.3 and 0.4, is extended in Figure 3.1 when compared to inocula of 1:100. In practice, cultures created from an inoculum of 1:100 of the overnight culture, reach OD measurements between 0.3 and 0.4 (arrow) at 600 nm after approximately 4 hrs (240 min).

E. coli K-12 MG1655 (+GFP)

E. coli strain K-12 MG1655 is again used in order to allow direct comparison between the relative growth of the two strains and the effect of chromosomal and plasmid GFP.

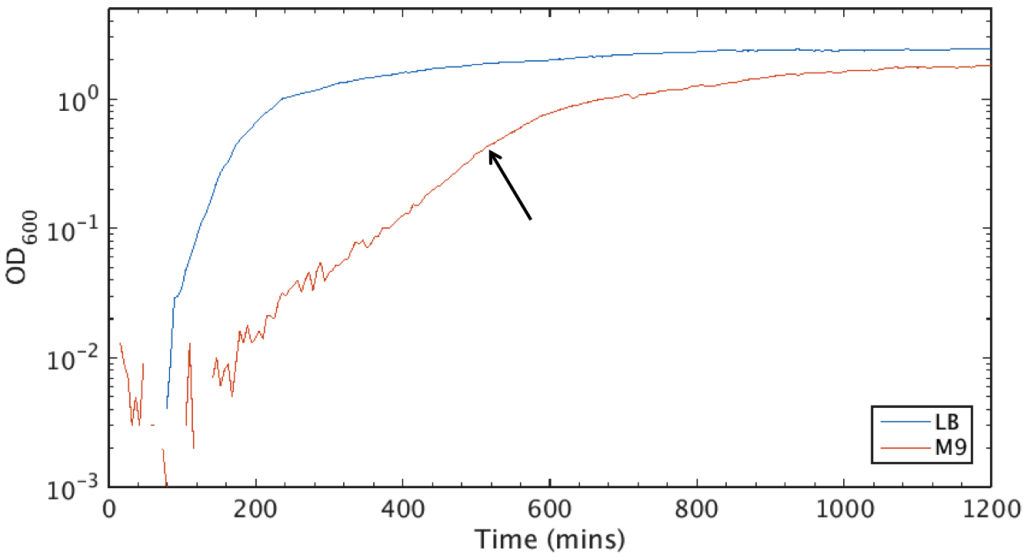

Figure 3.2: Growth curves for *E. coli* K-12 MG1655 expressing GFP inserted onto the chromosome in LB (blue) and M9 (black) media. Cultures were measured in triplicate for inocula of 1:1000 in order to be below the detection limit of the FLUOstar Optima plate reader to allow for removal of signal from the growth media. Cultures were removed upon reaching OD's of between 0.3 and 0.4 (black arrow) when measured at 600 nm. This corresponds to 4 hrs (240 min) for an inoculum of 1:100.

However, rather than inserted as a plasmid, the GFP is inserted onto the chromosome[7] of the *E. coli* and as a result the intensity of the fluorescence is reduced relative to the plasmid strain. As with the plasmid strain, the chromosonal strain is grown overnight into the stationary phase in 10 ml of M9 media for 16 ± 2 hrs at 37 °C before 100 µl is transferred to 10 ml of fresh M9 media and incubated at 37 °C into late-exponential phase (Figure 3.2). Again, the plate reader was inoculated with 1:1000 concentrations of stationary phase culture, meaning the initial measurements are below the detection limit of the plate reader, in order to allow removal of signal from the growth media. Experimental cultures were removed upon reaching OD's of between 0.3 and 0.4 when measured at 600 nm in order to ensure the bacteria were growing in late exponential phase (arrow), which corresponds to 4 hrs (240 min) for an inoculum of 1:100.

[7]The chromosome of *E. coli* is a double strand DNA loop containing all the genetic information necessary for the replication of the bacterium. Inserting the GFP directly onto the chromosome means that the bacterium will automatically copy the fluorescence when it divides without requiring additional antibiotics in the media. The trade-off for this is the reduction in signal relative to inserting GFP as a plasmid. The need for no additional antibiotics to be included in the media to maintain the GFP within the bacterium does mean that this strain is closer to the wild-type. The growth rate of the chromosonal GFP is analogous to wild-type measurements.

E. coli K-12 MG1655 with pLAU80

E. coli strain K-12 MG1655 is again used in order to allow direct comparison between all experiments conducted in this thesis, however, for experiments into the location of the septation (division) point of the bacteria the plasmid pLAU80 was transformed into the bacteria. The plasmid pLAU80 contains an L-arabinose inducible promoter P_{BAD}, Amp^R (ampicillin resistance) and FtsZ-yfp fusion, [96, 97] allowing specific expression of yellow-fluorescent protein (YFP) where FtsZ (linked directly to the septation) concentrates within a bacterium. The ampicillin resistance means that by including ampicillin from stock solution ($50\,\mathrm{mg\,ml^{-1}}$ in H_2O) in working concentrations of 10 µl in 10 ml of the M9 growth media it is possible to maintain the plasmid in all bacteria in the culture in a similar way to the inclusion of TET for pHC60 [95]. The pLAU80 plasmid works very differently to the GFP expressing plasmid pHC60 described above as the target fusion protein (YFP-FtsZ) is not constitutively expressed when the colony grows, but is rather controlled by an inducible promotor, so that it is only activated by the addition of arabinose to the growth media.[8] A promotor is a region of DNA that triggers the first stages of gene expression (known as transcription). When a promotor is inducible, as in the case of the L-arabinose promotor (P_{BAD}), the promotion of gene expression is initiated (induced) by the presence or absence of a physical or chemical factor. For P_{BAD}, the gene expression is induced by the inclusion of arabinose in the growth media.

Including arabinose in the growth media adds additional complications to sample preparation of MG1655, as Schleif *et al.* have shown that *E. coli* MG1655 can utilise arabinose through one of its metabolic pathways [98]. It is therefore necessary to include a greater concentration of arabinose than that specified by Lau *et al.* (0.05 % rather than 0.01 %) in order to ensure all the bacteria are exposed to arabinose at a sufficiently high concentration to induce the expression of the YFP in pLAU80 [96]. Additionally, glucose inhibits the uptake of arabinose in MG1655, since glucose is a preferential metabolite to arabinose (a process known as carbon catabolic repression) [99], and, as a result, it is necessary to exclude glucose from the growth media in order to successfully induce pLAU80. Starvation of the bacteria for a prolonged period is sub-optimal, and is known to lead to significant stress on the bacteria, causing them, amongst other things, to fail to septate correctly. Instead they grow as long filamentous organisms [100]. Subsequently, it was determined experimentally that the best compromise was the introduction of arabinose for the final 30 min of the exponential growth phase in

[8] Arabinose is only the inducer in the case of this specific plasmid, although it can be used to induce other plasmids as well. In general, inducible plasmids are activated by many varying promotors, both chemical (such as arabinose) and physical (such as light induction).

Strain	Derivative	Genotype	Fluorescence	
MG1655 (+GFP)	K-12	F^- λ^- ilvG- rfb-50 rph-1	GFP	[102]
MG1655 (pHC60)	K-12	F^- λ^- ilvG- rfb-50 rph-1	GFP	[102]
MG1655 (pLAU80)	K-12	F^- λ^- ilvG- rfb-50 rph-1	YFP	[102]
YD133 (pLAU80)	K-12	ΔFimA ΔFliC ΔFlgE	YFP	[101]

Table 3.1: *E. coli* K-12 derivative strains used for experiments within this thesis. Information on the strain derivative, genotype (deletions) and fluorescence are included.

M9 growth media. To achieve this, the sample was spun down from the exponential growth media (10 ml of a standard M9+Glucose media) and resuspended in 10 ml of M9 growth media excluding glucose and with 0.05 % (5 µl) arabinose added from stock solution.[9] Upon conclusion of this period the sample was again spun down and diluted in PBS to ensure concentrations of 10^7 cells/ml, before being pipetted onto the agarose pads.

E. coli K-12 YD133 with pLAU80

While MG1655 with pLAU80 is used in experiments conducted in this thesis (Chapter 7, p. 97), in order to ensure that the metabolism of arabinose by MG1655 or the starvation of the cultures in the growth phase were not significant in any phenomena observed, *E. coli* YD133, a strain of *E. coli* not known to metabolise arabinose is used as control. Our strain of *E. coli* K-12 YD133 is a K-12 derivative with deletions ΔFimA, ΔFliC and ΔFlgE [101], transformed with the plasmid pLAU80 [96]. YD133 is a strain derived from MG1655 and does not metabolise arabinose, allowing introduction of arabinose into the growth medium without the need to starve the culture.

3.2.3 Sample chamber

In order to achieve 3D resolution suitable for the imaging of bacteria, a custom made sample chamber is used [91]. A microscope slide is cleaned and a GeneFrame (ThermoScientific)[10] fixed to it. M9 media mixed with the required concentration

[9] Stock solutions of arabinose were obtained from the School of Biology media laboratories and are 20 % arabinose (i.e. 10 mg of arabinose for every 50 ml of ddH_2O). Consequently the addition of 0.05 % arabinose to 10 ml media cultures, as is the case here, requires addition of 250 µl of the stock solution (20 % arabinose).

[10] Double-sided adhesive consumable initially designed for PCR analysis proved to be excellent structures for containing a shallow pad of agarose. `www.thermoscientificbio.com/plastic-consumables/gene-frame/`

of agarose is heated and a volume of 250 µl pipetted into the GeneFrame. An additional microscope slide is placed over the GeneFrame to flatten the surface and ensure sterile conditions are observed while the agarose cools, creating an agarose pad (Figure 3.3). Upon solidification of the agarose, the top microscope slide is removed and two channels cut across the short axis of the agarose pad, creating three smaller pads of approximately identical size within the GeneFrame. These channels allow the samples to be well oxygenated and provide three agarose pads on which to place different concentrations of bacteria on the same microscope slide, ensuring a suitable concentration (of the order of 10^7 cells/ml) of bacteria is present for imaging. The samples (green) are pipetted onto or into the agarose pad depending on the experimental conditions, left to dry and sealed with a coverslip. The entire sample is then inverted and imaged using the confocal microscope.

Figure 3.3: Schematic of sample chamber used in experiments. Bacterial samples (green), are pipetted onto three agarose pads (brown), held in place by a microscope slide (bottom), GeneFrame, (sides), and sealed with a coverslip (top). The entire sample is then inverted and imaged using the confocal microscope.

Depending upon the geometry of the system under investigation (i.e. whether the colonies are to be close to the surface or spread throughout the agarose) the diluted cultures are placed on the microscope slide in one of three ways. The first, the method of sample preparation for the majority of experiments, examines bacterial colonies on the surface of the agarose. The second is for bacterial colonies entirely surrounded by agarose (within agarose) and the final method is for unsealed samples which are exposed to the air (position on agarose).

Bacterial colonies on agarose surfaces

For the majority of experiments conducted in this thesis, bacterial colonies are pipetted onto the surface of the agarose pad, which fills the entire GeneFrame, from the PBS dilutions and the PBS is allowed to evaporate for 2 min, leaving the bacterial culture on the surface of the agarose. The sample chamber is then sealed using a coverslip on top of the GeneFrame, which is necessary in order to get close to the sample and achieve the axial resolution required for resolving individual bacteria in the colony. The sample is then inverted and imaged using a Zeiss Confocal LSM 700.

Bacterial colonies within agarose

Bacterial colonies buried in the agarose are prepared in a similar way to those on the agarose surface, with some key alterations. Firstly, rather than filling the sample chamber entirely with agarose, the sample chamber is only partially filled with a volume of agarose calculated to leave approximately a 5 µm air gap from the surface of the agarose to the maximum capacity of the frame. The bacteria are then pipetted into the sample as before and the PBS allowed to evaporate before the remaining capacity of the frame is filled with molten M9 agarose solution at a temperature of 50 °C and sealed with a coverslip.

Bacteria position on agarose samples

Finally, to investigate the effect of closing the sample with a coverslip it is necessary to image the bacteria in an open system. This is achieved by fixing a GeneFrame directly to a coverslip. As small a volume of agarose as possible is then pipetted onto the coverslip in order to allow imaging of the bacterial colony through the coverslip (and the agarose) from beneath and thus enable the sample to remain open to the air. The coverslip is placed onto the confocal microscope stage and imaging is conducted as the bacterial sample is pipetted onto the agarose surface. This allows real-time analysis of the nature of the drying process conducted on the bench for the other two methods of sample preparation.

3.3 Confocal fluorescence microscope

Confocal microscopy was performed using a Zeiss Confocal Laser Scanning Microscope (LSM) 700. Images were acquired at a scan resolution of 1024×1024 pixels providing a suitable pixel resolution below the diffraction limit, in order to limit digital noise, whilst maintaining a large enough image area to capture full colony growth over the time course of the experiments. The Zeiss Confocal LSM is integrated into a standard microscope, allowing initial positioning of samples on the stage through a traditional brightfield set up. Additional to the brightfield illumination, the Zeiss Confocal LSM 700 is equipped with four diode lasers of wavelength, 405 nm, 488 nm, 555 nm and 633 nm, with maximum output powers from the end of the fibre used to direct the beam into the microscope body of 5 mW, 10 mW, 10 mW and 5 mW respectively. The four laser wavelengths allow tuning of the incident light directly to the excitation peak of the fluorophore used for the specific experiment (Table 3.2). For green-fluorescent protein (GFP) and yellow-fluorescent protein (YFP) the laser excitation is performed using a laser wavelength of 488 nm, while for Rhodamine B, the wavelength is 555 nm and for

Fluorophore	Excitation Peak (nm)	Laser Wavelength (nm)
Green Fluorescent Protein (GFP)	475	488
Yellow Fluorescent Protein (YFP)	514	488
Rhodamine B	540	555
Nile Blue	635	633

Table 3.2: Excitation peaks and targeted laser excitation wavelengths of fluorophores used in experiments within this thesis

Nile Blue, 633 nm. YFP excitation by a laser wavelength of 488 nm is well removed from the maximum peak of excitation (514 nm), but due to the excitation spectrum of the fluorophore, 488 nm still induces significant excitation of the fluorescent protein, providing an output signal intensity suitable for analysis.

Signal acquisition from the LSM 700 is available in two photomultiplier tube (PMT) channels simultaneously, or sequentially, in epi-detection mode, with an additional PMT able to acquire signal from transmitted signals (T-PMT). The T-PMT collects signal from part of the incident beam (i.e. the laser wavelength) which has passed through the entire sample, providing a pseudo-brightfield image, which has no axial resolution but a lateral resolution with a theoretical limit of $0.4\frac{\lambda}{\mathrm{NA}}$ (Eq. 2.3), allowing imaging of the sample areas which are not tagged with fluorescent markers.

3.4 Deconvolution

As discussed in Chapter 2 (p. 8), brightfield light microscopy is limited initially by the Rayleigh criterion, which can be reduced by using laser scanning microscopy methods such as laser scanning confocal microscopy. Despite these improvements, when imaging bacterial samples, the resolution of these systems, particularly in the axial direction, is still very close to the physical size of the bacterium. As a result, as the packing fraction of bacteria tends to 1 (as is the case for bacterial colonies) it becomes difficult to resolve individual cells in the collective sample. Therefore, for 3D reconstruction of such samples the need to maximise the resolution in all three-dimensions (plus time) is vital for correct identification of a specific bacterium in a colony. A way of improving the resolution achievable from microscopes is to remove the distorting effect the optical elements (and indeed the media through which imaging is taking place) have on the signal obtained from the sample. This process, known as deconvolution, is used for experiments in this thesis and consequently, the methods of achieving this are described here.

3.4.1 Overview

When light passes through a lens, or is reflected from a mirror, blurring and noise from the optical element are added to the incident light from the object. When passed through a series of optical elements (as in the case of a microscope) this can cause serious distortions, dramatically reducing the resolution. This is of particular importance when attempting to view samples at, or below, the resolution of the microscope, since the size of the objects being imaged is the same order of magnitude as the distortion. While it is not possible to remove the blurring during image acquisition, deconvolution can be used during image processing to reduce the distortions and restore the image to a quality close to that predicted for an ideal imaging system (referred to as the 'perfect image').

To deconvolve an image it is necessary to know the extent of the distortion generated by the optical elements used. This is achieved by generating a point spread function (PSF) of the microscope, which can then be removed from the images. The PSF is the image of a point source, which in practice is usually a bead with a diameter that is below the optical resolution of the microscope. PSFs can be theoretically calculated, but it is generally best to directly acquire a PSF for the microscope and settings used for sample measurements, especially since it is wavelength dependent. The acquisition process required for PSFs for this thesis is outlined in the following section.

Mathematically, the image acquired by the PMT ($I_i(X,Y)$) is the convolution of the emitted light from the object ($I_o(x,y)$) and the PSF ($\delta(x,y)$).

$$I_i(X,Y) = I_o(x,y) \otimes \delta(x,y) \tag{3.1}$$

To solve a convolution of this type and obtain $I_o(x,y)$, each element in Eq. 3.1 must be Fourier transformed from the spatial domain (x,y) into the frequency domain (k) using the convolution theorem

$$\mathscr{F}\{g\} = \mathscr{F}\{f \otimes h\} = \mathscr{F}\{f\} \cdot \mathscr{F}\{h\} \tag{3.2}$$

where $\mathscr{F}$ denotes the Fourier transform of the respective function. Eq. 3.1 can therefore be rewritten as

$$\mathscr{F}\{I_i(X,Y)\} = \mathscr{F}\{I_o(x,y)\} \cdot \mathscr{F}\{\delta(x,y)\} \tag{3.3}$$

Performing this transformation means $\mathscr{F}\{I_i(x,y)\}$ can be divided by $\mathscr{F}\{\delta(x,y)\}$ to obtain $\mathscr{F}\{I_o(x,y)\}$ and ultimately $I_o(x,y)$.

3.4.2 Point spread function

PSFs used in bacterial colony experiments in this thesis were acquired using TetraSpeck fluorescent microspheres of diameter 0.1 µm [103].[11] The TetraSpeck microspheres fluoresce with four different excitation peaks across the entire spectrum of emission used in these experiments. The microsphere samples are sealed, making it impractical to immerse them in agarose. However, since the primary constituent of M9 agarose is water the PSF should be analogous, particularly very close to the coverslip. Samples of Tetraspeck beads fixed to the coverslip and immersed in deionised water were inverted and placed on the confocal microscope (§3.2.3 p. 27) and stacks taken through the sample using identical settings to those used for bacterial sample acquisition. The resulting stacks were processed using the inbuilt PSF analyser within Huygens Deconvolution Software (SVI).[12]

Using the PSF obtained from measurements of Tetraspeck beads, it is possible to extract the perfect image stack from the image stack recorded by the confocal microscope by reversing the convolution process where the perfect image[13] was combined with the image created by the effect of the optical microscope. However, improving the resolution of the stacks of images is immaterial if it is impossible to successfully identify the location of individual bacteria within the colony. There are numerous ways for doing this, many of these with severe limitations, and these are discussed below, along with the method selected for reconstruction of bacterial colonies in three dimensions as a function of time.

3.5 Reconstruction

In order to successfully create a 3D sectioned micrograph of a bacterial colony at a point in time, it is necessary to identify all the individuals within the sample. Commercially, there are several packages capable of doing this, however, many are exclusively 2D techniques, so that a third of the spatial information is lost.

[11] Life Technologies `www.lifetechnologies.com`

[12] Huygens Deconvolution Software is a commercially available deconvolution programme for deconvolving stacks of images from confocal microscope acquisition. The software provides functions for theoretically calculating a PSF from input parameters or of producing a PSF from input stack images. Information on the software is available at `www.svi.nl/HuygensEssential`.

[13] Throughout this thesis, I use 'perfect image' to denote the theoretical image which faithfully reproduces, in a one-to-one correspondence, the object being imaged without noise. Perfect image corresponds directly to $I_o\{x, y\}$ in Eq. 3.1. The perfect image is only altered from the object by a rotation or scalar transformation.

3.5.1 Commercial 2D reconstruction software

It is relatively straightforward to reconstruct 2D systems with a high level of precision, Narayan *et al.* achieved this for millimetre scale rice bails and cylindrical colloids, with success rates above 97 %, even at extremely dense packing fractions of particles [104] using freeware readily available within the ImageJ community [105, 106]. These processes would be easily transferable to micrometre level systems on the condition that the resolution of the system is of a suitable level for separating closely packed samples. Similar to Narayan, a package used extensively in our group is Schnitzcells, a Matlab based package allowing quantitative analysis of time-lapse movies of living cells [85]. Schnitzcells offers excellent accuracy for quasi-2D systems but the degree of user input necessary to achieve this is considerable.

3.5.2 3D location of objects at micrometre scale

The software packages above are not readily transferable to 3D structures, both the ImageJ plugins and Schnitzcells search simultaneously in 2D for local maxima (i.e. they locate and define a backbone corresponding to the central structure of the bacterium/particles only in the plane of imaging). When a system is confined to a quasi-2D state this is not necessarily an inherent problem, however, when wishing to consider the true axial position and orientation of a particle or bacterium in a 3D structure it is necessary to evaluate surrounding voxels in all three dimensions in order to ensure vital information is not lost. The algorithms used in Schnitzcells are designed for efficiency in 2D analysis resulting in a non-trivial conversion to 3D reconstruction as they are embedded within several steps of the program.

In ImageJ there are 3D visualisation tools which allow the user to view systems in three-dimensions. Included amongst these are Volume Viewer, 3D viewer and BoneJ, all of which allow the user to qualitatively view the system in a 3D rendering [107–109].[14] From these 3D visualisers, the user can obtain some quantitative information from the input 3D samples, unfortunately, the user input is labour intensive and, particularly in the case of Volume Viewer, the output is error prone.

Consequently, with no commercial software, or freeware, capable of identifying individual cells in a densely packed environment, and subsequently extracting spatial information from the images I have collaborated with members of the colloidal physics group in order to obtain quantitative information on cells in a microcolony.

[14] More detail of all of these plugins can be found in reference [110]

3.5.3 3D reconstruction code

3D reconstruction of microcolonies is an analogous problem to identification of individual rod-shaped colloids in rheo-imaging. Code developed by Thjis Besseling and Michiel Hermes for the purpose of identifying individual particles in a sheared sample of colloidal rods is capable of extracting spatial information on the location and orientation of individual rods in both disperse systems and those which are approaching close-packed volumes [111]. However, colloidal rods are a far simpler system to work with than bacteria, being of approximately the same size, remaining rigidly straight (to a first approximation) and neither altering their dimensions greatly nor dividing as a function of time. Despite this, 3D reconstruction of bacterial microcolonies was achieved using the code developed by Thjis Besseling and Michiel Hermes and the process in which identification of individual cells is achieved is briefly described below [111].

3.5.4 Code processes

The Besseling and Hermes code reads an input tiff stack of grayscale images, deconvolved using Huygens Essential, and locates the centre of mass of each bacterium in three-dimensions. This is achieved by fitting backbones along pixels which exhibit an increased intensity when compared in their locality after the image has been thresholded and background noise removed. Spherocylinders (cylinders with two hemispherical caps) are fitted to these backbones and filtered to ensure overlap, length and curvature are within physical limits defined by the user for the bacteria. For the *E. coli* samples used in these experiments, the parameters were chosen to ensure the bacterium had length dimensions in the long axis of between 0.8 µm to 10 µm; short axis 0.4 µm to 1.0 µm and to ensure the 'hard core' (i.e. the incompressible part of the bacterium) was limited to a size no smaller than 0.8 µm and 0.4 µm in the long and short axes respectively. By experiment, the curvature variation allowed along the length of the bacterium was set at 10 % before the backbone was split, providing a degree of flexibility for the bacteria but meaning the code was still successful in identification of all individual cells in the colony. After filtering using these parameters, the 3D position, orientation, length and diameter of the remaining spherocylinders is then output to a text file for analysis.

Chapter 4

Three-dimensional reconstruction of bacterial microcolonies

4.1 Introduction

Advances in optical microscopy techniques have allowed increased study of samples of bacteria at a single bacterial cell resolution [40, 112–114]. The resolution of techniques, such as phase-contrast microscopy, fluorescence microscopy and confocal microscopy, has allowed detailed investigation of the properties of individual bacteria in 2D and (in the latter case) 3D [115–117]. However, the resolution of these imaging systems means that resolving densely packed micron sized particles (like bacteria in a colony) is difficult, even in static samples [104], and consequently, studies of bacterial colonies tend to focus on properties of the colony as a whole rather than identifying single bacteria within the colony [47–49, 91]. While investigations of colony development on a global (multiple bacterial level) scale are important in the understanding of these structures, it is also important that a better understanding is obtained of the role which individuals in the colony play in the production of these global phenomena. In order to achieve this, it is vital that experimentalists are able to extract spatial and orientational information on each individual in the population and this is one of the primary aims of experiments conducted as part of this thesis. In this chapter I outline developments in conventional confocal microscopy, and in the post-processing of the acquired images, that provide images of suitable quality for single bacterium resolution of bacterial microcolonies.

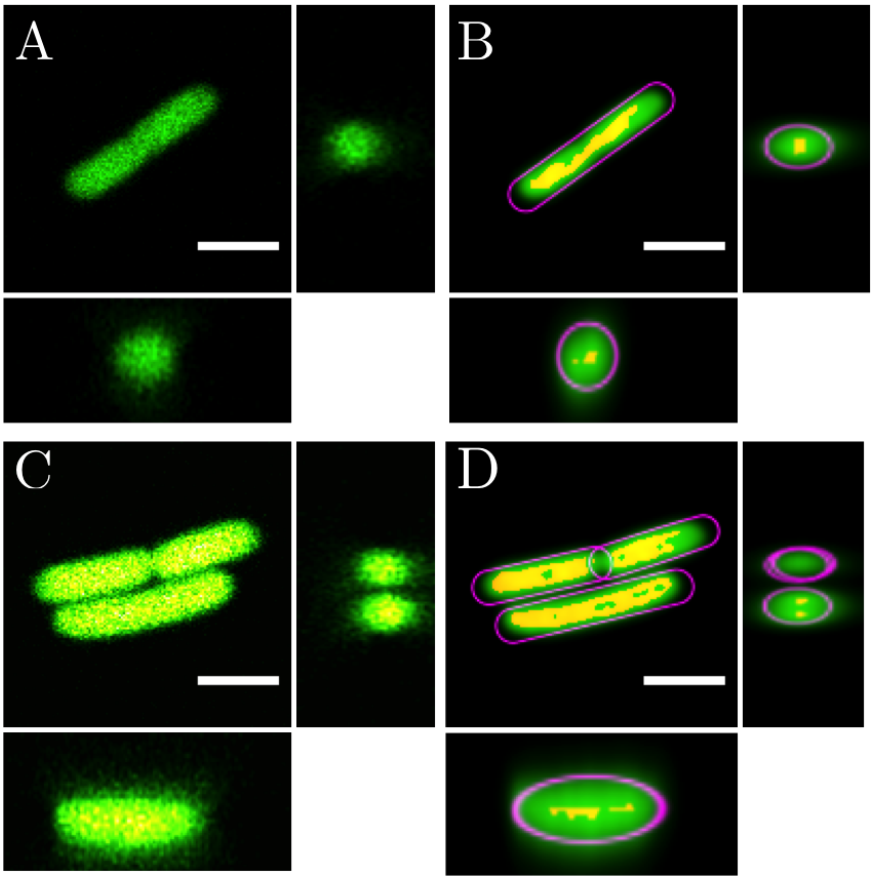

Figure 4.1: Three-dimensional reconstruction of early stage colony growth in three-dimensions. [A] Confocal stack of single bacterium incident on 2 % agarose surface. The bacterium is surrounded on all but one side by low fluorescing M9 agarose media (the other being the coverslip), resulting in dark pixels adjacent to the high intensity pixels defining the bacterium. Slices are imaged in 0.1 µm steps. [B] Reconstruction of A. The backbone (yellow pixels) is clearly identified along the major axis of the bacterium ensuring the subsequent spherocylinder (purple outline) is fitted well to the dimensions of the bacterium. [C] Confocal stack of early growth of a bacterial colony incident on 2 % agarose surface. Slices are recorded at 0.1 µm intervals. [D] Reconstruction of C. Despite the close proximity of the adjacent bacteria in the xy plane of imaging the backbones are clearly identified and the subsequent spherocylinder fits are a good representation of the position of each bacterium on the agarose surface. Scale bars are 2.0 µm.

4.2 Reconstruction in 3D

From raw confocal microscopy stacks (taken directly from a Zeiss Confocal LSM 700) of a seed bacterium on an agarose pad, Figure 4.1A, it is a relatively simple process to identify and extract the position and orientation of the bacterium from the image. Bacteria such as this, are clearly separated in the imaging plane, and as a result when analysing the confocal stack with the code developed by Besseling and Hermes [111]

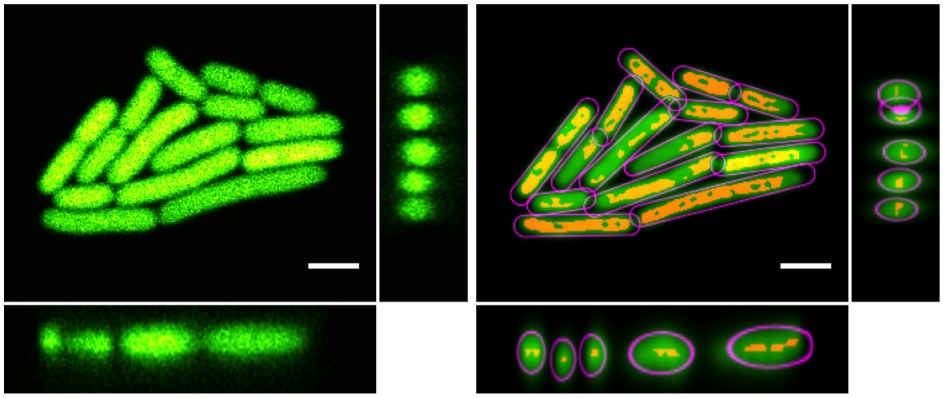

Figure 4.2: 3D reconstruction of single layer colonies grown on a 2 % agarose surface. [Left] Confocal stack of a single layer colony grown on a 2 % agarose surface. Slices are taken at 0.1 µm intervals. [Right] Reconstruction of single layer colony in 3D. The code successfully determines individual bacteria (green) entirely surrounded by adjacent bacteria within the colony by fitting a spherocylinder (purple outline) to a line of backbone pixels (yellow) along the length of the bacterium. Scale bar is 2.0 µm.

(§3.5.3, p. 33) the bacterium is correctly identified (B), with a clear backbone (yellow) through the centre of the bacteria and a spherocylinder (purple) fitted along the entire length of the bacterium. This is primarily because, in this case, a bacterium on the agarose surface is surrounded by M9 agarose, which is a low fluorescing media, and therefore the voxels surrounding those of the bacterium are generally dark in comparison.

However, as the colony grows and expands on the agarose, it becomes harder to resolve individual cells, as the seed bacterium now has other bacteria adjacent to it, which result in neighbouring voxels, from independent bacteria, exhibiting similar intensity to each other. For early stage colony development, where a bacterium is not entirely confined by adjacent bacteria, retrieving location and orientation information for all bacteria is still relatively straightforward (C and D). But, as the colony develops in a single layer, the central bacteria are confined in 2D by adjacent bacteria, the agarose, and the coverslip. This increases the complexity of the reconstruction, since the voxels defining the bacteria in the centre of the colony are now surrounded closely by voxels of similar intensity, (Figure 4.2). Due to the nature of confocal microscopy, the resolution in the focal (lateral) plane ($r_{\text{confocal}} \simeq 139\,\text{nm}$) is an order of magnitude smaller than the size of a bacterium and, as a result, it is relatively simple to identify all individual bacteria when the colony is constrained to a single plane.

However, the resolution of confocal microscopes in the axial direction is of the same

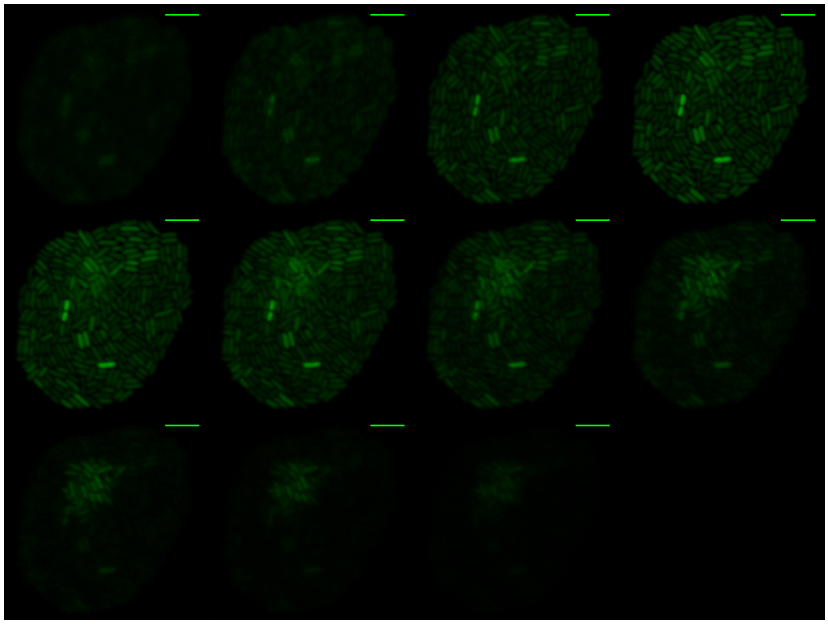

Figure 4.3: Raw confocal stack of bacterial colony after additional layer generation. Images are taken through the colony at 0.1 µm slices in the axial direction. Slices here are every 0.3 µm and scale bar is 5.0 µm.

order of magnitude as the diameter of a bacterium, (§2.2.3, p. 13) and, consequently, analysing microcolony images where the volume fraction of the microcolony is approaching 1 and bacteria form additional layers to the colony (buckle into the agarose surface), provides additional problems for reconstruction (Figure 4.3).

Firstly, the algorithm (§3.5.3, p. 33) used to determine the backbone of the bacterium can inadvertently merge two bacteria into one. This is particularly evident where the voxel size selected is at the limit of the resolution of the confocal microscope in the focal plane, rather than below it (Figure 4.3), adding additional digital noise (created by errors in the PMT acquisition rather than the optical setup of the confocal microscope) to the optical image. Additionally, the increased physical size which corresponds to a pixel of the PMT (around 140 nm compared to 70 nm) means there are fewer pixels of bright intensity to which the code can fit a backbone. Consequently, when bacteria form two layers the code struggles to distinguish the correct direction a backbone follows and has a tendency to fit backbones across two bacteria sitting adjacent to one another in the axial direction (Figure 4.4), due to the distance between pixels being approximately equal in all three-dimensions (100 nm along the optical axis and 140 nm in the focal plane). The code successfully reconstructs areas of the bacterial colony with only one layer of bacteria but where the colony has buckled and generated a second layer, the

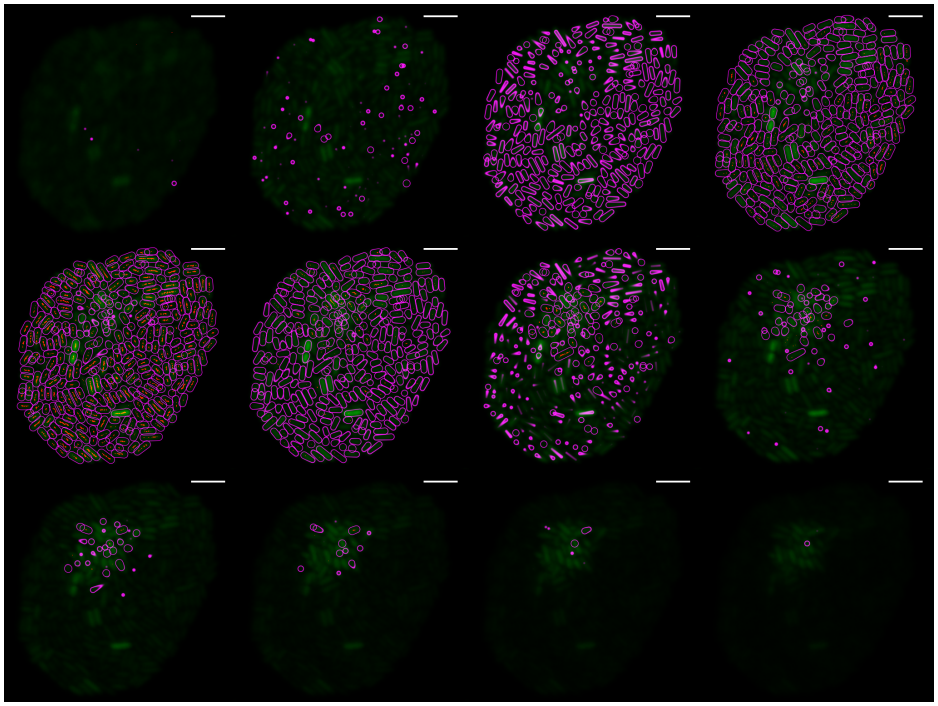

Figure 4.4: Reconstruction of bacterial colony which has buckled and developed a second layer above the primary layer. The reconstruction successfully identifies a bacterium within the colony where there is only a single layer of bacteria present. However, where the colony has buckled and an additional layer has been generated above the primary layer, the backbone (yellow) and subsequent outline (purple) does not fit well to the visible bacteria (green) within the colony. Scale bar is 5.0 µm.

resolution is not sufficient to distinguish the two layers. This leads to the backbones (yellow/orange) and outlines (purple) generated by the code not fitting to the bacteria (green) in Figure 4.4 . This is shown in more detail in Figure 4.5 which focuses on the area of Figure 4.4 where the reconstruction code fails to correctly identify bacteria. The raw image (green) and the fitted backbone (yellow/orange) and outline (purple) are not well matched.

The failure of the code primarily arises from the proximity of the diameter of the bacterium to the axial resolution of the confocal microscope and consequently, when the code executes 3D blurring of the pixels, in order to successfully stitch local maxima points together to form the backbone of the bacterium, the two layers are inadvertently merged together. This results in the distortions in the axial direction seen here and the failure to distinguish two layers in the colony. As a result of this the code overcounts the number of bacteria in the colony, with the code recording 324 independent bacteria compared to a manual count of 286 for the example shown in Figure 4.4.

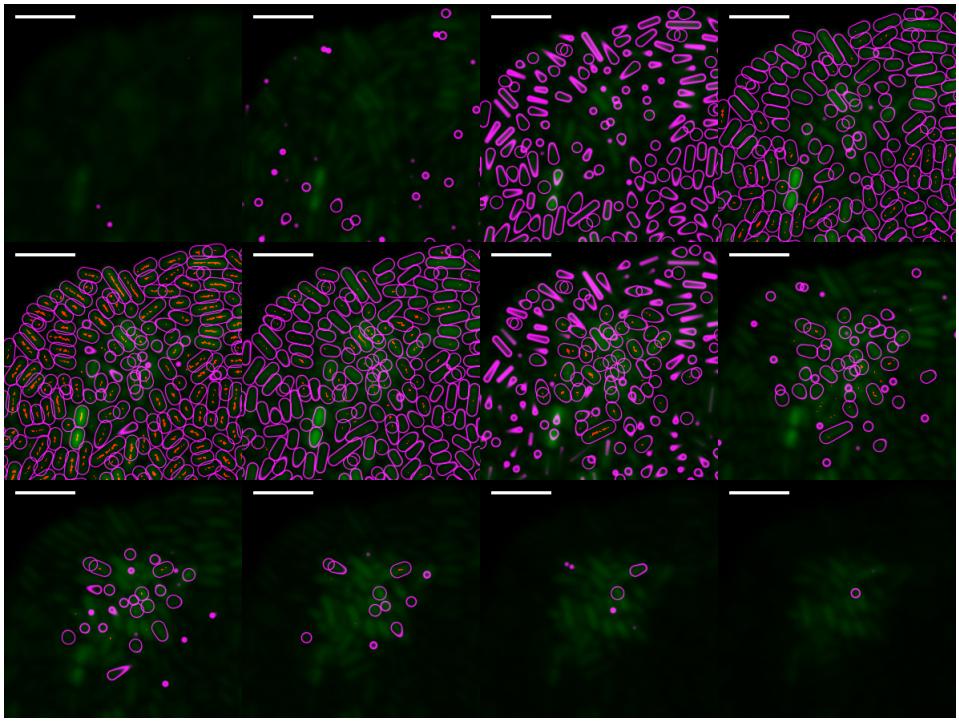

Figure 4.5: Area of Figure 4.4 focussing on the position where the colony has buckled and a second layer of bacteria has formed above the primary layer. It is evident here that the code fails to successfully locate all the bacteria (green) in this region and identifies incorrectly many others, fitting inconsistent backbones (yellow/orange) and outlines (purple) to the image as a result. The failure of the code primarily arises from the proximity of the diameter of the bacterium to the axial resolution of the confocal microscope. Consequently, when the code executes 3D blurring of the pixels, in order to successfully stitch local maxima points together to form the backbone of the bacterium, the two layers are inadvertently merged together. This results in distortions in the axial direction and failure to distinguish two layers within the colony. Scale bar is 5.0 µm.

4.2.1 Deconvolution

It is clear from Figures 4.4 and 4.5 that in order to successfully reconstruct bacterial microcolonies in 3D at a single bacterium resolution an improvement in the number of pixels per bacterium (pixels per micron), or clearer distinction of the edges of the bacteria as volume fraction tends to 1, must be achieved. The dimensions of a bacterium are just above the resolution limit of the confocal microscope (particularly in the axial direction) and while the confocal microscope has the capacity for increasing the pixels per micron well below the resolution limit of the optics, there is little increase in the information obtained in this way. It is therefore necessary to improve the distinction between adjacent bacteria in the colony in order to identify all the bacteria. This can be achieved by deconvolution of the raw confocal stacks.

As discussed in §3.4 (p. 29), deconvolution is a process used to recover the perfect image[1] of the bacteria in the colony, from the image stack recorded by the PMT. A point spread function (PSF), obtained through either a theoretical calculation dependent upon, amongst other factors, the wavelengths of the incident and emitted light and the refractive index of the media through which the light beams travel, or a direct measurement of the optical system used for measurements, is removed from the raw confocal image stack, allowing recovery of the perfect image.

In practice, theoretical PSFs prove problematic when evaluating experimental setups and models of theoretical PSFs generally assume perfect lenses with no spherical aberrations, as well as no distribution around the maximum excitation or emission of the incident wavelength. In reality, these assumptions are not valid in almost all cases. Specifically the latter, since emission of fluorescent proteins is a spectrum. While this can, in principle, be resolved by taking true distributions for the emission fluorophore and excitation wavelength, the result is a computationally heavy process. Shaevitz *et al.* have also show that the PSF of a microscope changes as a function of depth through the sample [118]. Additionally, while lens and mirror manufacturers are capable of producing optical elements at extremely high precision, the introduction of even small aberrations in a lens can have considerable cumulative results on the output signal. As a result, in almost all situations, it is better to measure directly the PSF for the system being used under identical conditions to those under which the measurement is being performed.

Measurements of the PSF

To measure the PSF of the Zeiss confocal LSM 700 used for measurements of bacteria in this thesis, commercially available Tetraspeck fluorescent microspheres of diameter 0.1 µm were used [103].[2] In contrast to Shaevitz *et al.*, a single PSF was used for all deconvolution performed in this thesis because all measurements were performed at, or close to, the coverslip of the microscope [118]. For imaging of colonies buried in agarose, the use of a depth-varying PSF may significantly improve the image quality.

Samples were inverted and placed on the confocal microscope (§3.2.3, p. 27) so they were being imaged through the coverslip and stacks were taken through the sample using the 63× oil immersion lens and excited at 488 nm in order to directly mirror conditions used

[1] Throughout this thesis, I use 'perfect image' to denote the theoretical image which faithfully reproduces, in a one-to-one correspondence, the object being imaged without noise. The perfect image is only altered from the object by a rotation or scalar transformation.

[2] Obtained from Life Technologies `www.lifetechnologies.com`

for the imaging of bacterial colonies. In order to ensure that the PSF was faithfully recorded, and not recording digital noise generated by the acquisition of the signal in the PMT channel, the pixel size was selected in all three dimensions to be well below the optical resolution of a confocal microscope, resulting in voxel (volume pixel) dimensions of $25 \times 25 \times 50\,\mathrm{nm}^3$ in x,y and z respectively. These dimensions were also below those used for imaging of the bacterial microcolonies, ensuring that subsequent deconvolution measurements were not compromised by reduced information in the PSF images. To provide optimal results, stacks of fifteen 0.1 µm diameter beads were acquired, allowing the PSF software to average out any noise within individual beads. The resulting stacks were processed through Huygens Deconvolution Software (SVI) using the inbuilt PSF analyser.[3] The software distills spherical beads, of known diameter, into a PSF for the system by subtracting the parameters of the spherical bead (i.e. the perfect image) from the image recorded by the microscope, leaving only the noise generated by the microscope.

Figure 4.6 shows the measured PSF imaged through the Zeiss LSM 700. In the xy plane (A) the point source is well defined with a clear blur (D) equal in all directions. This reflects the precision of the optical microscope and the clear resolution available in the xy plane, but as expected the blur in the axial direction (B-C) is far larger than that seen in the xy plane. Close inspection of the axial images also reveals a slight asymmetry in the blur profile along the optical axis (left to right in B and top to bottom in C), which can be attributed to slight misalignment of the optical system and is a recurring phenomenon for all PSFs for this microscope. The asymmetry seen in the PSF in the axial direction would not be included when considering a theoretical PSF and serves to highlight the importance of ensuring a correct calculation of the PSF for the system is obtained when using deconvolution to improve images.

The PSF shown in Figure 4.6, is for the photomultiplier tube (PMT) attached to Channel 2 of the Zeiss Confocal LSM 700 when exciting the sample at 488 nm with a 0.01 mW intensity and recording only GFP emission signals. For other excitation wavelengths, or indeed other fluorophores imaged in this channel, it is necessary to measure a new PSF, since the parameters governing the PSF have changed. Indeed, it was necessary to measure a separate PSF for the other PMT attached to Channel 1 in the confocal microscope. The two channels share identical optics until a final

[3]Huygens Deconvolution Software is a commercially available deconvolution programme for deconvolving stacks of images from confocal microscope acquisition. The software provides functions for theoretically calculating a PSF from input parameters or of producing a PSF from input stack images. Information on the software is available at `www.svi.nl/HuygensEssential`.

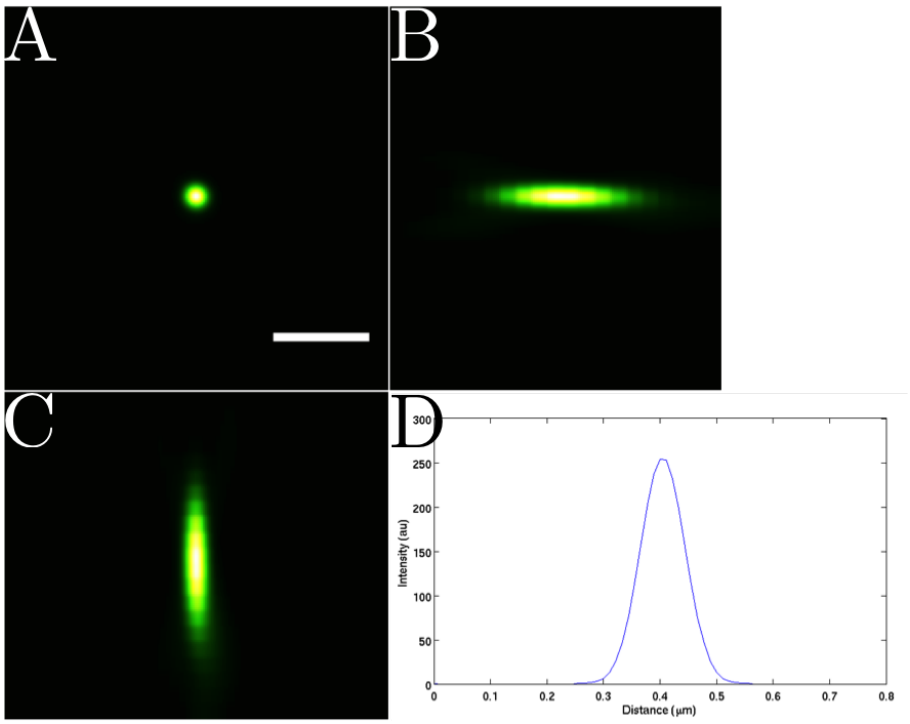

Figure 4.6: Measured point spread function (PSF) for Zeiss Confocal LSM 700. Tetraspeck fluorescent microspheres of diameter 0.1 µm were imaged with the Zeiss Confocal LSM 700 through the 63× oil immersion lens and excited at 488 nm in order to directly mirror conditions used for the imaging of bacterial colonies. The resulting stacks were processed in Huygens Essential (SVI). Orthogonal slices (B and C) through the PSF are shown with identical scale as the xy plane (A) to show the level of enhancement possible by deconvolving acquired image stacks on this scale. A slight asymmetry of the profile is seen in the orthogonal (axial) point which would not have been included if a theoretical PSF had been used in place of the measured. Scale bar is 500 nm. (D) the intensity profile through the centre of the bead in the lateral plane (A) in arbitrary units.

beamsplitter placed directly in front of the two PMTs deflecting part of the signal into Channel 1, but the difference in optical elements from this point on is significant to the PSF of the two channels. The filters used by Channel 1 to obtain the required signal are short-pass filters and, as a result, there is the addition of a reflection image in the acquired signal from the incident laser beam. Although this reflected image is usually a much lower intensity than the fluorescence image, and can generally be ignored, when dealing with biological samples, the intensity of light is low in order to limit phototoxicity of the living sample, meaning the reflected image forms a substantial part of the acquired signal. Consequently, the quality of the image is noticeably reduced when compared directly to Channel 2. For this reason, experiments requiring acquisition of a single emission spectrum are conducted exclusively in Channel 2.

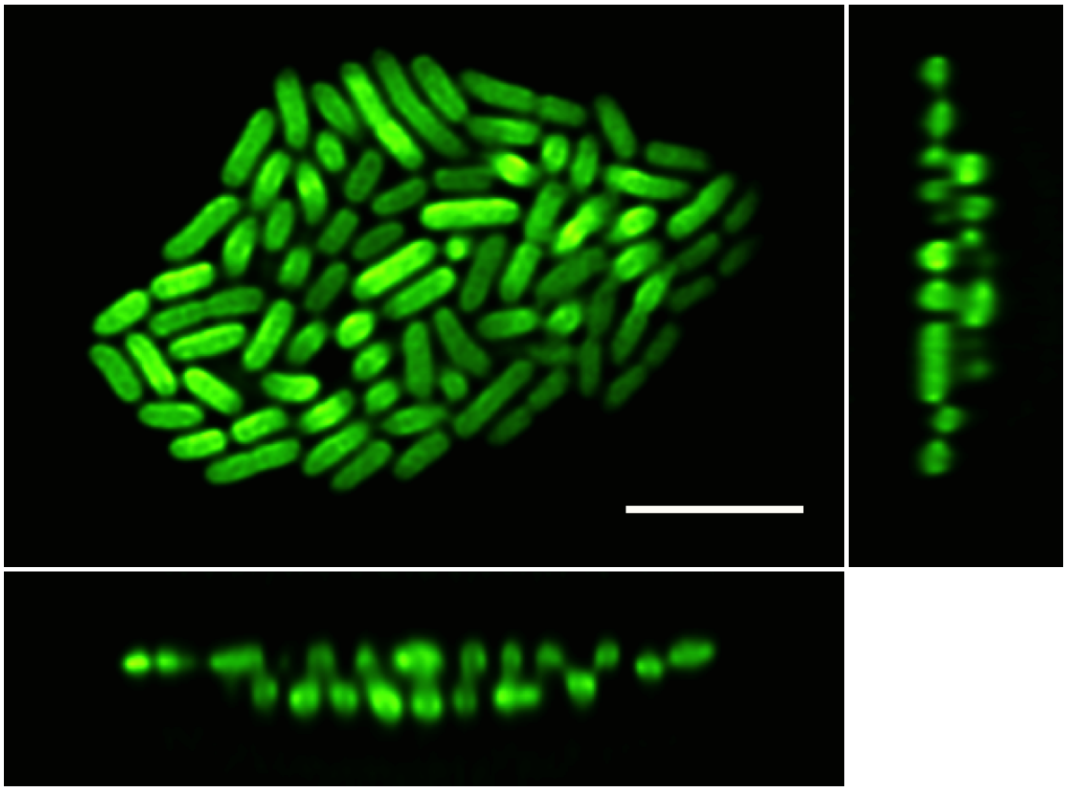

Figure 4.7: Bacterial colony grown on 2 % M9 agarose, deconvolved using measured point spread function (Figure 4.6). Individual bacteria are clearly distinguishable in the xy plane, as in the case of the raw confocal stacks. The distinction between bacteria in the axial direction is greatly enhanced. Despite some bacteria appearing to be merged together due to the deconvolution, the points of local maxima (used to locate the backbone for the bacterium) are more clearly separated than in the case of the raw confocal stack. Scale bar is 5.0 µm. A 3D rendering of this figure is available as Supplementary Movie A.1 (p. 130).

Deconvolving a stack taken through a bacterial colony grown in 2 % M9 agarose with the PSF measured in Figure 4.6 produces Figure 4.7. As is the case with the raw confocal stacks (Figure 4.3 p. 38), individual bacteria are clearly visible in the xy plane, separated from their adjacent neighbours. The separation of individual bacteria is now more apparent. Similarly, the distinction between bacteria in the axial direction is greatly enhanced when compared to the raw confocal stacks with clear separation between the two layers of bacteria. In the orthogonal slices, some bacteria appear to have been partially merged together between layers, with some blurring apparent, which is particularly visible between the two layers in the yz orthogonal slice (righthand of Figure 4.6), however, the local maxima of each bacterium, used by the code to define the backbone across which the spherocylinder outline is fitted, are more clearly separated than in the case of the raw confocal stack. As a result, reconstruction of the colony by the code is far more successful than when directly performed on the

raw confocal stacks. Figure 4.8 shows the successful identification, by the code, of two layers of bacteria, the primary layer (seen in the top image alongside the accompanying orthogonal profiles) is the layer growing closest to the coverslip through which imaging occurs and a second layer (bottom image), where bacteria have buckled into the agarose. Despite the apparent merging of bacteria seen in Figure 4.7, the local maxima are distinct enough from each other in the stack to be separable by the code and therefore to locate individual backbone structures (yellow) to which the code can fit a spherocylinder outline (purple) with a 100 % success rate.

4.2.2 Limitations of deconvolution

While deconvolution is a useful tool in the enhancement of densely packed structures such as bacterial colonies, there are caveats that need to be considered when analysing deconvolved images. As deconvolution is heavily dependent upon the PSF that is used, the use of an incorrect PSF will result in mis-representation of the perfect image. For instance, a PSF that is generated from a fluorescent bead with a diameter that is above the resolution of the microscope will result in an overestimation of the aberrations of the system. Consequently, when performing deconvolution on the acquired image stacks the dimensions of the resulting structures in the stack will be smaller than they should be, as the PSF will remove signal which represents the sample as well as that caused by aberrations in the system. This is particularly important when attempting to resolve structures that are very close to the resolution limit of the microscope, since the relative sizes are of a similar order of magnitude. Consequently, care must be taken in ensuring that the PSF is indeed a good representation of the system.

4.2.3 Optimisation of confocal microscopy for colony imaging

The quality of image in Figure 4.7 (p. 44) is reproducible across all images acquired as part of these experiments. To achieve routine success requires optimisation of several other factors. Firstly, in order to limit the effect of digital noise, the pixel size of the PMT used to acquire the signal must be smaller than the resolution of the confocal microscope in the focal plane (i.e. better than 140 nm). In theory, reducing the pixel size of the PMT below the resolution of the confocal provides no additional information on the bacterium's position, however, it does allow the deconvolution of the image to render a better quality image. It is vital, though, when considering the pixel size of the PMT that the effect of photobleaching and phototoxicity to the sample is considered. By reducing the pixel dimensions on the PMT, the scan area over which the beam illuminates the sample is similarly reduced meaning the size of the image may need to be increased in order to visualise the entire colony, causing the acquisition time (and

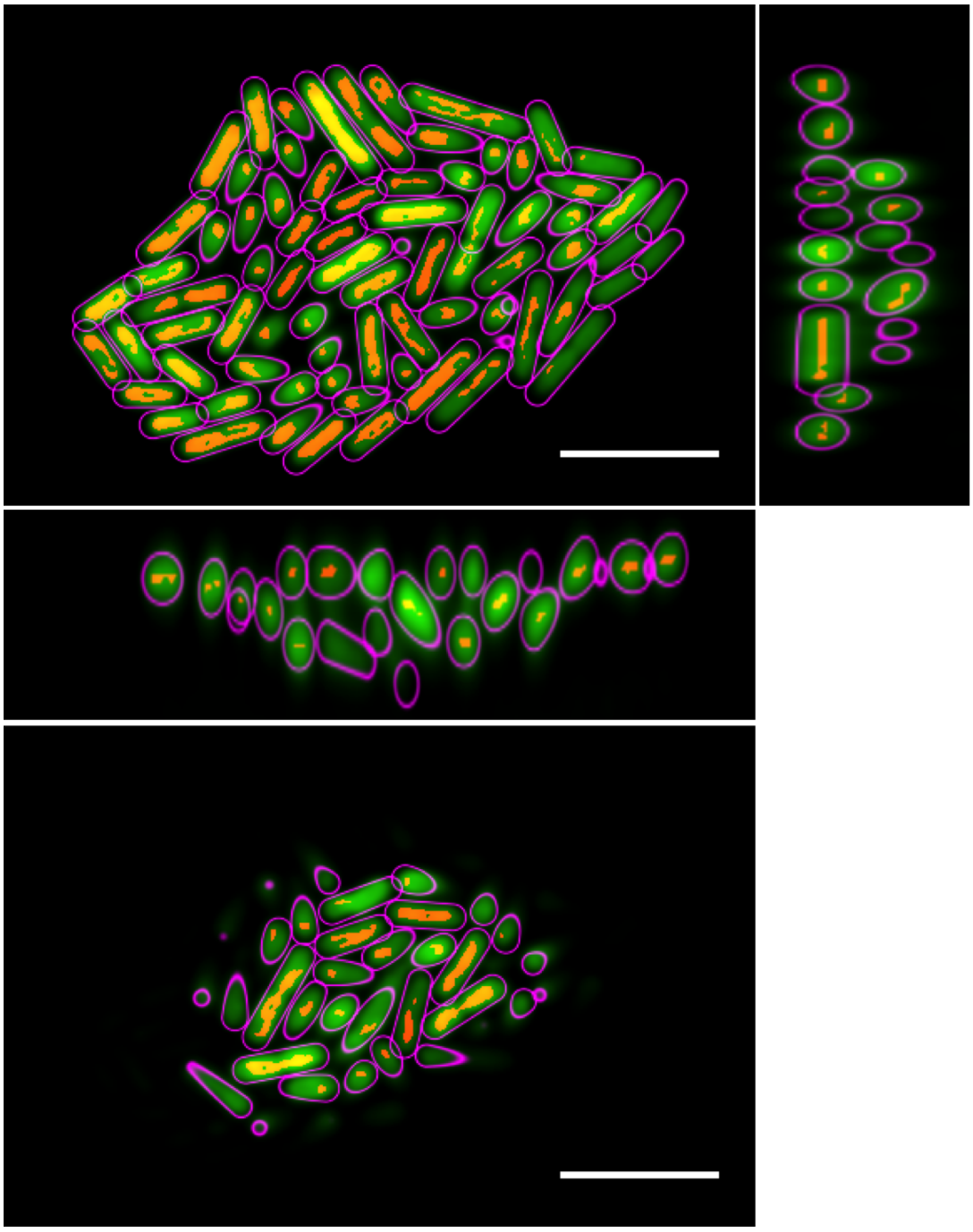

Figure 4.8: Reconstruction output of a bacterial colony grown on 2 % M9 agarose which has been deconvolved using the measured PSF (Figure 4.6, p. 43). The code successfully identifies two layers of bacteria, the primary layer (top) and a secondary layer (bottom image), fitting backbones (yellow) to the local maxima within each bacteria (green) before fitting a spherocylinder outline (purple) to each. Despite the apparent merging of bacteria (seen in Figure 4.7, p. 44) the code successfully distinguishes all bacteria in recognisable form. Scale bar is 5.0 µm. A 3D rendering of this Figure is available as Supplementary Movie A.2 (p. 130).

therefore the length of time the sample is illuminated) to increase substantially. Being probed by laser radiation for increased periods of time will not only result in samples losing fluorescence, as a result of photobleaching, but will also, in many cases, result in phototoxicity of the bacterial culture or, perhaps worse, disruption of the natural growth mechanisms resulting in filamentous or unhealthy samples. Therefore, a compromise is required in order to obtain a suitable resolution while not compromising the integrity of the sample. Experimentation with the parameters of the confocal microscope suggests that a pixel dimension in the focal plane of between 50 nm to 70 nm is suitable for achieving high resolution images, while ensuring the sample remains viable.

Similarly, the pixel size in the axial direction must also be below the resolution of the confocal in the axial direction (better than $\simeq$ 300 nm) in order to achieve the best possible results from deconvolution of the acquired image. The confocal microscope takes sections through the sample by moving the sample stage in the axial direction, changing the position of the focal plane in the sample and, as a result, when imaging with an oil immersion lens, the oil between the objective and the coverslip is squashed or stretched each time the relative distance between the objective and sample is altered. This variation causes an increase in the drift associated with high magnification oil immersion objectives leading to the focal plane of the sample drifting out of the stack window. Additionally, reducing the step size between slices increases the time the sample is illuminated, thus increasing the likelihood of photobleaching or phototoxicity occurring. Consequently, it is important that, as in the lateral case, a compromise is achieved. For experiments in this thesis into the growth of bacterial colonies in viscoelastic media, altering the focal plane at 100 nm intervals was found to provide sufficient improvement in the optical resolution after deconvolution without compromising the viability of the sample. Selecting pixel dimensions of 50 nm to 70 nm in the focal plane and 100 nm along the optical axis (or roughly 2-3 times smaller than the resolution limit of the microscope) allows an improvement in image quality of approximately 1.5$\times$ the raw image.

4.2.4 Limitations of reconstruction

Single bacterial resolution reconstruction has been successful for bacterial colony experiments conducted in this thesis. However, there are several limitations to the information extractable from a reconstruction model which fits rigid rods to individual bacteria, notably the lack of bending in the sample, length and diameter discrepancy and loss of signal. These are discussed in the following section.

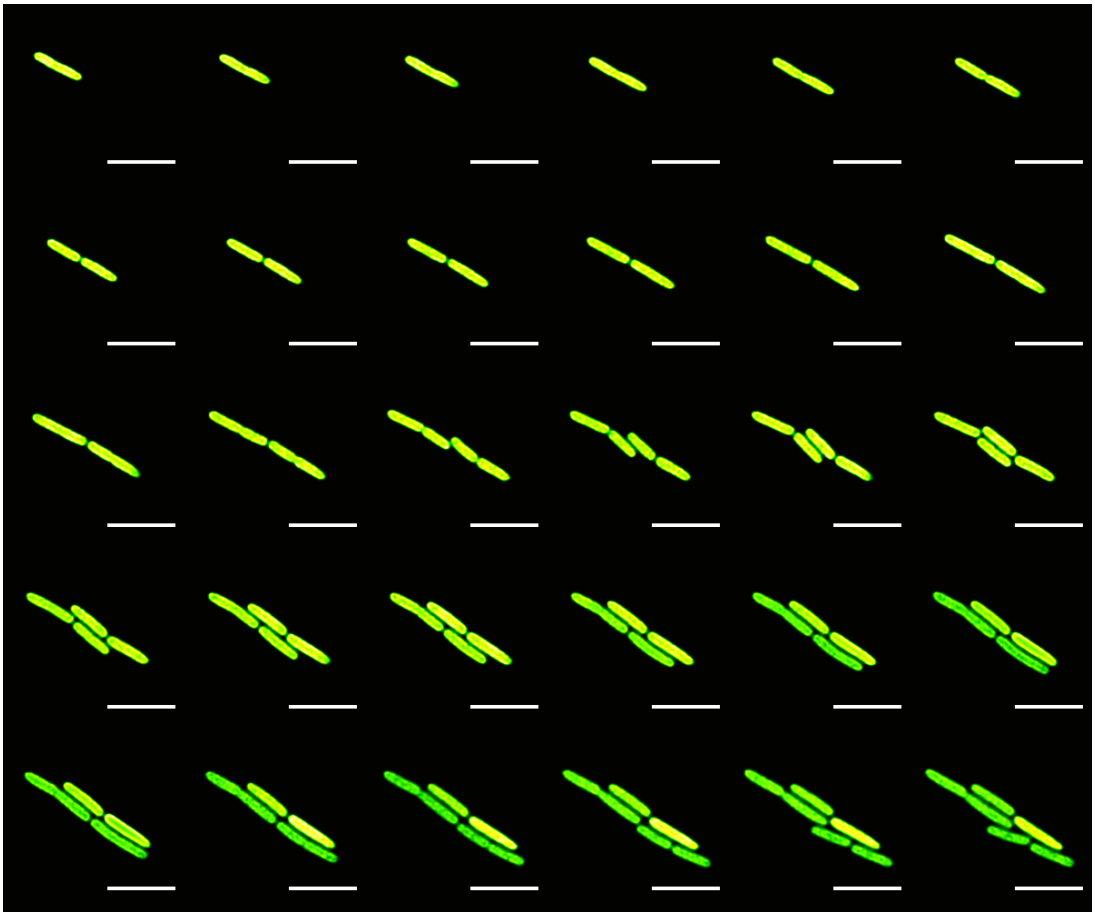

Figure 4.9: Time-lapse confocal microscopy image of a bacterial colony grown on 3 % M9 agarose. Stacks are recorded every 5 min (10 min intervals shown here) showing 2D growth of the colony. Study of the images reveals some bacteria exhibit deviation from the normal spherocylinder geometry. Frames exhibiting large deviation of a bacterium from the spherocylinder geometry are reproduced in Figure 4.10. Scale bar is 5.0 µm. A full collection of this montage is available as Supplementary Movie A.3 (p. 131).

Bending

The first, and most stark of the limitations associated with the use of Besseling and Hermes' code [111] is the approximation of a spherocylinder for the shape of a *E. coli* bacterium in the colony. To a first approximation, isolated *E. coli* bacteria do take the form of a spherocylinder, particularly when growing in bulk solutions. However, when growing on agarose the *E. coli* are seen to bend away from a straight spherocylindrical shape. This bending occurs primarily as a bacterium negotiates obstacles in its path, such as other bacteria, which restrict the growth. Figure 4.9 shows images recorded from the confocal microscope stacks at 10 min intervals as a bacterial colony grows on a 3 % M9 agarose surface. The majority of the bacteria exhibit normal spherocylinder

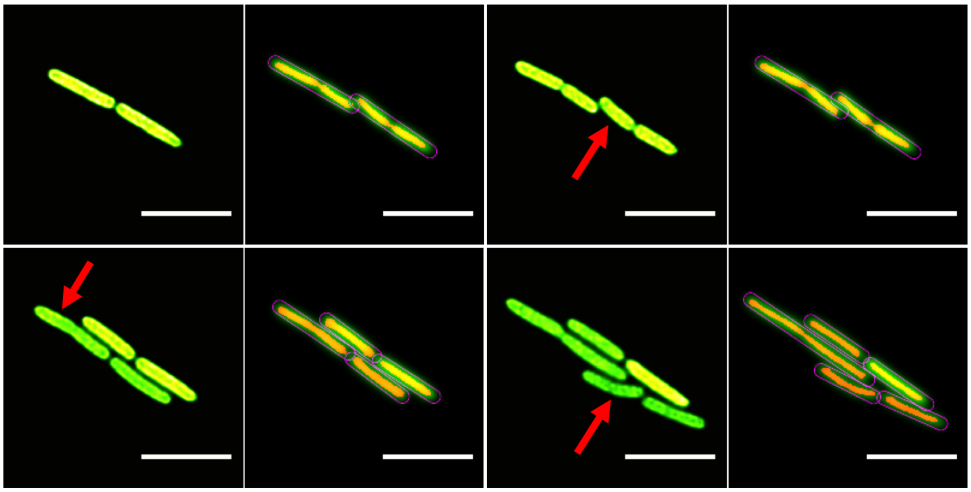

Figure 4.10: Time-lapse confocal microscopy of a bacterial colony grown on 3 % M9 agarose taken from Figure 4.9. Red arrows indicate bacteria which deviate from the spherocylinder shape. Output from the code is shown to the right of each of the raw images. The code fits straight spherocylinders to all bacteria resulting in curvature information being lost. For most bacteria the loss of information is trivial, but some bacteria (red) clearly deviate from a straight spherocylinder, a fact which is omitted by the reconstruction. Scale bar is 5.0 µm

geometry with the cylindrical body appearing straight, however, close study of the images as a whole reveal several occasions when spherocylindrical geometry is lost and the bacterium bends. Figure 4.10 shows four images from Figure 4.9, the top left image showing spherocylindrical geometry of the bacteria, where both bacteria are straight and the other three images show one bacterium in the colony that has deviated from spherocylindrical geometry and is bending (red arrow). Despite some bacteria showing clear evidence of deviation from the spherocylinder geometry, the reconstruction code does not take this into account. In fact, the code utilises deviation from a straight rod fit to distinguish between individual backbones fitted along a bacterium which are close to each other spatially. Consequently, there is a loss of information, and the potential for errors in the form of mistaken orientation information.

Figure 4.11 shows the corresponding stills from Figure 4.10 analysed through code developed by Dario Miroli, which attempts to resolve this issue by adaptation of algorithms used for fitting outlines in 3D to each of the bacteria in the colony. Rather than fitting a backbone along a set of local maxima in a bacterium, the code fits an outline to the bacterium through extensive thresholding and rethresholding of the image. While results proved promising on this test data set, consistency across different measurements proved problematic and subsequently work in this area is ongoing. One major advantage of this code, apart from the rendering of the outline of the bacterium

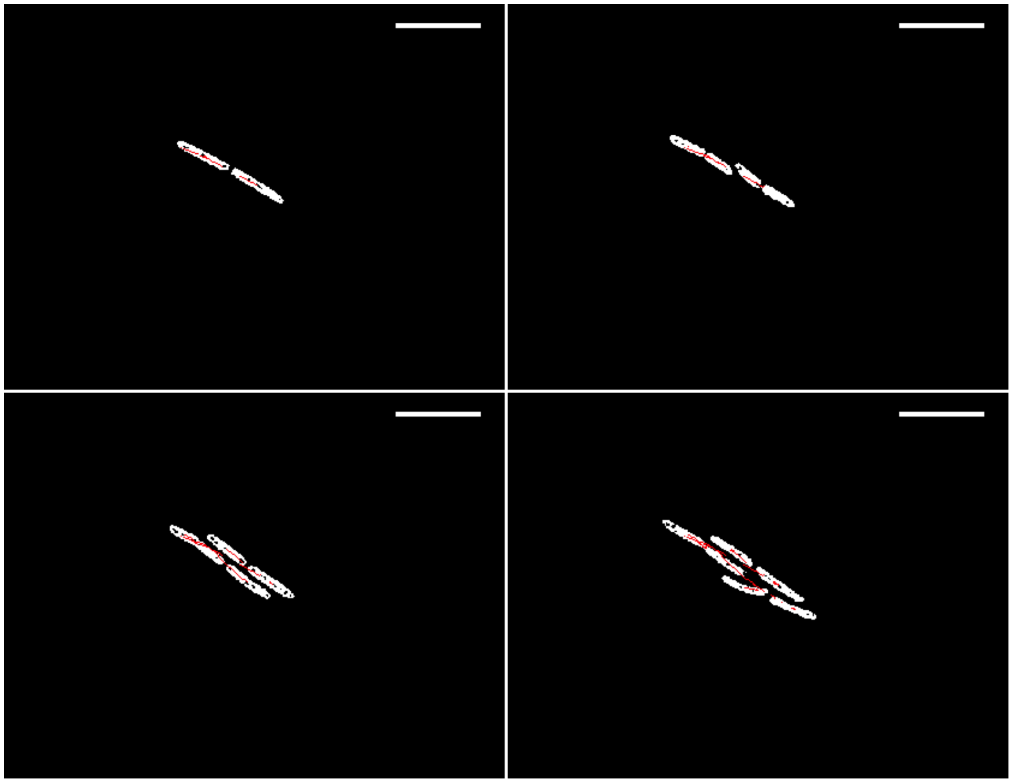

Figure 4.11: Code developed by Dario Miroli, fitting directly to the outline of the bacterium rather than fitting a spherocylinder. The four stills from Figure 4.10 are reproduced for direct comparison. The code successfully identifies the deviation from a straight line. Red lines show the historical position of individual bacteria within the colony. Scale bar is 5.0 µm. Full 2D (plus time) imaging of this Figure is available as Supplementary Movie A.4 (p. 131)

rather than fitting to a spherocylinder, is the integration of tracking code, developed initially by Crocker and Grier [119], allowing tracking of bacteria as a function of time as well as in three spatial dimensions. Future development in reconstruction code should be focussed on these routines with the expectation that full reconstruction of all bacteria in a microcolony, including the flexibility of the cell, will lead to a greater understanding of the mechanisms which instigate the buckling event.

Length

Due to the nature of the reconstruction code there is a discrepancy between the physical length of the bacteria and the measured length obtained by the code, which is dependent upon input parameters defined by the user for the cut-off intensity during the backbone pixel allocation. The reconstruction code measures a length of the bacterium which is defined as the length of the backbone. It is clear that this will underestimate the bacterial length by twice the radius of the hemispherical cap fitted to the cylinder

(Figure 4.8, p. 46). A simple correction is to add the radius of these hemispherical caps to the outputted length of the bacterium, which is done for all measurements of length in this thesis.

Diameter

Similarly, the reconstruction code is heavily constrained in the measurements of the spherocylinder diameter, since for each stack analysed through the code, a global diameter (assigned to all the bacteria in the stack) is selected by varying the parameter from 400 nm to 1000 nm. All the diameters are therefore constrained to be identical at a single time-point. Since one of the main parameters used to distinguish a true bacteria from noise and distortions in the acquired image is this fixed diameter, reworking of the code is required in order to produce similarly accurate results while extracting the true diameter, and, although many interesting questions can be asked on the consistency of the diameter of *E. coli*, this work is out of the scope of this thesis. However, other studies have shown that the diameter is far less polydisperse than the length in *E. coli* [120–122].

Loss of Signal

In a bacterial colony, the intensity of the GFP expressing plasmid varies considerably due to heterogeneity of the plasmid copy in specific bacteria, meaning that each bacterium contains a different number of GFP expressing plasmids. Reconstruction overcomes this problem by defining a local maximum and locating the point where the intensity drops below a fraction of this maxima to distinguish the bacterium. However, imaging bacterial colonies over an extended period of time using fluorescence microscopy, particularly laser scanning microscopy, can lead to phototoxicity and photodamage to the bacteria. While photodamage is limited through the use of low laser powers, over the course of an experiment (approximately a 24 hr timescale) the fluorescent signal from each bacterium diminishes. Data sets exhibiting loss of signal from a bacterium within the colony are discounted from analysis due to the significant loss of information of the colony features.

Similarly, a reduction in the intensity of fluorescence of bacteria in the colony makes the reconstruction of the colony far more complicated. Due to the decrease in local maxima, relative to the maximum intensity measurable by the PMTs, the code becomes more sensitive to input parameter settings, which can lead to interpretation of noise within the PMT background as individual bacteria and population overcount. It is therefore essential that care is taken in order to ensure this does not happen, particularly when

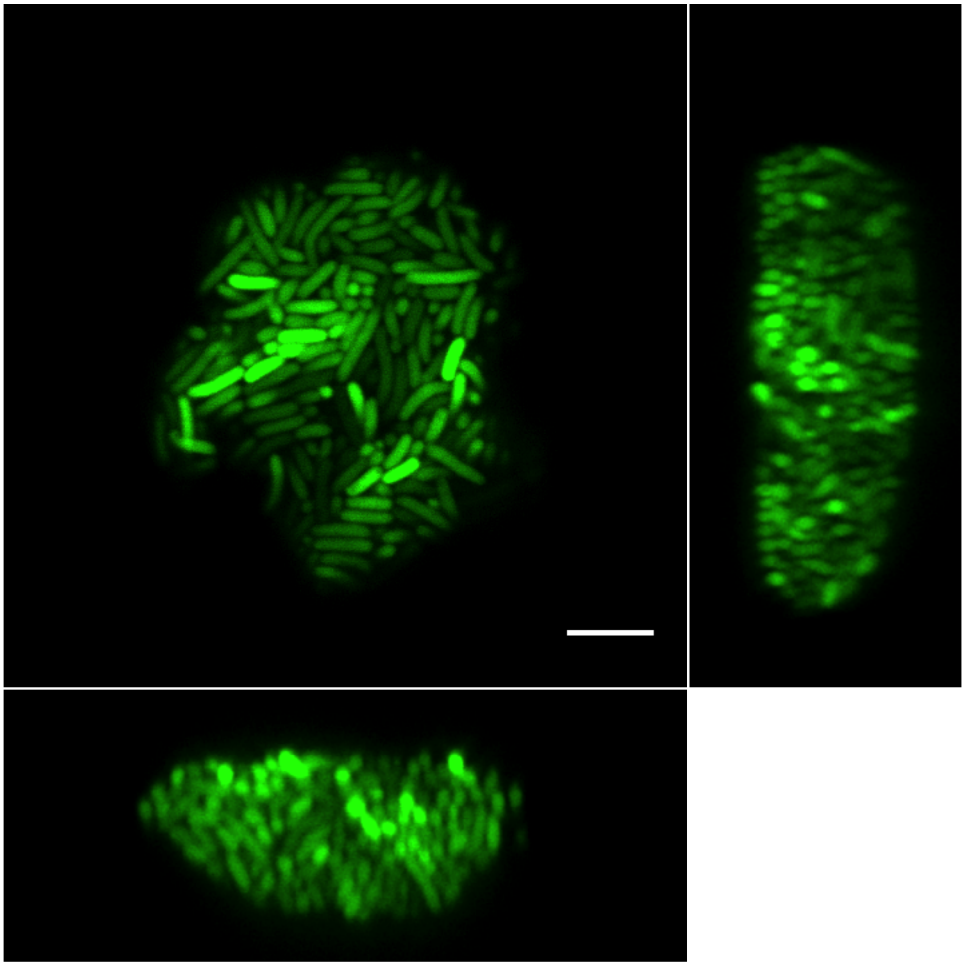

Figure 4.12: A single *E. coli* MG1655 bacterial colony grown fully submerged within 2 % M9 agarose gel. Individual bacteria are clearly distinguishable throughout the colony, even when imaging through multiple layers of bacteria which are highly divergent media. Colonies such as these have been successfully reconstructed using code, as with the surface bacterial colonies, showing the possibility of the extension of the method to investigating fully 3D systems. Scale bar is 5.0 µm. See Supplementary Movie A.5 (p. 132) for a 3D rendering of this figure.

automating analysis.

4.3 Applications of the reconstruction method

Despite these limitations, the reconstruction of bacterial colonies growing in viscoelastic media has proved successful up to 5 layers of bacteria (Figure 4.12). As well as the ability to successfully reconstruct bacterial colonies growing on an agarose gel surface at single bacterial resolution, there is the possibility to extend this technique to the investigation of bacterial colonies fully submerged in agarose gels.

Figure 4.13 shows a confocal stack of fully submerged bacterial colonies in 2 % M9 agarose. Bacteria on the surface of the agarose have grown in a chain fashion (seen in

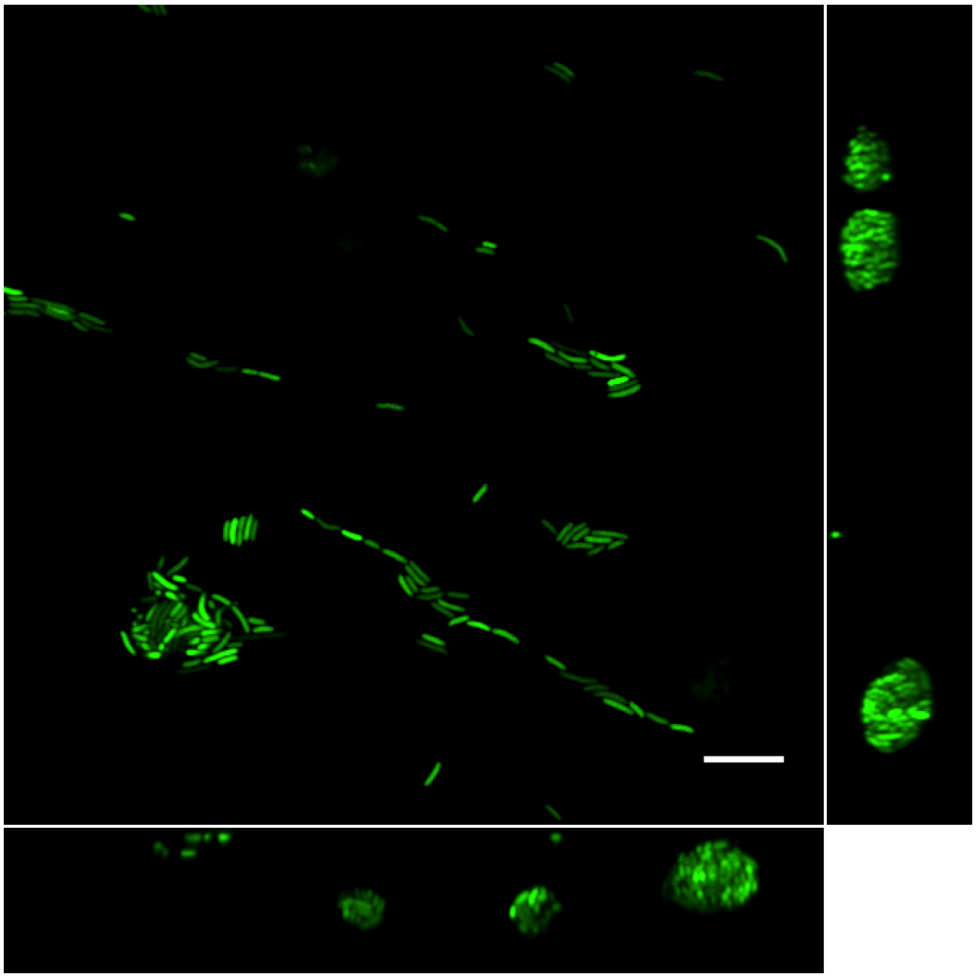

Figure 4.13: *E. coli* MG1655 bacterial colonies grown fully submerged with 2 % M9 agarose gel. Individual bacteria present on the surface of the agarose are seen to grow in chains, whilst those submerged in the agarose have formed spherical colonies. Individual bacteria are clearly distinguishable within the colony. Scale bar is 10.0 µm. A 3D version of this figure is available as Supplementary Movie A.6 (p. 133).

the xy plane), whilst those submerged have formed near spherical colonies and, in all cases, individual bacteria are clearly visible within the colonies. Similarly, Figure 4.12 shows a single submerged bacterial colony in 2 % M9 agarose and, as with Figure 4.13, individual bacteria are clearly visible in the colony at a resolution suitable for image analysis using reconstruction code. Reconstruction of one of these colonies is shown in Figure 4.14 (p. 55), where the colony is seen to form a spherical ball of bacteria.

One of the primary motivations for investigations of fully submerged bacterial colonies

is the reduction in complexity of the models which can be used to predict such structures due to two interlinked factors:

(i) the increased symmetry of the system

(ii) the ability to neglect boundary effects due to the coverslip-bacteria and coverslip-agarose interactions

The former means that, aside from a bias in the initial growth plane of the bacterium, dictated by the initial orientation of the rod-shaped cell, the system is symmetric in all directions. This allows, in theory, equal probability of the bacteria invading the surrounding agarose in all directions. For the latter, not needing to consider the effect of the coverslip on the colony growth again significantly reduces the complexity for modelling of these systems, particularly when wishing to consider bacterium-bacterium interactions directly. Experiments have been conducted in this group by a masters student, Michal Tomaszewski, working under the supervision of Bartloiej Waclaw, on the imaging of fully submerged bacterial colonies but, as with those experiments conducted on surface growing colonies, single bacterial resolution has proved difficult to obtain. It is hoped that through an extension of the work carried out here the ability to fully reconstruct completely submerged bacterial colonies at the resolution of single bacteria will be realised in the near future.

4.4 Discussion and conclusions

This chapter provides an outline of the processes necessary after image acquisition in order to successfully reconstruct bacterial colonies in 3D and time at single bacterium resolution. These methods are used throughout this thesis to obtain quantitative information on the growth and development of bacteria on agarose, both individually (Chapter 5 p. 57) and in a colony (Chapter 6, p. 75). The reconstruction has proved more than suitable for successful identification of individual bacteria in dense structures such as surface colonies, and this method has proved successful in reconstructing bacterial colonies which are buried in agarose at a single bacterium level to high precision.

Throughout the chapter, areas requiring additional research have been discussed, and paths for the exploration of these areas have been provided, with perhaps the most pressing one being the development of software to directly link and track bacterial lineages through the colony. While the reconstruction software performs admirably in the cases outlined above there are limitations to it, particularly in the loss of

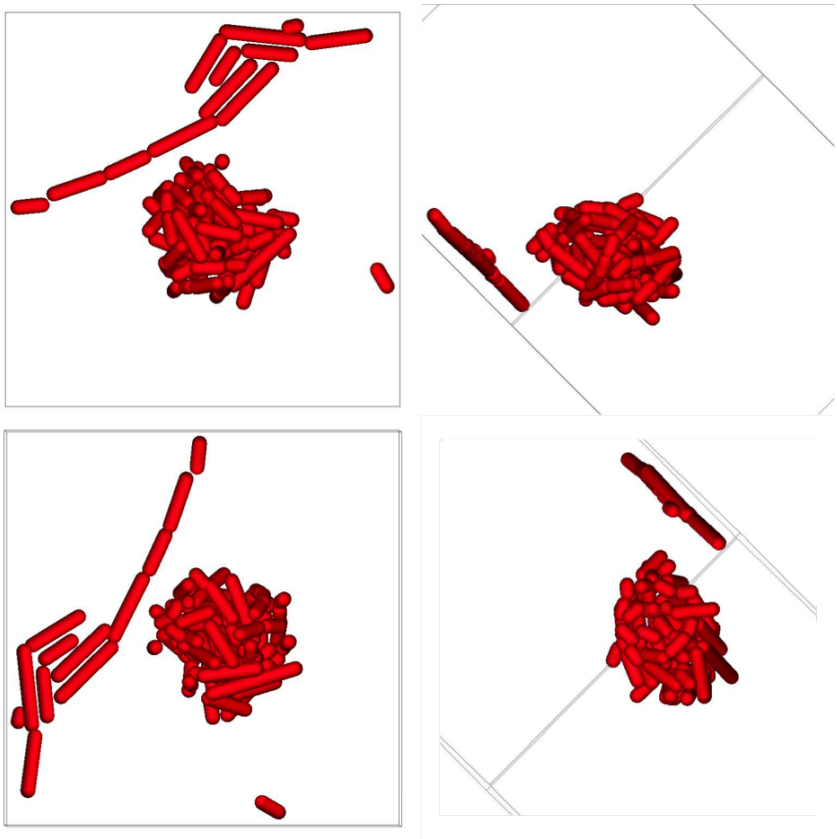

Figure 4.14: Reconstruction of fully submerged bacterial colony grown within 2 % M9 agarose. Stills are taken from visualisation software developed by Michiel Hermes to visualise the output from the reconstruction code. Bacteria are clearly distinguishable on a single bacterial resolution. The bacteria form a spherical colony and are seen to be submerged below the surface of the agarose (identifiable by the linear bacteria structure visible in the frames). No clear bias can be seen for the growth of the bacterial colony in any direction in this case. The full movie of this reconstruction is available as Supplementary Movie A.7 (p. 134).

information regarding the curvature of the bacteria throughout the colony development. Addressing this would provide considerably more information on the physical properties governing the growth of bacteria as the colony becomes larger and spatial constraints are increased.

In conclusion, confocal microscopy, with the enhancements in image acquisition and post-acquisition processing outlined in this Chapter, provides a suitable imaging platform for obtaining high-precision, single cell resolution images of densely packed bacterial colonies. When these stacks of images are combined with deconvolution and reconstruction software the extraction of physical, geometrical parameters of individual bacteria in the colony is possible.

Chapter 5

Initial growth

5.1 Overview

In the laboratory, bacterial colonies are generally grown on agar plates (a circular petri dish holding a gel substance containing all of the nutrients necessary for bacterial growth). This is the case for all experiments which have been conducted in this thesis. While many references are made in literature to how colonies of bacteria grow on agar (or indeed agarose)[1], little is known about the precise position a bacterium has in relation to the surface of the agar upon which it grows [123]. There are three potential ways in which bacteria may be on the surface of an agar plate (Figure 5.1):

(A) The bacterium lies on top of the agarose layer with only the bottom surface of the bacterium touching the agarose surface

(B) The bacterium is partially submerged into the agarose surface

(C) The bacterium is completely buried in the agarose with the top surface of the bacterium parallel to and level with the surface of the agarose

Whether the bacteria sit on-top, are partially submerged or are fully submerged within the agarose has significance when considering the physics involved in the growth and division of the bacterium as it develops into a colony, particularly the force exerted by the bacterium and by the agarose in confining the bacterium.

In order to answer this question it is necessary to be able to precisely locate the bacterium as it is positioned on an agarose layer. To do this, samples of *E.*

[1] Agarose is one of the two principle components of agar (which also consists of agaropectin) and is a linear polymer made up of a repeating monomer unit of agarobiose. The agarose used in this thesis is Invitrogen Ultrapure Agarose obtained from LifeTechnologies `https://www.lifetechnologies.com/order/catalog/product/16500500`

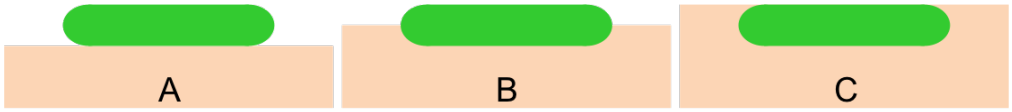

Figure 5.1: The potential positions of a bacterium on an agarose pad. (A) The bacterium sits on top of the agarose surface with only the base of the bacterium adjacent to the surface. (B) the bacterium is partially submerged within the surface. (C) The entire bacterium is immersed (buried) within the agar with the top surface of the bacterium parallel to and level with the agarose surface.

coli expressing the pcH60 plasmid, a tetracycline resistant plasmid containing green fluorescent protein (GFP), were prepared and plated on M9 media with agarose weight concentration of 2 %. Since M9 is a low fluorescing media, in order to directly image the agarose pad it was necessary to add a fluorescent marker to the agarose and Rhodamine B (Rho. B) was selected due to overlap of the excitation spectra with GFP (Figure 5.2A). In later experiments, Nile Blue was used as a complementary fluorescent marker for the imaging of the agarose, due to the low cross-talk between Nile Blue and GFP (Figure 5.2B), and the tendency of Rho. B to accumulate at the surface of bacteria, inhibiting growth [124]. Using the laser scanning confocal microscope, excitation of the GFP in the bacteria was performed using laser light of wavelength 488 nm and Nile Blue excited with wavelength 639 nm, giving good fluorescence in both the GFP and Nile Blue channels.

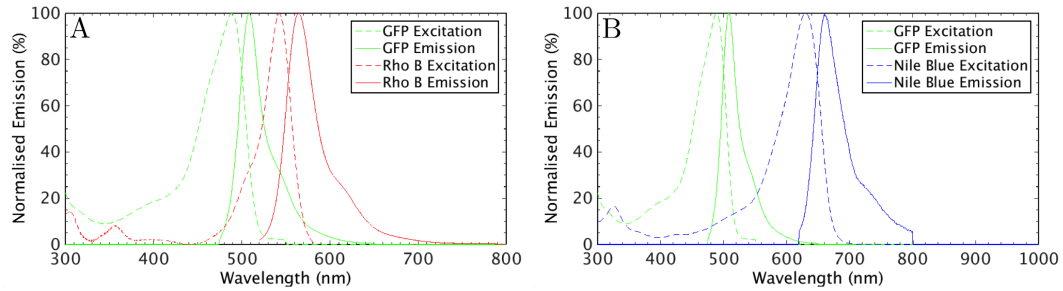

Figure 5.2: [A] Excitation and emission spectra of green fluorescent protein (GFP) and Rhodamine B (Rho. B). Rho. B was selected due to the overlap of the excitation spectra of GFP and Rho. B, so that excitation could be simultaneous without the need to introduce additional laser light into the system.
[B] Excitation and emission spectra of GFP and Nile Blue. GFP and Nile Blue emission spectra are removed enough from each other to reduce to a minimum the cross-talk associated with the two fluorescent tags. Reproduced from [125].

The effect of the coverslip on the position of the bacterium relative to the agarose was investigated by preparing samples (§ 3.2.3, p. 27), with a thin layer (<10 µm) of Rho. B doped agarose placed directly on a coverslip. The bacterial culture was then

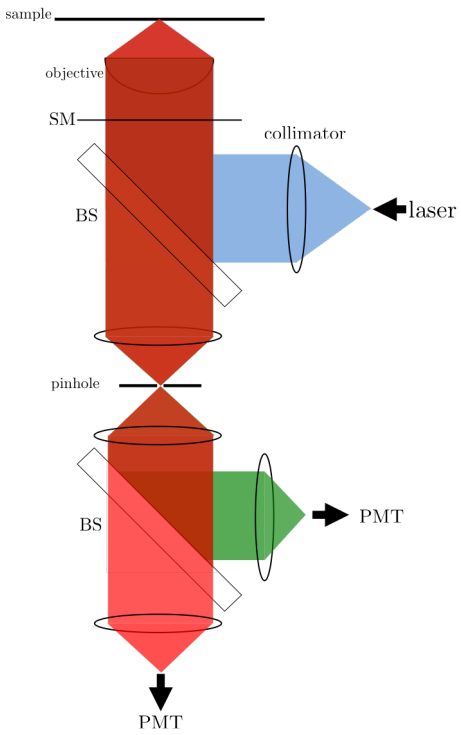

Figure 5.3: Confocal setup for simultaneous imaging of GFP (green) and Rho. B or Nile B (red). The use of two PMTs within the confocal allowed rapid acquisition of both channels simultaneously.

pipetted onto the surface of the agarose and imaged through the agarose layer from below.

5.2 Imaging methods

Simultaneous acquisition of Rho. B and GFP or Nile B and GFP fluorescence was made using the confocal microscope (§ 2.2.2, p. 11), with stacks being taken through the sample with an axial separation of 0.05 µm. Figure 5.3 shows a schematic for the experimental setup used to achieve this. Two PMTs in the confocal microscope were utilised to allow rapid acquisition of the 3D structure of the agarose and *E. coli*, with GFP signal obtained in Channel 1 and either Rho. B or Nile Blue in Channel 2.

5.3 Position of a bacterium on an agarose plate

5.3.1 Open samples

Confocal imaging of the open sample through the thin agarose pad immediately after the culture has been placed on the surface allows us to observe how the bacterial cell sits on the agarose. By taking slices at 0.05 µm intervals through the sample, a 3D picture of the position of the bacterium relative to the surface of the agarose can be made (Figure 5.4).

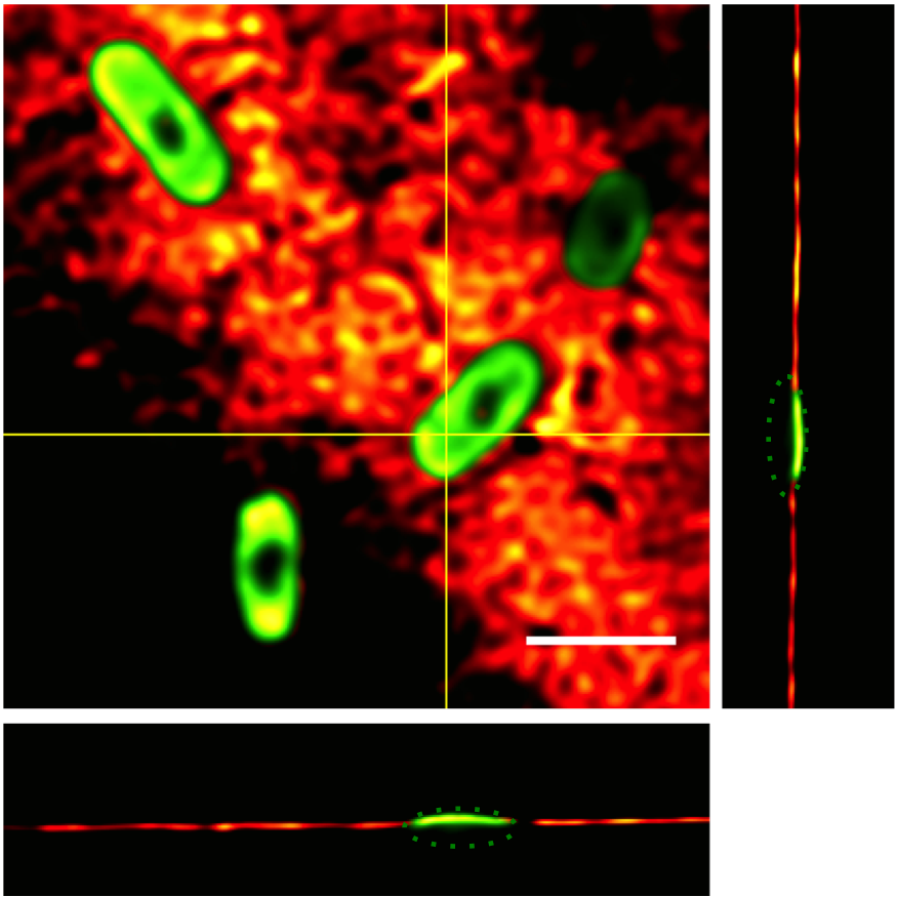

Figure 5.4: Confocal image of bacteria (green) on M9 agarose (red) with a 2 % (weight) concentration immediately after pipetting onto the surface. The axial views clearly show the bacterium is partially buried in the agarose, the surface of which shows up bright red due to the increase in concentration of Rhodamine B at the air-agarose interface. Close inspection of the sample reveals the bacteria are not completely submerged in the agarose but rather have approximately one quarter of their volume above the surface. An outline of the bacterium is included (green dotted line) in the orthogonal views as an approximate aid to the eye. Scale bar is 2.0 µm. Orthogonal slices are taken every 0.05 µm through the sample.

Figure 5.4 shows bacteria (green) approximately 10 min after being pipetted onto the agarose (red) surface, with the orthogonal view through the bacterium (position denoted by the cross-hairs) indicating that rather than sitting directly on the agarose surface, the bacterium is partially submerged (approximately three-quarters of the volume) in the agarose. A green dotted line, indicating the outline of the bacterium, is included in the orthogonal views of Figure 5.4 as an aid to the eye.

Imaging of the agarose and bacteria in this configuration was hampered by the surfactant properties of Rho. B and its tendency to accumulate at the interface of two surfaces [124]. This is particularly evident in Figure 5.4 where the intensity of the Rho. B at the air/agarose interface is far greater than the intensity of the Rho. B in bulk agarose and consequently, it is difficult to distinguish the air and agarose bulk relative to the surface. For the xz orthogonal (below the main figure) the air is above the agarose (as imaged), for the yz orthogonal the air is to the right of the interface. Additionally, there is cross-talk between GFP and Rho. B due to the close proximity of their emission peaks (Figure 5.2A, p. 58), and the Rho. B channel dominates the combined images. This is a result of the need to acquire the Rho. B signal at a far higher gain setting than for the GFP, due to the diffuse nature of the Rho. B within the agarose and consequently it is only possible to faintly resolve the bottom of the bacterium, an area where only GFP emission is present. However, it is clear that the bacterium does not sit directly on the top of the agarose.

Studying the surface signal of the agarose relative to the bacterium it is also evident that the bacterium, is not entirely submerged in the agarose either, as seen by the increased height of the bacterium relative to the surface of the agarose, a finding which is confirmed when replacing Rho. B with Nile Blue as a fluorescence marker for the agarose pad (Figure 5.5). Unlike Figure 5.4, Figure 5.5 has not been deconvolved and the distortion in the axial direction is clearly evident, particularly due to the need to image through the bacterium and agarose in order to identify the top surface of the bacterium. As a result a clear tail is seen beyond the agarose-air interface for both orthogonal images, but the interface is again clearly evident, with approximately three quarters of the volume of the bacterium immersed below the agarose-air interface.

Time-dependence of position

The position of a bacterium relative to the surface of the coverslip is time-dependent for the period immediately after the culture is pipetted onto the agarose pad. As the bacterial culture is introduced to the agarose pad using a liquid culture, (phosphate

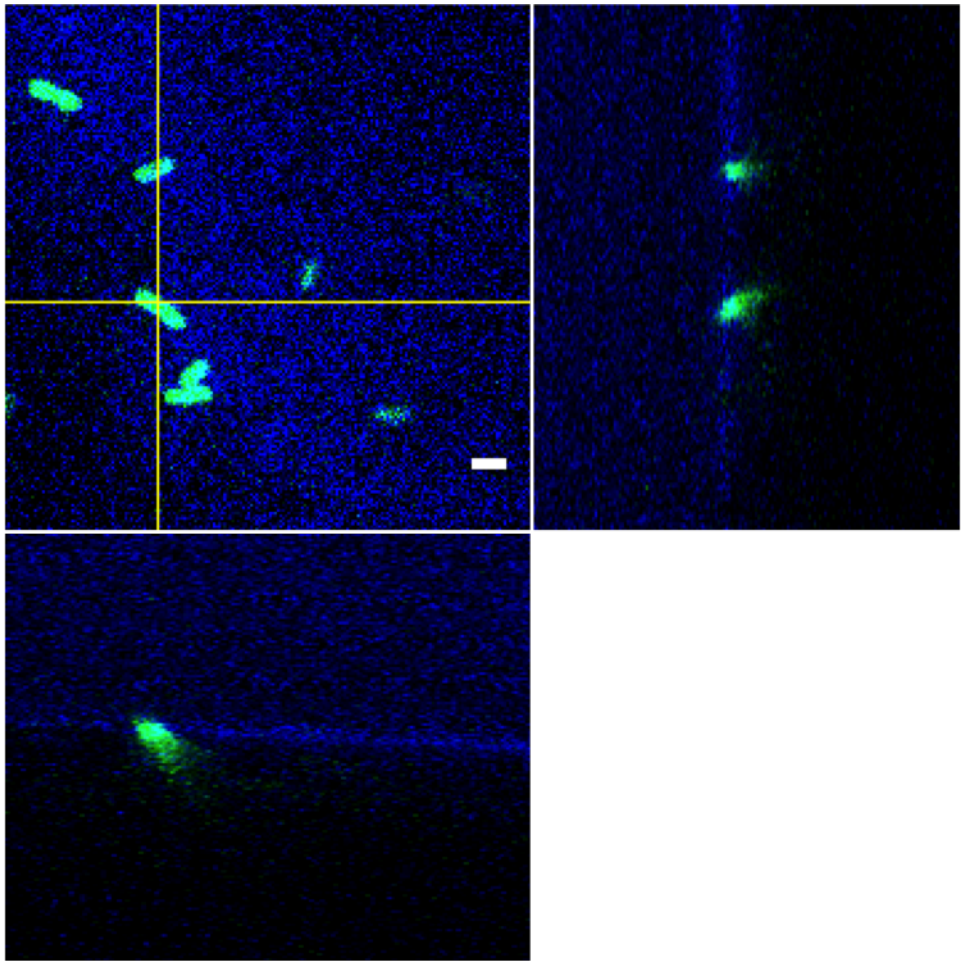

Figure 5.5: GFP plasmid expressing MG1655 *E. coli* position on an open agarose pad tagged with Nile Blue fluorescence. For the xz orthogonal (below the main figure) the air is above the agarose (as imaged), for the yz orthogonal the air is to the right of the interface. The bacterium does not sit directly on the surface but rather is partially submerged within the agarose layer. Scale bar is 2.0 µm. Orthogonal slices are taken every 0.05 µm through the sample.

buffer saline (PBS)), at the point of contact with the agarose pad the bacterium must be at rest on top of the agar (Figure 5.1A, p. 58). As the PBS solution evaporates the bacterium gradually sinks into the agarose pad up to the point visible in Figure 5.4. At this point the bacterium has approximately one quarter of its volume above the surface of the agarose pad and more closely approximates the schematic shown in Figure 5.1B.

From this point, as time increases, the proportion of the bacterium immersed remains constant, but unfortunately, in this case, due to the complexity of sample preparation, direct comparison of samples as a function of time is not possible, as the time required for acquisition of suitable quality images for analysis is of the order of the time frame

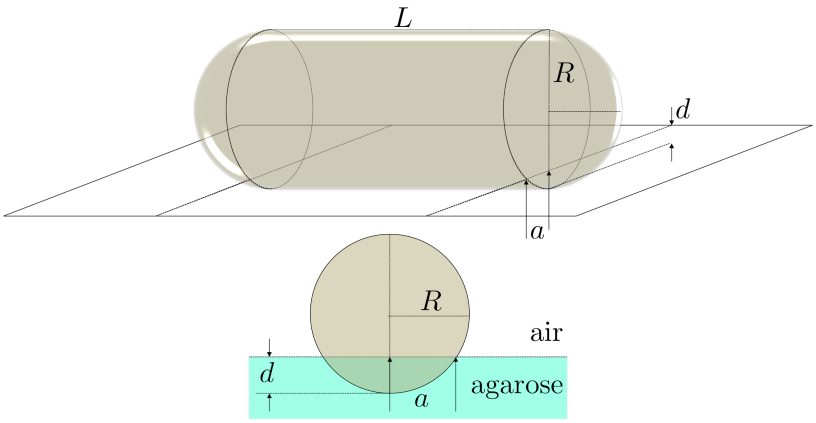

Figure 5.6: Schematic showing the parameters for calculation of Young's modulus of agarose using continuum mechanics in both 3D (top) and 2D (bottom). A bacterium can be approximated as a spherocylinder (a cylinder of length L with two hemispherical caps of radius R) and lies on an agarose surface at the air/agarose interface. The bacterium is seen to 'sink' into the agarose with a depth of penetration d resulting in a contact radius a. The contact radius is the proportion of the radius of the cylinder which is parallel to the surface of the agarose (i.e. when multiplied by the length of the cylinder produces the effective area which is pressing down on the agarose surface).

of the drying process. I believe the apparent 'sinking' of the bacterium into the agarose pad is due primarily to surface tension changes as the PBS evaporates. Initially, the agarose is covered either by PBS or by a bacterium. Since both PBS and bacteria are predominately water the surface tension of bacterium-agarose and PBS-agarose are approximately equal. However, as the PBS evaporates the PBS-agarose interface changes to an air-agarose interface which leads to a change in the surface tension relative to the bacterium-agarose interface and the subsequent sinking of the bacterium.

To verify this, the order of magnitude of the Young's modulus of the agarose can be calculated using continuum mechanics. By approximating the bacterium as a rigid cylinder of length L and radius R (Figure 5.6) which sinks into the agarose surface to a penetration depth of d, the bacterium has an effective contact area on the agarose surface of $2La$, where a is the contact radius of the bacterium. Using these parameters, the strain exerted on the agarose, ϵ, can be approximated as

$$\epsilon \approx \frac{d}{2a} \tag{5.1}$$

leading to an order of magnitude estimation of the stress σ as

$$\sigma \approx \frac{Ed}{2a} \tag{5.2}$$

where E is the Young's modulus of the agarose. The force F exerted on the agarose by the bacterium can therefore been written as

$$F = \frac{\pi}{4} E^* L d \tag{5.3}$$

where E^* is the reduced Young's modulus and is defined by

$$E^* = \frac{E}{1 - \nu^2} \tag{5.4}$$

where ν is the Poisson's Ratio of the agarose.

Similarly the force can be written in terms of the surface tension γ of the interface between the air and agarose and the radius of the cylinder as

$$F = \frac{\gamma}{R} 2La \tag{5.5}$$

where $2La$ is the effective area of contact of the cylinder to the agarose.

Equating Eq. 5.3 and Eq. 5.5 and rearranging gives

$$E^* = \frac{8\gamma}{\pi d} \frac{a}{R} \tag{5.6}$$

which can be simplified in this case as the bacterium penetrates the agarose by approximately three-quarters of the volume meaning $a = R$ and

$$E^* = \frac{8\gamma}{\pi d} \tag{5.7}$$

The surface tension of a water/air interface is approximately $70\,\mathrm{mN\,m^{-1}}$ and the penetration distance is $0.75 \times 0.8\,\mu\mathrm{m} = 0.6\,\mu\mathrm{m}$ giving a value of $E^* \approx 300\,\mathrm{kPa}$. There are a limited number of studies measuring the elastic properties of agarose gels with many interested in the properties on a macro scale taking a value $\nu = 0.5$. However, Geissler *et al.* measure $\nu = 0.32$ [126] which when applied to Eq. 5.4 gives a value of $E = 270\,\mathrm{kPa}$. Both E and E^* are in close agreement with measurements of the Young's modulus of agarose gels made in the literature (Appendix D, p. 143) where values range from a few kPa to MPa.

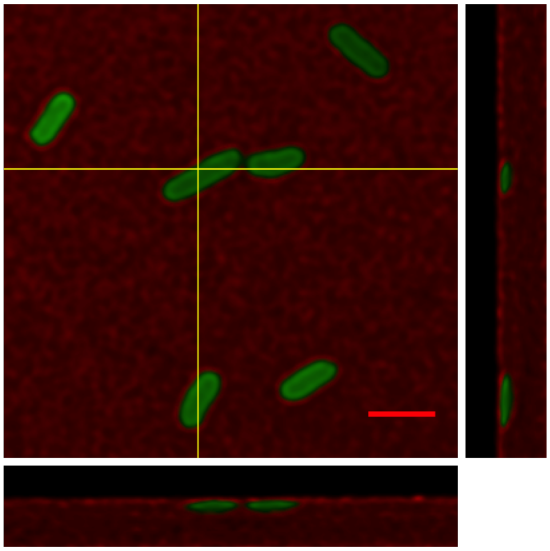

Figure 5.7: Two colour fluorescence confocal image of bacteria (green) on M9 agarose (red) with a 2 % (weight) concentration where the sample has been sealed with a coverslip. The bacteria are seen to be fully submerged within the agarose and are completely confined to a 2D layer by the coverslip. Scale bar is 2.0 µm. Orthogonal slices are taken every 0.05 µm through the sample.

5.3.2 Quasi-2D growth

In order to simplify the imaging process, reduce the effect of drying of the sample and to allow significant improvement of the image quality, bacterial colony experiments conducted in this group [91] (and also by Grant *et al.* [48]) are not exposed to the air, as in the open configuration. Instead the sample is sealed with the addition of a coverslip above the agarose surface. This is the geometry used for experiments in this thesis (§3.2.3, p. 27) and has the effect of restricting the growth of the bacterium to a 2D layer, which can be confined to the focal plane of the microscope, thus allowing the imaging of the sample using phase-contrast or brightfield microscopy, without the need to consider multiple layers of bacteria and is a well established method in the microbiology community [85].

However, it is unknown if the confinement is truly 2D, i.e. whether the coverslip is flush to the agarose pad or rather rests on the top of the bacterium, which is partially submerged in the agar. In order to resolve this confusion, confocal images were taken at 0.05 µm slices through a sample prepared on a microscope slide, with a coverslip sealing the agarose pad. From the resulting 3D stack (Figure 5.7) the bacteria (green) are clearly seen to be submerged in the agarose (red). Analysis of the orthogonal sections shows the top surface of the bacterium membrane is in line with the Rho. B

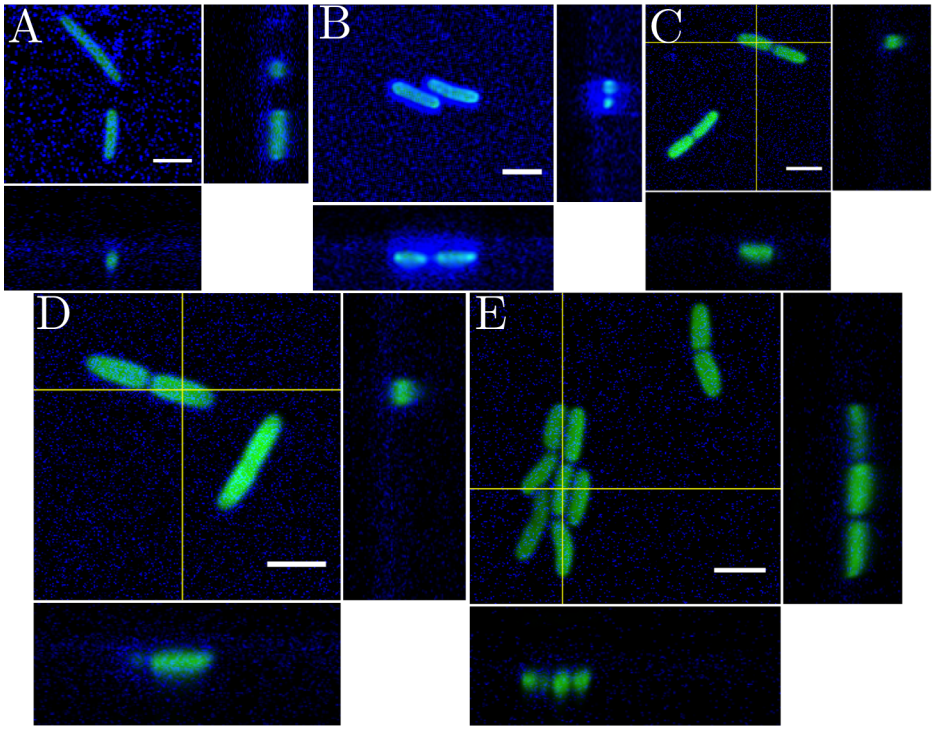

Figure 5.8: Two colour fluorescence confocal images of bacteria (green) on M9 agarose (blue) with (A) 1 %, (B) 2 %, (C) 3 %, (D) 4 % and (E) 5 % (weight) concentration. The sample has been sealed with a coverslip using the method described previously. Across all concentrations the bacteria are seen completely confined to a 2D layer by the coverslip. Scale bar is 2.0 µm. Orthogonal slices are taken every 0.05 µm through the sample.

doped agarose surface. Consequently it can be inferred that the coverslip is flush to both the agarose pad and the bacterium. This means that the bacterium is compressed into the agarose from the position seen in Figure 5.4 (p. 60).

When viewing the bacteria visible in Figure 5.7 in the axial direction there appears to be a thin layer of agarose above each of the bacteria. This is not in fact agarose but rather an accumulation of Rho. B at the surface of the bacterium and at the coverslip interface, similar to the accumulation of Rho. B at the air/agarose interface (Figure 5.4, p. 60) [124]. These results are confirmed when replacing Rho. B with Nile Blue (Figure 5.8) which shows the bacteria fully submerged in the agarose and confined by the coverslip as the concentration of agarose is increased from 1 % to 5 % (weight) agarose concentrations.

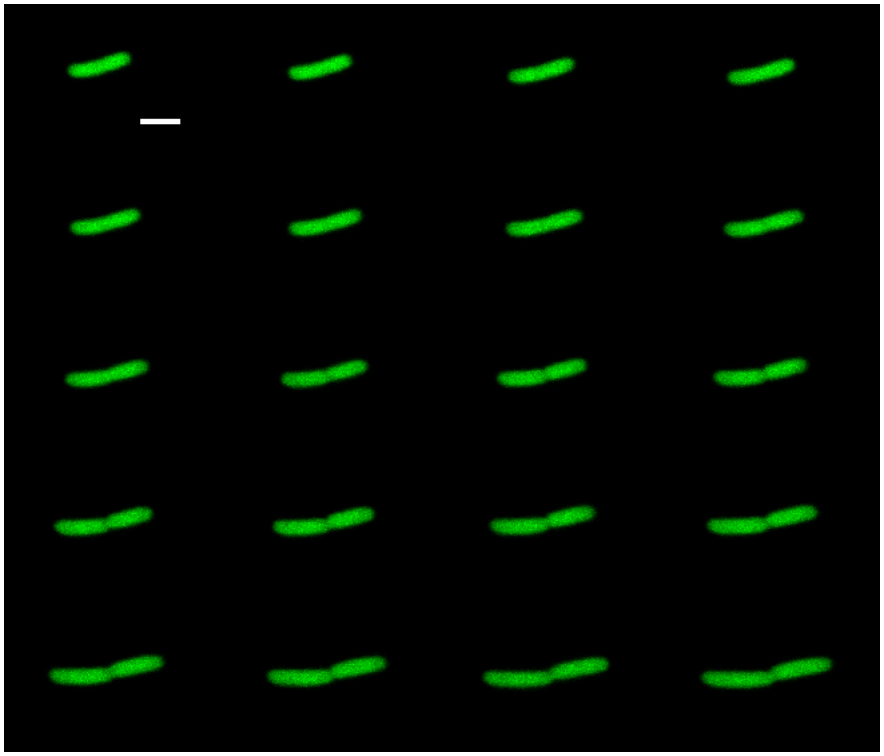

Figure 5.9: The growth of a single bacterium on M9 agarose at 3 % (weight) concentration. Stacks through the sample are acquired every 2 min. The bacterium is seen to approximately double in size from initial conditions until the point where the division occurs. Scale bar is 2.0 µm. A movie of this figure is available as Supplementary Movie A.8.

5.4 The first generation

Confining bacteria in this way limits their initial growth to a 2D plane parallel, and just below, the coverslip. This provides a suitable environment in which to visualise the development of the seed bacterium into a microcolony. Using confocal microscopy, bacteria on the agarose surface were imaged at time intervals of 2 min to 5 min. From the subsequent stacks information is extracted on the position, orientation and size of the bacteria as a function of time allowing quantitative analysis of growth of individual bacteria as the properties of the agarose surface are varied.

5.4.1 A single bacterium growing on an agarose surface

An *E. coli* bacterium in the closed configuration described in §5.3.2 (p. 65) grows in an approximately linear direction from both poles. Whether the growth rate of an individual bacterium is linear, exponential or some other nonlinear form is a current unanswered research question. Laser scanning confocal microscopy allows many of the physical properties of the bacterium to be determined at a superior resolution to

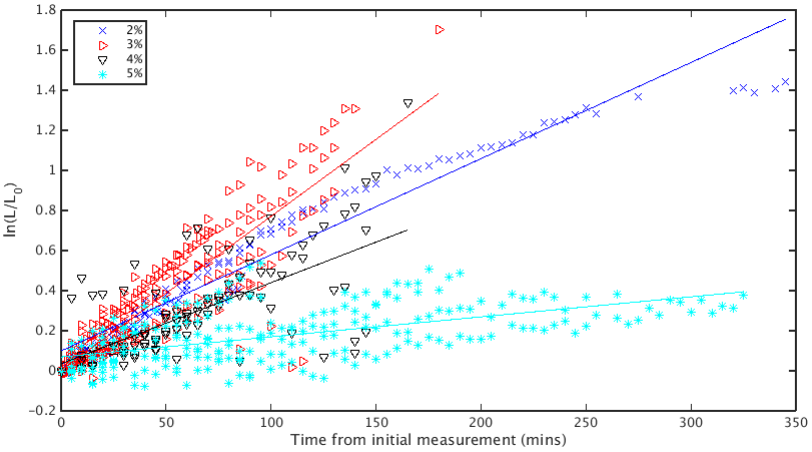

Figure 5.10: Growth of a seed bacterium as a function of time. Measurements of the length of the bacterium are made for each frame and normalised against their initial length (L_0). For all concentrations of agarose in the surrounding media the bacterium increases in length. However, the growth rate varies with the concentration of agarose present in the surrounding media. Exponential fits for the growth rate of 2 % (10), 3 % (21), 4 % (11) and 5 % (16) concentrations of agarose are $0.005\pm0.001\,\mathrm{min}^{-1}$, $0.008\pm0.002\,\mathrm{min}^{-1}$, $0.004\pm0.002\,\mathrm{min}^{-1}$ and $0.0001\pm0.0010\,\mathrm{min}^{-1}$ respectively. Brackets indicate number of bacteria (N) over which measurements are made.

conventional microscopy methods such as phase-contrast or brightfield. Consequently, we can accurately test the growth rate of individual bacteria grown on agarose surfaces.

Figure 5.9 shows a time-lapse reconstruction of the growth rate of a single bacterium from initial imaging to the point of division on 3 % (weight) M9 agarose, with stacks through the sample being acquired every 2 min. The difference in length between frames is clear enough to be readily measured, after analysis by Besseling's code [111], and subsequently imaging bacteria growing from initial state to first division for different concentrations of agarose allows a comparison of growth of a single bacterium as the surrounding conditions are controlled.

5.4.2 Rate of growth

Figure 5.10 shows the normalised growth of the single bacterium for concentrations of agarose of 2 %, 3 %, 4 % and 5 % in an M9 growth media. Measurements of the length of the bacterium (L) for each frame are obtained from Besseling's code [111] and normalised against the initial length (L_0) of the bacterium from the measurements. For all data sets, the bacterium is seen to increase in length from the initial measurement up to the point of division, however, the growth rate of the bacterium is dependent

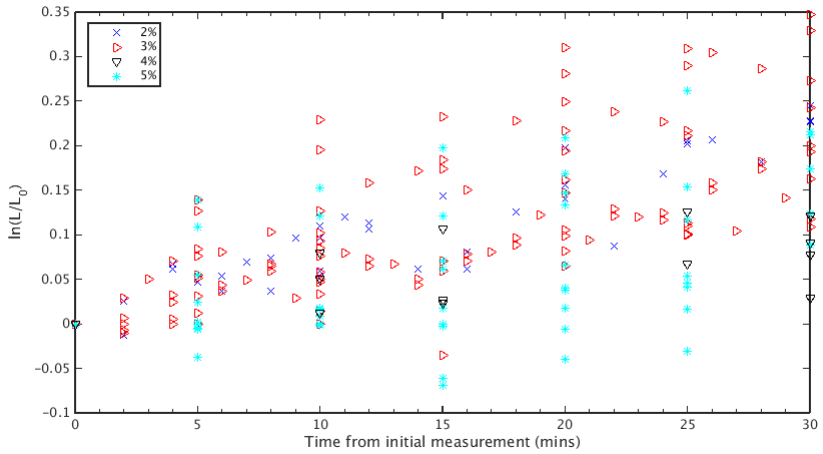

Figure 5.11: Growth of a single bacterium for the first 30 min after commencing imaging on different agarose concentrations. No discernible difference in the growth rate is evident when the agarose concentration within the surrounding media is varied from 2 % to 5 %. N=10 (2 %, 21 (3 %, 11 (4 %) and 16 (5 %).

Agarose concentration (%)	Rate of growth, α (unitlength/min)
2.0	0.005 ± 0.001
3.0	0.008 ± 0.002
4.0	0.004 ± 0.002
5.0	0.0001 ± 0.001

Table 5.1: Rate of growth per minute of bacterium as agarose concentration is varied.

upon the concentration of the agarose within the surrounding media. This appears contrary to previous studies by Tuson *et al.*, which have found that for the first 30 min of growth of a bacterium on the surface of the agarose there is no variation in the growth rate as the concentration of agarose is changed [127]. If only considering the initial 30 min of growth, the experiments do agree as no discernible difference in the growth of the bacterium across the four agarose concentrations investigated here is evident (Figure 5.11).

After normalising L with L_0 it is possible to fit an exponential function of the form

$$\frac{L}{L_0} = e^{\alpha t} \tag{5.8}$$

where α is the rate of growth of the bacterium as a function of time t. The rate of growth (solid lines Figure 5.10) obtained by performing fits on the different agarose concentrations are summarised in Table 5.1 and shown in Figure 5.12. The growth

rate of a bacterium on any agarose surface is greatly reduced when compared to liquid culture. All the growth rates in Table 5.1 are far longer than for liquid cultures. For instance the growth rate for 3 % equates to a doubling time of 90 min compared to 20 min for *E. coli* in liquid cultures at optimal growth conditions. Additionally, the growth rate of the bacterium does not vary linearly with the concentration of agarose in the surrounding media. Rather, there is a peak where the growth is maximum as the agarose concentration is increased from 2 % through 3 % to 4 %, with the maximum being close to 3 %. Although initially surprising, this non-monotonic variation in growth rate as agarose concentration increases matches well with previous experiments investigating the dynamic effects of concentration of agarose on the structure and shape of bacterial colonies [46–48]. Both Su *et al.* [47] and Grant *et al.* [48] see a peak in the size of the colony grown on agarose before the generation of a second layer around this point and this phenomenon will be discussed further in Chapter 6 (p. 75) where the studies are directly relevant.

Beyond the peak at 3 %, the rate of growth decreases with increasing agarose concentration, becoming unmeasurable above 5 %. This marked reduction in growth rate of the bacterium suggests that the force exerted on the bacterium by the agarose is approaching the maximum force which a bacterium can exert in order to add additional matter to the cell wall and therefore grow. Rod-shaped bacteria (such as *E. coli*) grow from both poles by inserting new rings of peptidoglycan (a polymer consisting primarily of sugars and amino acids) into the cell wall randomly along the long axis of the bacterium. In order to do so, the new peptidoglycan must apply a force to separate existing peptidoglycan currently in the cell wall. If the force exerted externally by the surrounding media is greater than the force which the new peptidoglycan can exert in order to insert itself, then the growth of the bacterium will stall and it will remain at a constant length.

The growth rate of a bacterium in 5 % agarose is measured as $0.0001 \pm 0.0010\,\mathrm{min}^{-1}$. This rate of about 0.01 % increase of unit length per minute is exceptionally slow, particularly compared to growth rates at other concentrations (Figure 5.12) and is not attributable to depletion of nutrients at the growth site of the bacterium for two reasons. Firstly, the bacterium is surrounded by nutrients in the form of the M9 agarose with glucose in which it is embedded and secondly, the diffusion rate of glucose through agar surfaces has been measured for several concentrations of agar weight to volume and at temperatures from 18 °C to 37 °C. These diffusion rates are of the order of hundreds of square microns per second, considerably faster than any rate of growth observed of the bacteria at any of the concentrations of agarose [128]. For these reasons we can safely

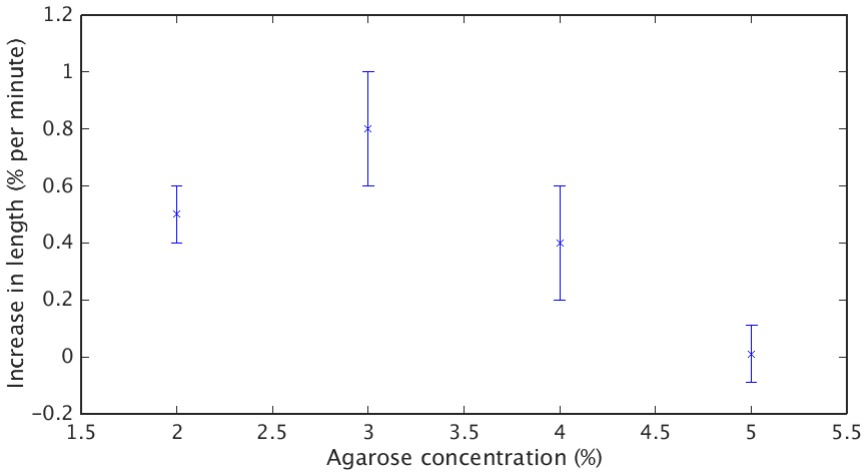

Figure 5.12: Rate of growth per minute of bacterium as the agarose concentration is varied from 2 % to 5 %. The change in growth rate is not linear as the agarose concentration is increased, but rather there is a peak in growth rate at agarose concentrations of 3 %, which matches well with a peak in colony area before buckling seen in Chapter 6 and by experiments conducted by Su, Grant and Lloyd respectively [46–48, 91]. The growth rate is also seen to reduce dramatically at agarose concentrations of 5 %, suggesting the force exerted on the bacterium by the agarose is approaching the internal growth force of the bacterium. Errors are standard errors on the fit.

assume that the slow growth observed is not attributable to any depletion of nutrients and can infer that the growth is slowed by the force exerted externally on the bacteria approaching the internal force of insertion of a protein into the membrane.

Atomic force microscopy

Identification of the slow growth rate of bacteria in 5 % agarose allows us to qualitatively say the external force exerted on the bacterium is of the same order of magnitude as the growth force of the bacterium, but in order to quantify this the force exerted on the bacterium by the agarose, (i.e. the elastic properties of the agarose), must be measured. Literature values of the elastic modulus of agarose gels vary dramatically[2] and are heavily dependent upon the measurement process and geometry at which they are conducted [129, 130]. In order to gain a suitable value for our particular geometry and set-up, it is necessary to perform our own calculations for deformation of agarose gels at the micron scale (the spherical cap of the bacterium through which the growth force of the bacterium is directed is of the order of 1 µm).

One method of achieving this is through atomic force microscopy (AFM). Measurements

[2]Ranging from a few kPa to hundreds of MPa. Literature values relevant to this thesis are summarised in Appendix D

of the elastic modulus of M9 agarose gels have been performed using an AFM pyramid tip of 20 nm in collaboration with a group in the School of Engineering at The University of Edinburgh. The resulting Young's moduli extracted from the curves obtained are high (5.7±1.2 MPa for 5 % M9 agarose gels) compared to literature and vary considerably across a single sample depending on the location of the tip. It is believed the large values and the wide distribution can be attributed to the small diameter of the AFM probe tip meaning measurements are probing individual fibres (or fibre bundles) of agarose on the surface of the sample. This will be verified if measurements are made using spherical beads of 1 µm diameter attached to the cantilever providing the force, allowing measurements to be made with a geometrically similar setup to a bacterium extending its length by pushing a hemispherical cap into the agarose.

5.5 Future developments

The resolution of confocal microscopy has proved to be great enough to image single bacteria through a coverslip over prolonged periods of time, however, the addition of the coverslip to the system does add additional constraints to the bacterium which can be difficult to quantify in terms of the forces exerted between the glass coverslip and the bacterium. Additionally, it has been shown in these experiments that the starting position of the bacterium has been altered by addition of the coverslip to the system.

In this chapter I have shown it is possible to image a single bacterium on an agarose surface by imaging through the agarose, rather than by adding a coverslip and inverting the sample. Further development of this method would be particularly interesting as it more closely resembles conditions seen *in-vivo* for bacteria growing on the surface of food [131], in the human body [132,133] and other surfaces exposed to air [5,40,134,135]. To achieve this, a custom-built flow-chamber capable of housing a small layer of agarose with the bacteria cultures would allow imaging through the agarose and the ability to pass growth media over the top of the bacterial cultures, without compromising the image integrity. Temperature regulation of the chamber would also allow precise reconstruction of *in-vivo* conditions.

5.6 Conclusions

Through imaging of individual bacteria present on M9 agarose using confocal microscopy I have shown in this chapter that when exposed to the air (i.e. not sealed by a coverslip), open bacterial cultures do not rest on the surface of the agarose but are partially submerged in it. Initially the amount of the bacterium submerged in the

agarose increases as a function of time, due to the evaporation of the fluid within which the bacteria culture is introduced to the agarose, but this stabilises after a period of approximately 10 min whereupon approximately a quarter of the bacterium is above the surface of the agarose with the rest submerged in the bulk. This stabilisation correlates well with the time required for the PBS to evaporate entirely from the surface of the agarose. Additionally, it is shown that bacteria grown on an agarose pad which has been sealed by a coverslip are fully submerged in the agarose with the top surface of the membrane of the bacterium being in-line with the surface of the agarose, effectively confining the bacteria to a 2D layer along the surface of the coverslip.

Variation of the concentration of agarose surrounding the bacterium affects the growth, with a peak in the rate of growth at weight concentrations of 3 % agarose. It is highly probable that this peak is linked to the increase in colony buckling areas seen in previous studies by Su *et al.* [47] and Grant *et al.* [48] and also seen in further experiments conducted as part of this thesis (Chapter 6, p. 75). Additionally, the growth rate of the bacterium is seen to slow dramatically (by almost a factor of 100) as the agarose concentration is increased from 3 % to 5 %, 0.00770 ± 0.0003 and 0.00010 ± 0.00005 unit length per minute respectively. The increase in length of only 0.01 % per minute at 5 % agarose concentrations equates to a doubling time far longer than that of the bacterium in bulk, suggesting the pressure exerted by the agarose surrounding the bacterium is approaching the force required to insert a new ring of protein into the bacterial cell wall.

By investigating the elastic properties of M9 agarose gels using AFM the Young's modulus of 5 % agarose gels has been measured at 5.7 ± 1.2 MPa, which is at the upper limit of literature values (Appendix D, p. 143). However, literature measurements of the agarose stiffness properties are highly dependent upon the method employed and the geometry used and repetition of these measurements with an AFM probe of similar geometry to the hemispherical cap of the bacterium (i.e. a spherical bead of approximate diameter 800 nm) would provide a more relevant comparison.

Chapter 6

The first division and beyond

6.1 Introduction and previous work

Once a bacterium on an agarose surface has grown and divided, (Chapter 5), the daughter bacteria (produced upon the division of the seed bacterium into two new bacteria) will grow on the agarose surface and divide.[1] As this process repeats and the colony grows from two daughter bacteria to four, the bacterial colony will expand in a 2D layer along the surface of the agarose (Figure 6.1), initially forming a two-by-two cell matrix (as seen by Su *et al.* [46]) where the daughter bacteria grow preferentially from the new poles and therefore appear to slide alongside each other parallel to their respective long axis. After the second division of the bacteria on the plate (giving four bacteria in the colony), the process of growth and division will continue to iterate and the colony will expand. For early generation growth, up to approximately the seventh generation (six divisions) of bacteria, Stewart *et al.* showed that the division of all bacteria in the colony is relatively synchronised, meaning two daughter bacteria will grow for a similar period of time after they have been created from the same parent bacterium, before dividing at approximately the same time (with the bacterium produced from the newer pole always dividing first) [50]. This division will continue to occur and the bacteria in the colony will replicate into a disc shaped colony.

At early generations, space is available for the growth and division of bacteria on the agarose surface. However, as the local area fraction at the centre of the colony tends to 1 there is no longer sufficient space for bacteria to grow, and as a result one of three processes must occur:

[1] As discussed in Chapter 5 the bacteria are not entirely on the surface of the agarose but are rather immersed in the agarose and flush to the coverslip. For the purposes of this chapter when referring to 'on the surface' of the agarose it is meant that the bacteria are confined in this way.

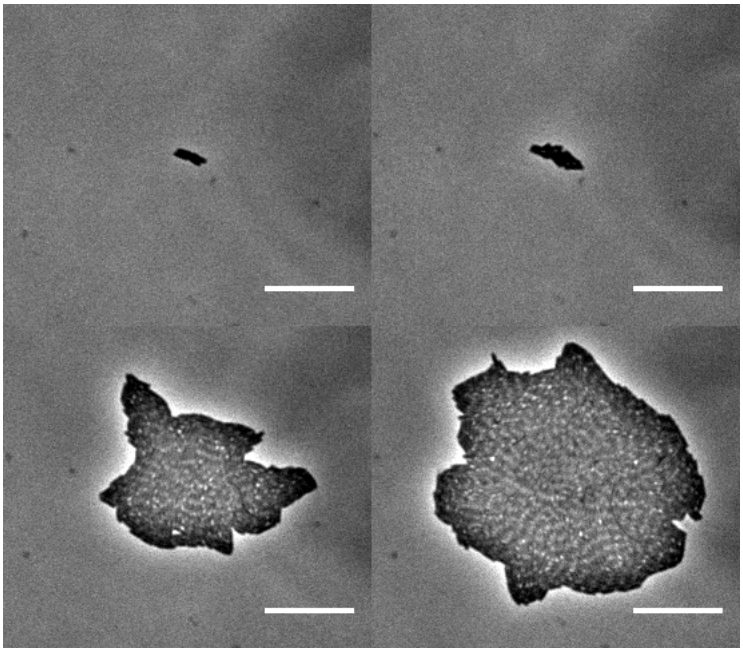

Figure 6.1: Stills from a phase-contrast video of a bacterial colony growing in two dimensions on 3 % (weight) M9 agarose at 37 °C. The colony expands in a plane. Scale bar is 25 µm. Reproduced from [91]

1. The central bacteria stop growing and dividing, becoming dormant or die.
2. The bacteria push away neighbouring cells to provide space for themselves to grow and divide
3. The bacteria find additional space in the third dimension.

Studies by Lloyd *et al.* ruled out the first process [91]. The confined bacteria are not limited by nutrient uptake, since the nutrient is evenly dispersed beneath the bacteria in the agarose [128] so that bacteria in the centre of the colony will continue to grow and divide along with those on the edge of the colony. As is clear from Figure 6.1 (top right panel), initially the colony grows in a 2D plane on the surface of the agarose, despite the central bacteria being confined on all four sides. However, after a period of time, growth is not restricted to this plane, rather bacteria, in approximately the centre of the colony, invade into the underlying agarose in order to find additional space to grow and divide [47].[2]

This invasion, known as a buckling event, has been further studied by Grant *et al.* [48], who found that varying the agarose concentration from 1.5 % to 4 % produces different

[2]In the absence of a coverslip the confined bacteria will preferentially invade into the air above the agarose.

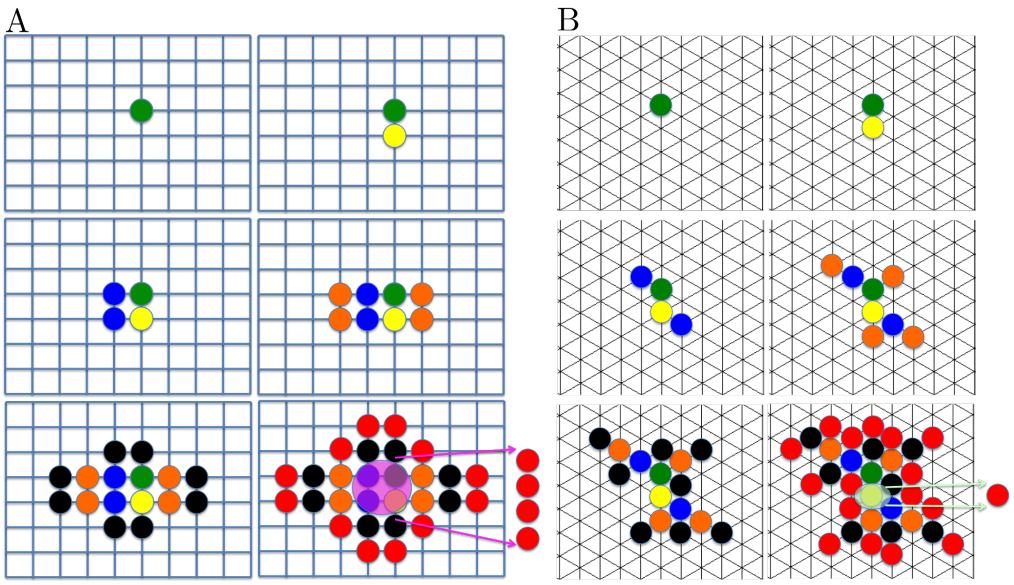

Figure 6.2: Colony growth on a square (A) and triangular (B) lattice. A spherical seed bacterium (green) divides and places a daughter (yellow) onto an adjacent point on the lattice. This process can iterate through a third (blue), fourth (orange) and fifth (black) generation before the central bacteria are completely confined and unable to place their daughter bacteria onto an adjacent point on the square lattice (red). Thus the central bacteria must push adjacent bacteria away or find new space (the third dimension) in which to place their daughter bacteria.

sized colonies before the buckling event occurs. They observed an increase in the critical buckling area, A_c, as the agarose concentration is increased from 1.5 % to 3 %. However, as the concentration is increased beyond 3 % to 4 %, A_c reduces. Grant *et al.* propose a model involving static frictional forces, which describes this non-monotonic trend, and points to the importance of considering mechanical interactions when investigating bacterial colonies growing on agarose [48]. This has been further verified by Lloyd, who reproduces this nonlinear dependence of buckling colony size to agarose concentration under slower growth conditions (doubling time $\approx$ 60 min) as well as at the original growth conditions (doubling time $\approx$ 20 min) [91].

6.1.1 'Game of Life' and buckling

The physical reason for buckling into the third dimension can be made clear by a 'game of life' [136] on a 2D lattice, (Figure 6.2A), in which 'cells' are denoted by occupied lattice sites, and each cell is allowed to 'reproduce' by making a 'daughter cell' on any nearest-neighbour lattice site.[3] We start with an initial 'cell' (= occupied lattice site). It is clear that on a square lattice, the central cells no longer have empty sites in which

[3]Using a lattice to describe this concept was originally proposed by Alexander Morozov, with Wilson Poon noticing the similarity to Conway's famous game.

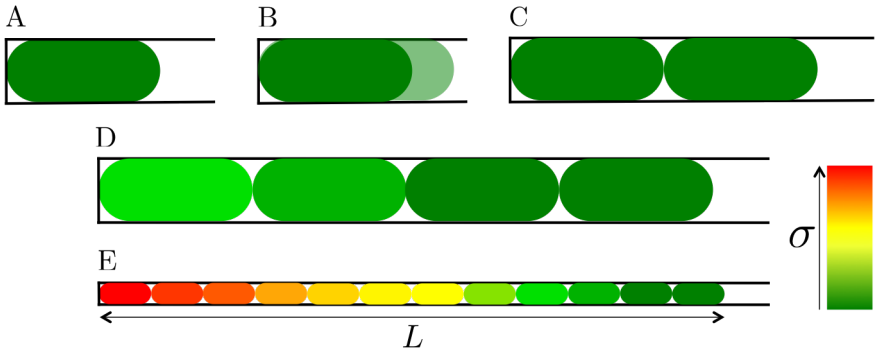

Figure 6.3: A one-dimensional array of rod-shaped bacteria grown in a rigid, incompressible tube open at one end and with diameter equal to the diameter of the bacteria. [A] The seed bacterium is placed flush to the incompressible wall where it begins to grow along a single axis [B]. [C] The bacterium divides producing another bacterium before continuing to grow, pushing the daughter bacterium away as it does so. [D] As the system iterates, the growing seed bacterium is forced to push more bacteria away from it in order to generate enough space into which it is able to grow and divide. As this occurs, the seed bacterium is under increasing stress (σ) from external sources. [E] At a point this stress increase will be greater than the force that the bacterium can exert through growth. At critical σ (red) the seed bacterium will be unable to grow any further in this direction, resulting in termination of the growth in the one-dimensional array.

to reproduce after $n = 5$ divisions. The value of n depends weakly on the symmetry of the lattice, Figure 6.2B, but is always ~ 5 in 2D. This is the fundamental reason for a 2D colony to invade into the third dimension, although in reality, the size of the colony at which this will happen must depend on a host of other factors such as cell shape, cell-cell interaction, and cell-substrate interaction.

6.1.2 Pressure build up and buckling

The 'game of life' model does not allow for cells pushing each other out of the way to create 'growth space'. Our *E. coli* cells clearly can do that, so that buckling can occur later than ~ 5 generations. Such pushing, together with friction between cells and the substrate, creates an increasing pressure towards the centre of the colony. This can be seen in a 1D toy model, Figure 6.3, where a single bacterium is placed adjacent to the wall of a tube diameter 0.8 µm (i.e. identical to the diameter of the bacterium) (A). The tube consists of incompressible walls on three sides, but allows sufficient nutrient for optimal growth. Growth and division of the bacterium (B-C) confines the seed bacterium, producing an identical effect to that seen at the centre of a bacterial chain where central bacteria are confined by adjacent cells. Iteration of the process results in an increase in the force required to displace adjacent bacteria, causing a rise in the external stress, σ, exerted on the bacterium by adjacent cells (D). After a finite number of iterations σ will equate to the growth force of the seed bacterium and the

seed bacterium will reach a critical stress σ_c (red) and be unable to grow (E). For simplicity of depicting this process schematically, the growth of daughter bacteria has been neglected, however, the rate at which σ_c is reached is increased if all bacteria continue to grow upon division. This setup has been experimentally realised by Moffitt *et al.* who created ridged agarose pads encouraging bacteria to grow in single chains rather than 2D colonies while allowing small molecule nutrients to reach all bacteria in the chain [137].

It is easy to calculate the effect of pressure on this model by assuming an overdamped system (i.e. one where friction is more important than viscosity) and that the friction is proportional to the velocity (v) of the bacteria (Stokesian friction).[4] The pressure gradient $\frac{dp}{dx}$ in one dimension is therefore

$$-\frac{dp}{dx} = \gamma v \tag{6.1}$$

where γ is the damping term.

If we assume the bacteria in Figure 6.3 are all growing at the same rate ($\frac{dv}{dx} = \Lambda$), Eq. 6.1 becomes

$$\frac{d^2p}{dx^2} = \gamma\Lambda \tag{6.2}$$

which has a quadratic solution

$$p = p_0 + 0.5\gamma\Lambda(L^2 - x^2) \tag{6.3}$$

where p_0 is the pressure exerted on the system by the surrounding agarose and L is the length of the chain (Figure 6.3E). Therefore the pressure increases quadratically to the centre of the chain (or the wall in Figure 6.3).

Eq. 6.3 assumes Λ is uniform across this chain. This is not a realistic assumption, rather Λ is a function of pressure with a maximum pressure ($p_{\max}$) at which growth can occur. Thus

$$\Lambda(p) = \Lambda_0\left(1 - \frac{p}{p_{\max}}\right) \tag{6.4}$$

meaning solutions to Eq. 6.2 take the form of cosh functions with a maximum pressure $p_{\max}$ rather than quadratics. While this model only considers a 1D chain of bacteria, the argument is scalable to two-dimensions with L being the radius of the colony.

[4] The calculation for the pressure across the colony was originally performed by Matthew Blow

6.1.3 Single bacterial resolution

The previous studies mentioned above by Su, Grant and Lloyd [47, 48, 91] all focus primarily on colony scale interactions, investigating parameters such as the critical buckling area, difference in colony area between initial and buckled layer and rate of colony area expansion as a function of time. While some investigations are conducted by both Grant *et al.* [48] and Lloyd [91] on a single bacterial level, neither pursues this to its logical conclusion, the production of a 3D micrograph of a bacterial colony as a function of time. This can partly be attributed to the difficulty of obtaining high enough resolution in 3D to successfully resolve individual bacteria in such a densely packed system.

The study of microcolony and biofilm formation is more comprehensively addressed in the literature, with numerous studies looking at the mechanisms and structure that these systems take on [5, 40, 41, 44, 45]. But these studies tend to focus on the overall structure of the biofilm, locating and distinguishing between the different constituent parts of biofilms, the bacteria cells and other structures within the extra-cellular matrix [49]. The location of individual cells within the biofilm, and 3D colonies in general, has yet to be studied in detail. Locating and tracking all individual bacteria in the colony should offer increased understanding of how and why colonies form as they do. However, in order to do so it is necessary for 3D stacks of images to be produced at a single-bacterial resolution in order to allow distinction between individual cells in the microcolony, particularly as the volume fraction of the colony tends to 1 and additional layers (above the initially formed layer) are created. Chapter 4 shows single bacterial resolution is achievable and the remainder of this Chapter presents results of single bacterial resolution experiments using these methods.

6.2 The first division

Resolving single bacteria in a confined 2D plane, (Figure 6.4), is relatively trivial to achieve. Brightfield microscopy techniques are capable of distinguishing individual bacteria in a two-dimensional plane provided the magnification of the objective lens is high enough, ($> 40\times$). Phase-contrast further enhances the ability to resolve individual bacteria in this way by providing enhanced distinction between the edges of the bacteria, so that confocal microscopy could be considered excessive for such simple structures. However, confocal imaging is vital for studying the third dimension, and the third dimension is vital to all higher organisms we know of today. This is clear from the basic topology of all metazoans (higher animals), which is that of a doughnut: the

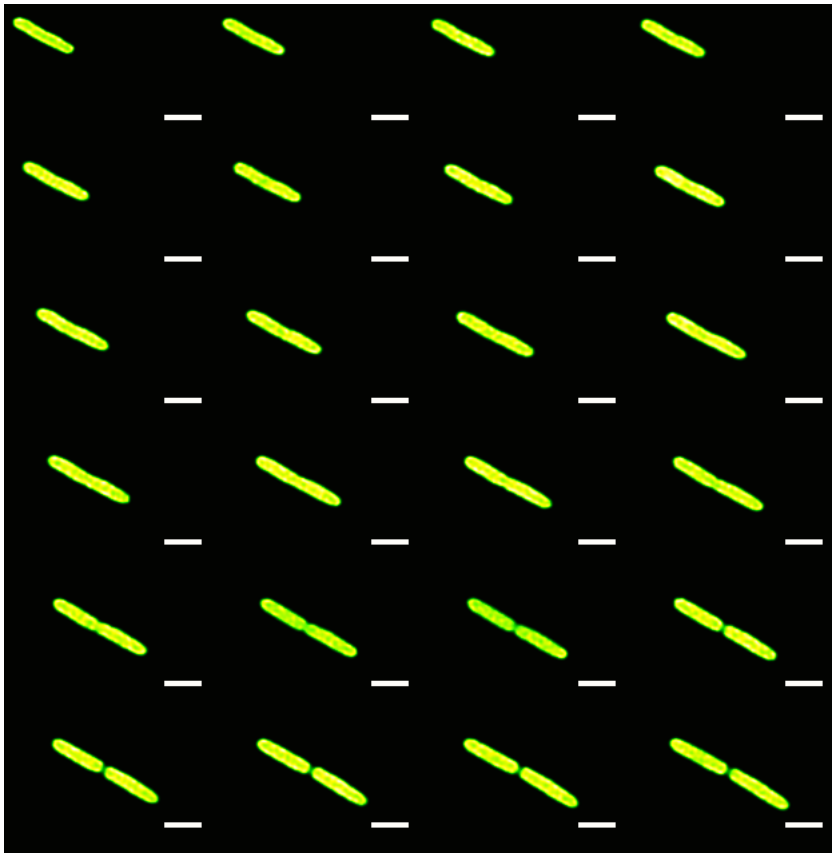

Figure 6.4: Bacterial colony growth from seed bacterium to first division (generation 2) on 2 % M9 agarose gel. Stacks of images are recorded every 5 min. The bacterium grows in the long axis in a two-dimensional plane along the surface of the agarose before dividing to produce two daughter bacteria. Scale bar is 2 µm. A movie of this figure is included as Supplementary Movie A.9 (p. 135).

'hole' in the middle is the alimentary track (mouth to anus). A 2D body plan of this kind, Figure 6.5, does not work – a 2D metazoan simply falls apart. The 'discovery of the third dimension' by a growing 2D bacterial colony was therefore a vital step in evolution. On a more mundane level, such buckling of a 2D microcolony is a key step in the life cycle of a 3D biofilm. Yet, this buckling event has been little studied in the literature.

Obtaining 3D images is vital for such study, since projecting bacterial microcolonies grown on agarose to a 2D plane, Figure 6.4, results in the loss of a third of the spatial and orientational information. This is highlighted in Figure 6.6, showing a colony grown on 2 % M9 agarose media. Even when only containing as few as 16 bacteria, one of the central, spatially confined, bacteria (red arrow) loses fluorescence in the imaging plane. If only considering a 2D bacterial system it may be inferred that this reduction

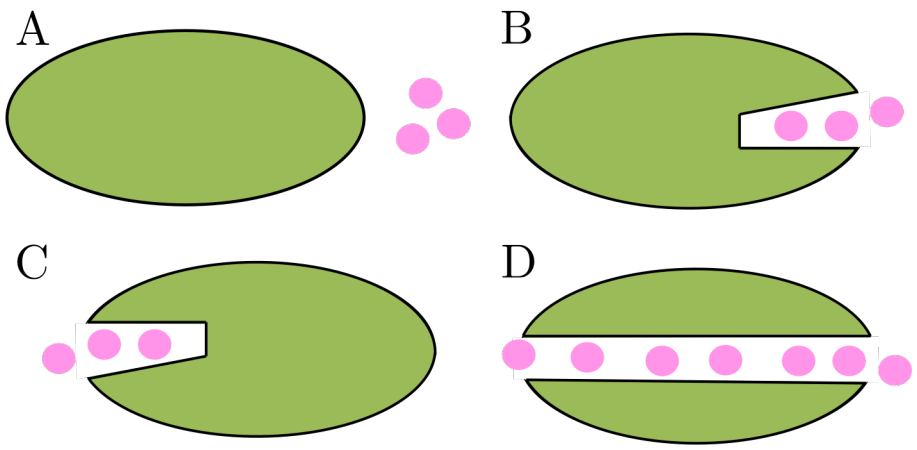

Figure 6.5: Cartoon of 2D organism. A: A 2D organism. B: Intake of nutrients requires a separation in the organism. C: Excretion of waste also requires a separation of the organism. D: Simultaneous nutrient uptake and waste excretion requires the organism to divide into two.

in fluorescence is the result of photobleaching, or the reduction in the copy number of the plasmid containing the fluorescent protein as the bacterium grows, suggesting the bacterium remains in the initial growth plane but with a loss of signal. However, comparing this to the 3D stack of the same colony (right panel of Figure 6.7), the bacteria can clearly be seen bending away from the 2D growth plane and beginning to force its way into the third dimension.

By sectioning samples (Figure 6.7) in this way, 3D information is not lost. In Figure 6.7, the 3D structure of the bottom two panels of Figure 6.6 shows both the fourth and fifth generations of the bacterial colony are still growing in a single 2D plane but, in generation 5 (right) there is clear evidence of a single central bacteria invading the agarose and deviating from this plane (red arrow). In fact, this is already occurring in generation 4 (left), with the bacterium being slightly raised relative to the rest of the bacteria in the colony when viewed in the orthogonal plane (blue arrow), despite the 2D slice along the surface of the agarose showing no indication of invasion.

6.2.1 Three-dimensional orientation

To a first approximation, a bacterium on the surface of an agarose pad will initially grow in a linear fashion, however, at the division (septation) the *E. coli* are seen to 'kick' away from each other, by some unknown process, as they divide, in order to allow growth to occur at the newly formed poles (a process first described by Begg and Donachie [112]). This event has been imaged in the xy plane using a plethora of imaging techniques, and is visible in Figure 6.6, where the bacteria push past each

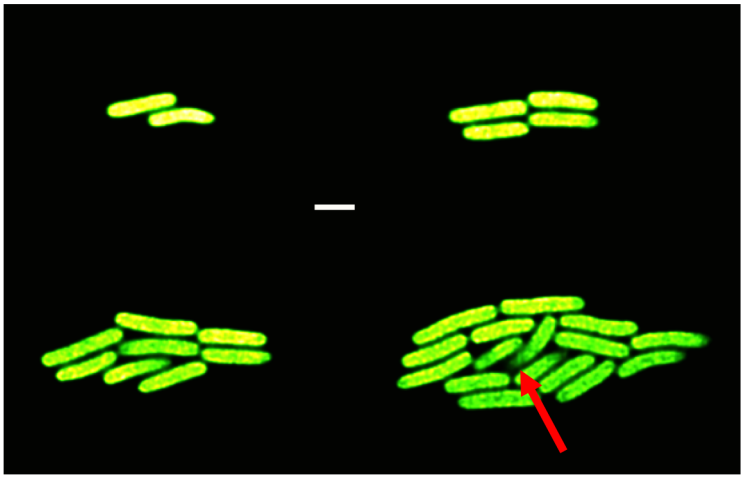

Figure 6.6: Development of a bacterial colony from two-dimensional growth on the surface of 2 % M9 agarose gel to three-dimensional growth. The bacteria grow and divide in a single plane at the surface of the colony. However, in the final panel shown here (bottom right) a central, spatially confined, bacterium in the colony is seen to bend away from the growth plane and appear to be pushed into the third dimension (red arrow). Scale bar is 2 µm.

other from the top left panel to the top right panel to align themselves in parallel and form a two-by-two matrix. While this has only been seen in the 2D plane it is also possible that the 'kick' event will include an out-of-plane component.

Indeed, as the bacteria grows along the long axis of the cell it is likely that it will experience an accumulation of pressure similar to that experienced by compressed beams, forcing the centre of the bacterium to bend and the bacterium to bow in the centre (Figure 6.8, p. 85). An order of magnitude calculation can be performed for the Euler buckling force (F_c) using

$$F_c = \frac{\pi^2 EI}{l^2} \tag{6.5}$$

where l is the length of the bacterium, E, the Young's modulus and I the moment of inertia. Assuming the bacterium is cylindrical, $I = 0.5MR^2$ where M is the mass of the bacterium (1×10^{-12} g) and R the radius of the cylinder (400 nm). Using the estimation of Young's modulus (§ 5.3.1, p. 61), $E = 300$ kPa, we calculate $F_c = 15$ pN, a force far smaller than that necessary to displace agarose through extension of the cap of the bacterium (mN).

Immediately upon division of the seed bacterium into two daughter bacteria, one (or both) of the bacteria must therefore not be parallel to the growth plane of the seed bacterium, invading the agarose (C). As time increases from the septation (division) the bacteria will align themselves parallel to the initial growth plane (due to the proximity

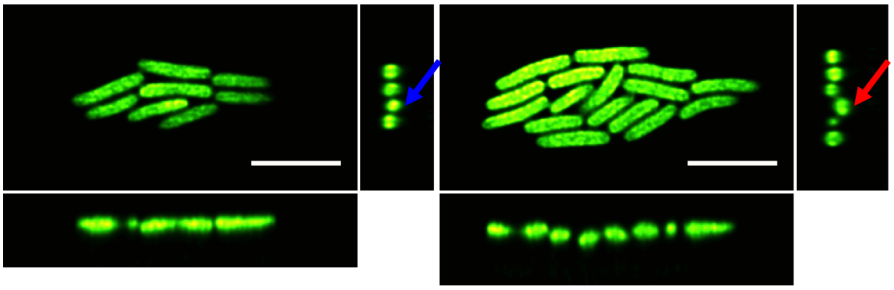

Figure 6.7: 3D images of a bacterial colony grown on 2 % M9 agarose. [Left] Colony having reached generation 4 (3 divisions). The colony is still clearly in a 2D plane but with a single bacterium (blue arrow) deviating from it. However, the overlying trend of the colony is still in a 2D plane.
[Right] Colony having reached generation 5 (4 divisions). The colony is beginning to exhibit 3D structure beyond that intrinsic to the structure of a single bacterium. A central bacterium (red arrow) is seen clearly to be bending into the agarose surface. Scale bar is 5.0 µm.

of the coverslip), where in the xy plane they will grow past each other to eventually form a 2×2 matrix. I now give evidence that this conjectured sequence of events may indeed occur in reality.

6.2.2 Early deviation into the third dimension

Achieving resolution of the colony growth at individual bacterial level allows investigation into local deviations relative to the initial growth plane. Stacks of bacterial colonies grown on M9 agarose were imaged at 5 min intervals from inoculation of the sample to beyond the point of buckling and the weight percent concentration of agarose was varied from 1 % to 5 % (Chapter 5, p. 57). Using code developed by Besseling and Hermes [111] the spatial location and orientation of spherocylindrical rods is fitted to all bacteria. This allows extraction of the angle relative to the growth plane (θ) for the spherocylinders which have been fitted to the bacteria (Figure 6.9, p. 86).

Figure 6.10 (p. 87) shows measurements of the mean angle of all bacteria ($\langle\theta\rangle$) relative to the agarose surface (A), and maximum angle relative to the agarose surface, $\theta_{\max}$, (B) for early growth of bacteria on agarose. Initially a single bacterium is aligned with the agarose surface, before a sharp increase in $\langle\theta\rangle$ as the bacterium divides (arrow). $\langle\theta\rangle$ then decreases rapidly, indicating the bacteria are relaxing to align parallel to the agarose surface after division. After this initial relaxation, $\langle\theta\rangle$ increases steadily to each new division point with sharp rises in $\langle\theta\rangle$ at each subsequent division. Unsurprisingly, these sharp increases in angle relative to the agarose surface are accentuated when analysing $\theta_{\max}$, with dramatic increases across the division points, indicating the 'kick' event occurs in all directions and one bacterium invades the agarose more than the

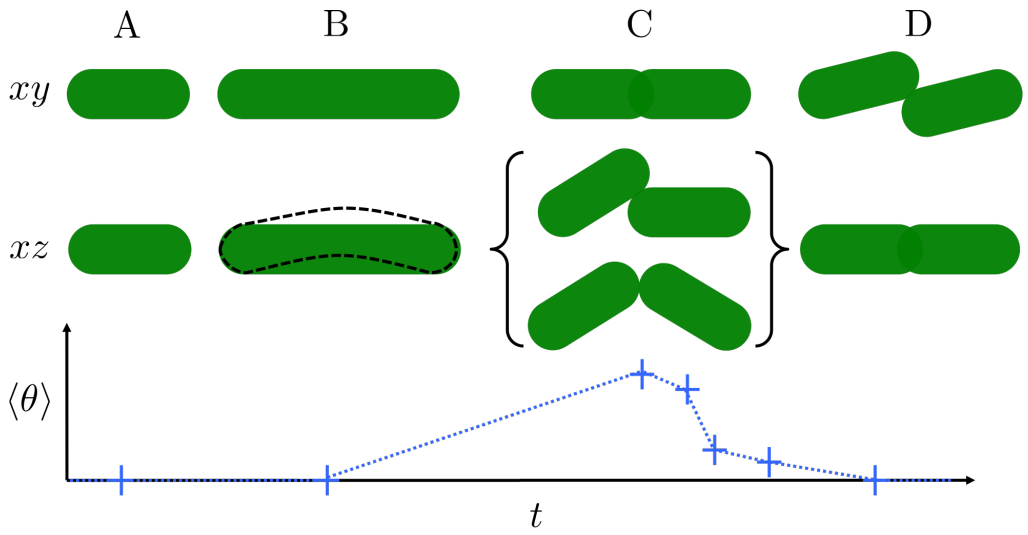

Figure 6.8: Schematic showing the xy and xz projections of a bacterium as it grows from seed (A) to first division. (B) As the bacterium grows it appears spherocylindrical in the xy projection but bows (dotted black line) in the xz view. (C) At the point of division the bacteria still appear to be aligned in the xy view but one (or both) are seen to invade the agarose layer before relaxing (D) to lie parallel to one another. Measurements of the mean angle of the bacteria in the colony relative to the initial growth plane ($\langle\theta\rangle$) indicate the extent which bacteria are being forced into the third dimension.

other (top of bracket in Figure 6.8C). Noticeably, though, the fourth division does not correspond to a sharp increase in $\theta_{\max}$. This is believed to be a result of the close proximity of two divisions masking one another. The data in Figure 6.10 are consistent with the scenario sketched out in Figure 6.8.

6.3 From two to many

After division of the seed bacterium into two daughters, of approximately equal length, the colony continues to grow in a 2D plane (Figure 6.11, p. 88). The daughter bacteria push past each other, providing space at the newly formed caps for growth. As the second generation grows, the bacteria align parallel to each other, most probably in order to reduce surface tension between themselves and the agarose, before dividing again to form a two-by-two matrix as observed by Su *et al.* [46]. However, Figures 6.7 and 6.10 show the initial layer of bacteria is not flat. Moreover, as the number of bacteria in the colony increases, the centre of the colony flexes into the agarose (Figure 6.12, p. 89), with central bacteria deviating from the imaging plane through the bacteria at the extremity of the colony. This flexing can be seen as an increase in θ across the colony.

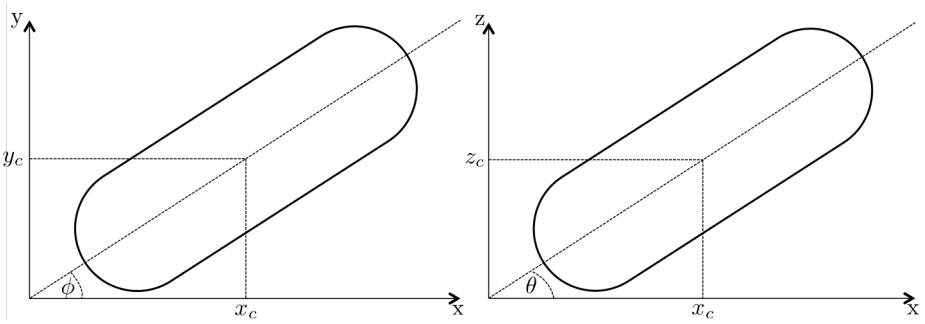

Figure 6.9: Schematic of parameters obtained from reconstruction code developed by Besseling *et al.* [111] [Left] Projection of the bacterium onto the xy plane with the centre of mass coordinates for x (x_c) and y (y_c) shown along with the angle the bacterium makes with the x axis (ϕ). [Right] Projection of the bacterium onto the xz plane with the centre of mass coordinates for x (x_c) and z (z_c) shown along with the angle the bacterium makes with the z axis (θ). The combination of these parameters, alongside the fitted length and diameter of the bacteria allows for full spatial reconstruction of the location of the bacterium.

By measuring the variation of the mean angle relative to the initial growth plane ($\langle\theta\rangle$) this process can be quantified (Figure 6.13, p. 90). While growth and division continues in a 2D plane, Figure 6.6 (p. 83), as is the case for very early bacterial division, I find that before buckling occurs $\langle\theta\rangle$ increases as the number of bacteria increases (B). This means that supposed sudden buckling events into the third dimension are not as sudden as assumed by Su *et al.* [47] and Grant *et al.* [48], especially since measurements of the the maximum angle $\theta_{\max}$ tell us that the buckling transition occurs when $\theta_{\max}$ approaches $\frac{\pi}{2}$, i.e. when cells begin to stand upright (anti-parallel to the growth plane). Indeed, this scenario is consistent with the description given by Grant *et al.* who assume a gradual accumulation of out-of-plane orientation in cells.

The large increase in $\theta_{\max}$ across the division seen in very small colonies (Figure 6.10) is not as defined as the number of bacteria increases, a result of divisions occurring asynchronously to one another. The effect of this could be reduced by tracking of individual bacteria, allowing investigation of the change of angle on a local, rather than global, scale.

6.4 The development of additional layers

Very early in their development, bacterial colonies show evidence of three-dimensionality, however slight, and as the colony continues to expand, previous experiments conducted by Grant *et al.* [48] and Lloyd [91], using phase contrast microscopy, report a darkening of the central region of the colony, indicating an increase in the amount of high

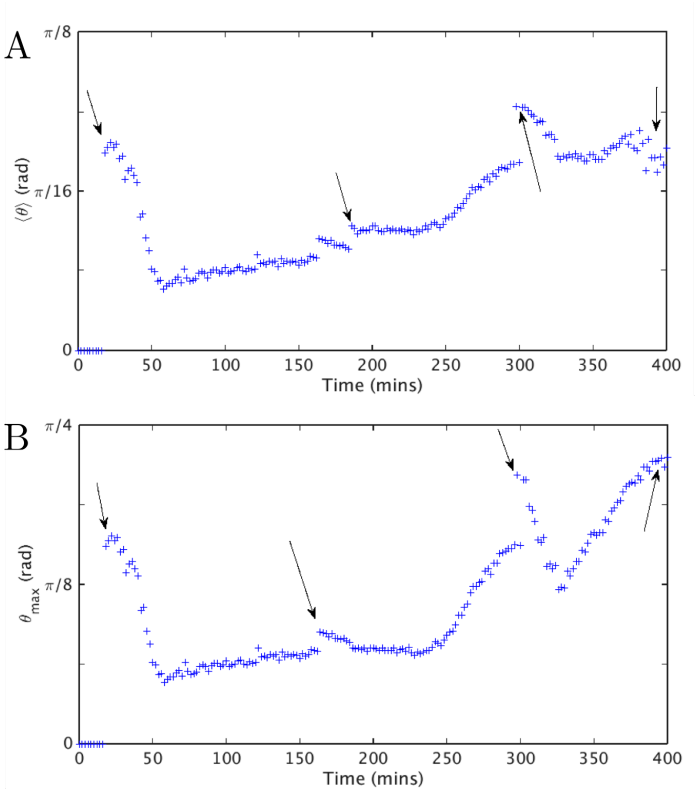

Figure 6.10: [A] Measurements of the mean angle of bacteria relative to the initial growth plane ($\langle\theta\rangle$) as a function of time for initial measurements. Arrows indicate the first time an increase in bacteria is recorded (i.e. the first frame after division). Initially the bacterium is parallel to the surface, but at division (arrow), $\langle\theta\rangle$ increases dramatically. After division $\langle\theta\rangle$ decreases dramatically before steadily rising to the second division, before which a sharp rise is seen. $\langle\theta\rangle$ continues to increase after division before a dramatic rise as the fourth bacteria is created. [B] Measurements of the maximum angle of a bacterium $\theta_{\max}$ relative to the initial growth plane. As with $\langle\theta\rangle$ a sharp increase in $\theta_{\max}$ is seen as the bacterium divides, with the event being clearer in the first three cases. The fourth division is masked partially by the close proximity of two divisions at this point (390 min and 402 min) meaning a relaxation in $\theta_{\max}$ is not observed in this case.

refractive index medium through which the light is passing. This darkening is the development of additional layers of bacteria, caused by central bacteria being unable to displace surrounding bacteria, and therefore buckling into the agarose. However, these studies have been unable to identify individual bacteria in the colony, relying instead on measurements of the colony area.

Figure 6.15 (p. 92) shows a colony grown on 3 % M9 agarose after 18 hrs of imaging. Three layers of bacteria are clearly seen in the colony, the primary layer on the agarose surface and two additional layers caused by invasion of bacteria into the agarose. Individual bacteria are identifiable in the colony allowing extraction of the spatial

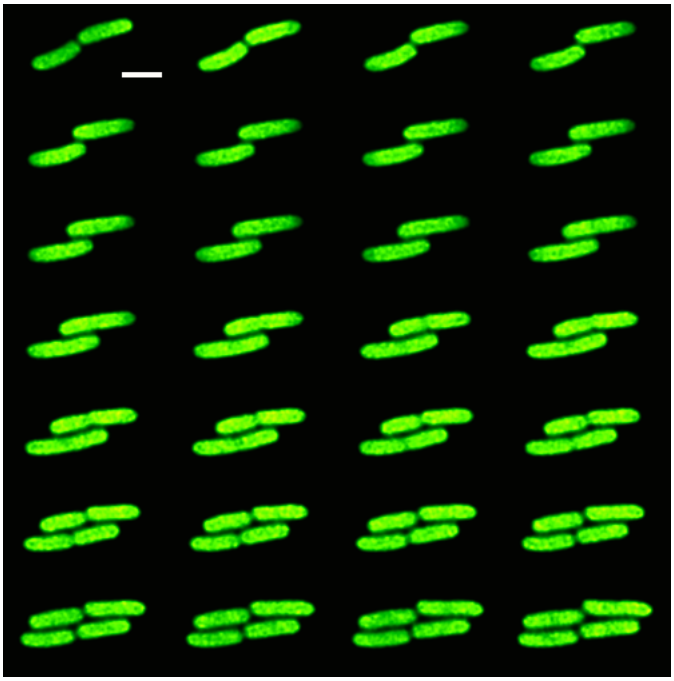

Figure 6.11: Bacterial colony growth from first division (generation 2) to second division (generation 3) on 2 % (weight) M9 agarose. Stacks of images are recorded every 2 min (4 min intervals shown here). The colony is seen to grow in a 2D plane on the surface of the agarose. After the initial generation, the two bacteria are seen to push past each other to allow growth from the newly formed caps in the centre. Similarly, as the third generation forms, the bacteria push past each other to form a two-by-two matrix. Scale bar is 2.0 µm. This montage is a smaller part of the Supplementary Movie A.10 (p. 135).

location, orientation and dimensions of each individual bacterium and investigation of the buckling event at single bacterial resolution. Figure 6.16 (p. 93) shows the number of bacteria ($\mathrm{Num_{bac}}$) in the colony at the point where the centre of mass of a single bacterium is measured to be one diameter (0.8 µm) higher than the centre of mass of the lowest bacterium. This difference between the centre of masses of the highest and lowest bacteria in the colony corresponds to the buckling event. The centre of mass of the lowest bacterium is chosen as the reference point as it is not possible to identify the location of the coverslip without the addition of another fluorophore. Similarly, the relative position of the bacteria in the confocal stack varies considerably across the experiment timeframe (of the order of 24 hrs) due to the movement of the sample relative to the objective (this is unavoidable when wishing to generate single bacterial resolution in 3D stacks due to the need to match the refractive indices of the glass and the objective, Chapter 2, p. 15). It is assumed that the sample chamber, and therefore the bacterial colony, is perpendicular to the imaging setup (to a first approximation), and therefore that there is little variation in the axial position of the agarose surface

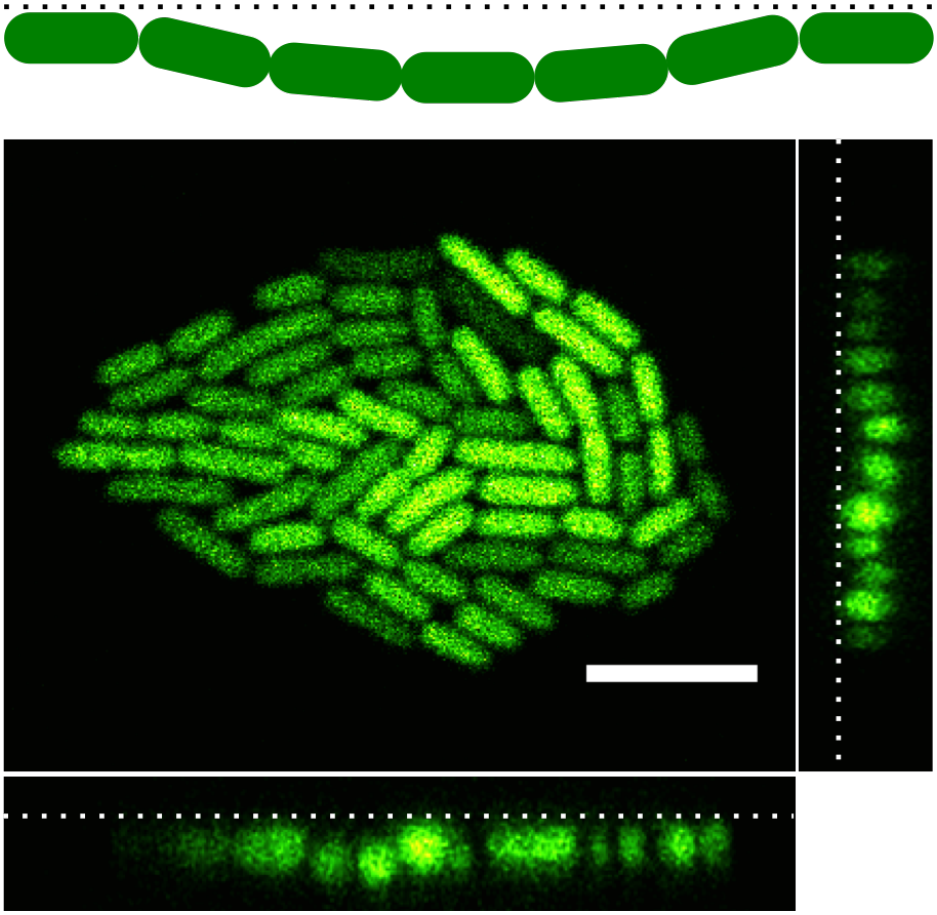

Figure 6.12: [Top] Schematic of a single layer of bacteria where the centre of the colony has deviated into the agarose. [Bottom] A single layer bacterial colony, which is undergoing this flexing process. Dotted lines indicate the plane at the bottom of bacteria at the extremity of the colony.

across the imaging area.

It is clear, from Figure 6.16 that $\mathrm{Num_{bac}}$ is not monotonic with agarose concentration as there is a clear peak at 3 % concentrations. This is in good agreement with Grant *et al.* and Lloyd, when considering the area of the primary layer of bacteria at the point of buckling, who find peaks at 2.5 % and 3 % respectively [48, 91]. Additionally, the peak seen in Figure 6.16 resembles the rate of growth variation seen in Figure 5.12 (p. 71), indicating rate of growth of the bacteria on agarose is important in determining $\mathrm{Num_{bac}}$.

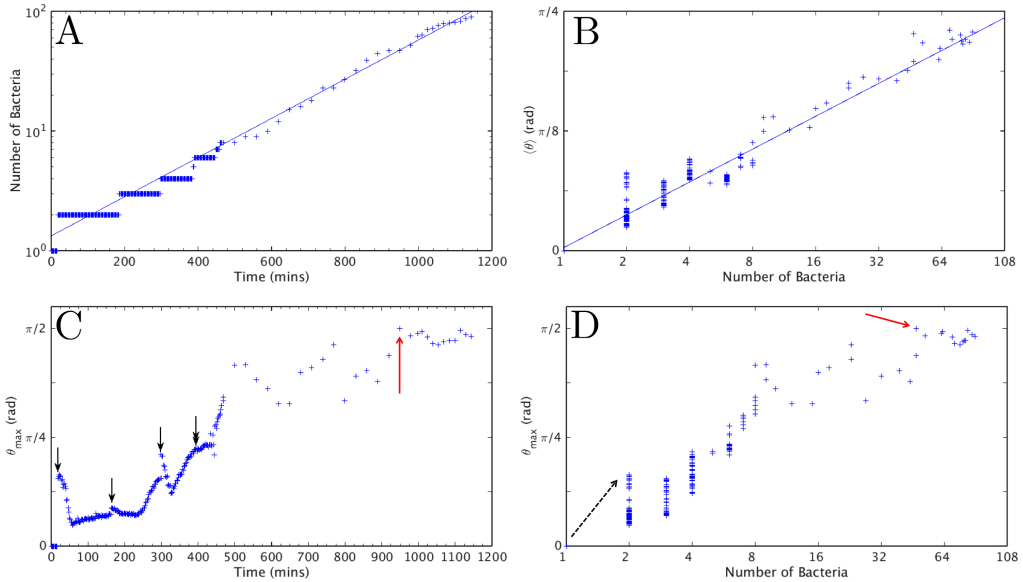

Figure 6.13: [A] Growth of bacterial colony as a function of time. Exponential fit (blue) to the data is $1.33e^{3.8 \times 10^3 t}$. [B] Variation of mean angle relative to agarose surface ($\langle\theta\rangle$) as function of time. $\langle\theta\rangle$ increases as the number of bacteria increase indicating the buckling point is the result of accumulation of pressure exerted in the initial growth layer. This shows the term 'buckling point' is misleading, since the buckling event is not a step change in $\langle\theta\rangle$. Instead, a 2D layer of bacteria on agarose exhibits 3D structure very early in the colony formation, and increases steadily throughout the colony development generating additional layers in the process. [C] Variation of maximum angle $\theta_{\max}$ as a function of time from initial measurement. $\theta_{\max}$ increases in a similar fashion, tending towards 0.5π, where the buckling event occurs (red arrow). [D] $\theta_{\max}$ as a function of number of bacteria present in the colony. A sharp increase in $\theta_{\max}$ is seen at each division (first indicated with dotted arrow). $\theta_{\max}$ tends to 0.5π where the buckling event occurs (red arrow).

6.4.1 Buried bacteria colony structure

Although work in this thesis has concentrated on surface growing colonies, it is also possible to analyse buried bacterial colonies (such as those in Figure 4.13, p. 53) in a similar manner using Besselling's code. The seven colonies imaged in Figure 4.13 were analysed using Besselling's code and $\langle\theta\rangle$ were measured (Figure 6.14). In contrast to Figure 6.13, $\langle\theta\rangle$ (A) remains approximately 0 as Num_{bac} increases but the standard deviation is large suggesting the distribution of θ is uniform across 180°. This is confirmed by viewing boxplots showing the median, 25 and 75 percentiles and maximal and minimal outliers (B). Although time-course information is unavailable for these colonies, the seven colonies contain different numbers of bacteria, allowing some temporal information to be extracted. This temporal information indicates that there is no variation in $\langle\theta\rangle$ as Num_{bac} increases.

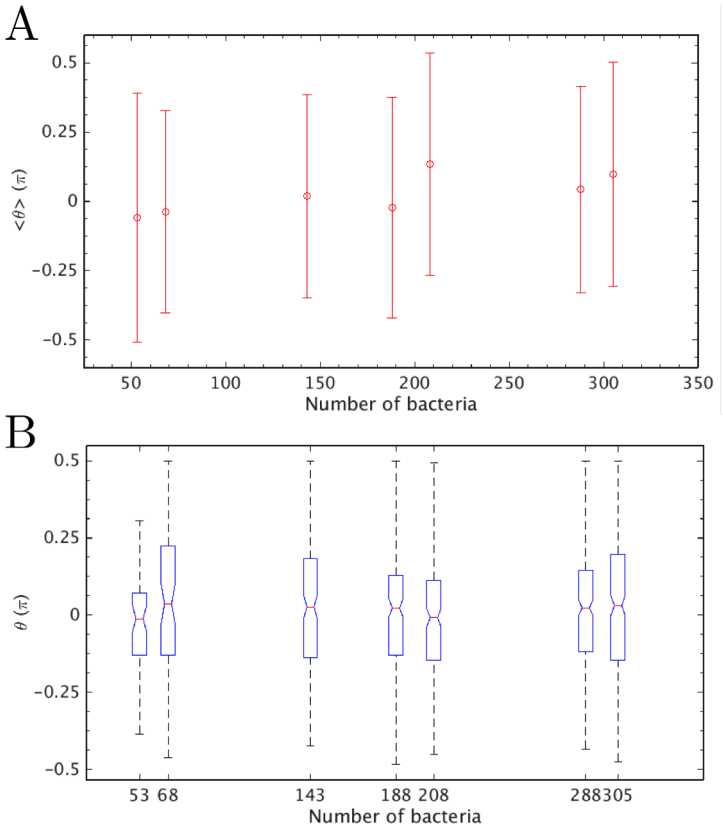

Figure 6.14: [A] Variation of mean angle relative to the agarose surface for seven buried bacterial colonies. $\langle\theta\rangle$ remains approximately 0 as the number of bacteria present in the colony increases. Error bars show the standard deviation and indicate that there is a large distribution of θ throughout all the colonies. [B] Boxplot showing the median (red line), 25 and 75 percentiles (box), 95 % confidence in the median (notches) and maximal and minimal outliers (dotted lines). The boxplots indicate the orientation of bacteria throughout the buried colonies is uniform through 180°.

6.4.2 Comparison to previous studies

Further comparison between the surface colony study and previous studies performend by Grant*et al.* [48] and Lloyd [91] is difficult due to differing methods of measuring the colony at the point of buckling.[5] But by approximating the dimensions of a bacterium in colonies grown on agarose in both Grant and Lloyd's experiments as 4.0×0.8 µm it is possible to extract an approximate value of $\mathrm{Num_{bac}}$ in each case. Figure 6.17 (p. 94) shows $\mathrm{Num_{bac}}$ for colonies with approximate doubling times of 20 min, 60 min and 75 min, with data for 20 min and 60 min doubling times being adapted from measurements obtained by Diarmuid Lloyd in experiments conducted

[5]Both Grant and Lloyd use the colony area at the point of buckling to compare between agarose concentrations rather than counting individual bacteria due to the reduced resolution available as a result of their imaging methods.

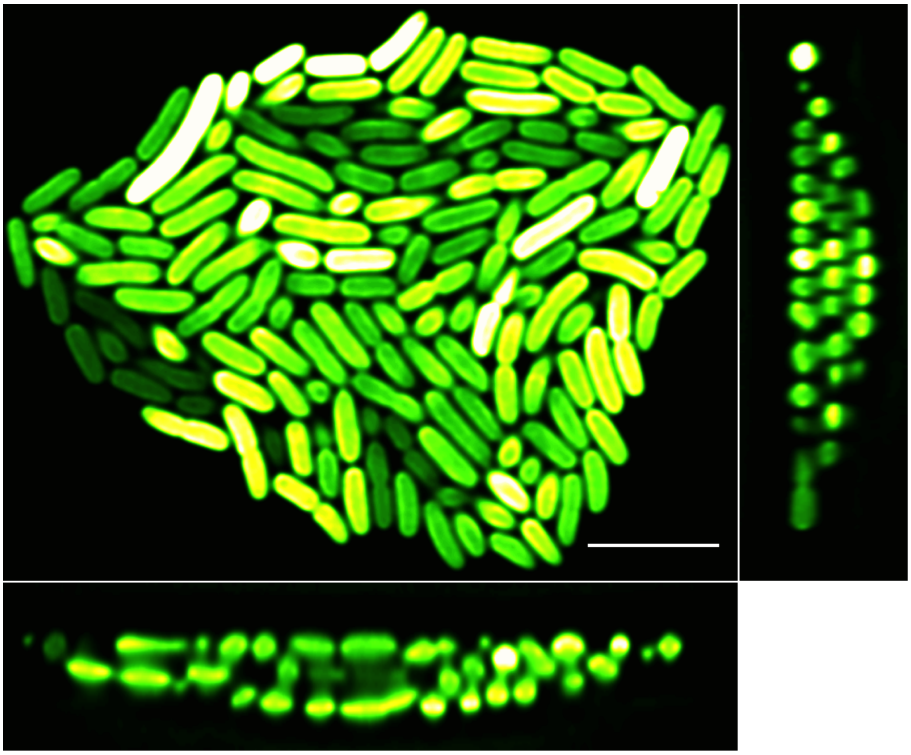

Figure 6.15: Single bacterial resolution of 3D colony grown on 3 % M9 agarose. Bacteria can be seen growing in three distinct layers, the primary layer on the agarose surface and two additional layers where invasion into the agarose has occurred. All bacteria can be distinguished within the sample allowing information on the spatial location and orientation of all bacteria in 3D to be extracted for analysis. Scale bar is 5.0 µm. Supplementary Movie A.11 (p. 136) shows the sectioning of this figure as a movie and Supp. Movie A.12 (p. 137) shows a 3D representation of the colony.

as part of his postgraduate studies [91]. What is immediately clear is that there is an increase in $\mathrm{Num_{bac}}$ as the doubling time of the bacteria decreases.

Qualifications to comparisons between experiments

It it important to note that the conditions under which experiments in this thesis are conducted are different to those of both Grant and Lloyd [48, 91]. Experiments undertaken by both Grant and Lloyd were performed at 37 °C, with the difference in colony doubling time in Lloyd's experiments achieved through variation of the nutrient available to the bacteria [48, 91]. In contrast, experiments conducted in this thesis were conducted at 22 °C, for simplification of the imaging process, and additionally, the strains used for both Grant and Lloyd's experiments, although also derivatives of MG1655, are not identical to that used for my experiments. The strain used by Grant *et al.* is an *E. coli* K-12 BW25113 derivative with the green-fluorescent protein (GFP)

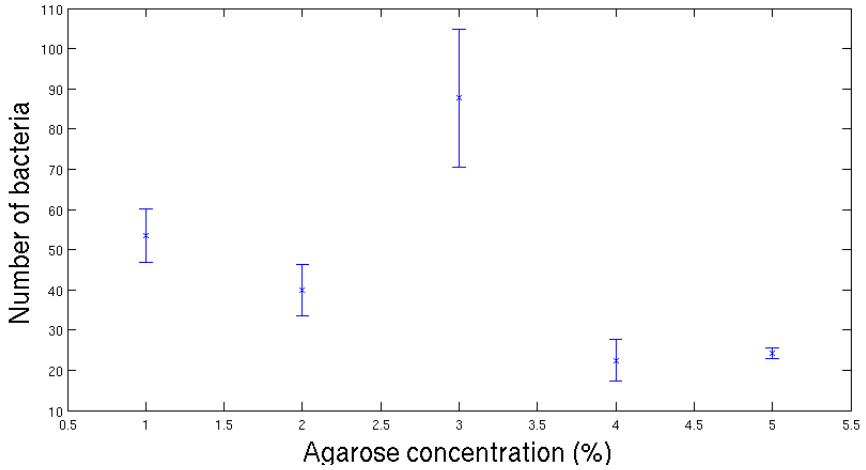

Figure 6.16: Number of bacteria within colony at the initial development of a second layer of bacteria as the concentration of agarose is varied from 1 % to 5 %. The number of bacteria present at the buckling point does not vary linearly with the agarose concentration. Rather a clear peak is seen in the number of bacteria present for concentrations of 3 % agarose relative to the others. Error bars show the standard error on the mean.

expressing plasmid PKK_PdnaA-GFP while Lloyd's strain of MG1655 contains yellow-fluorescent protein (YFP) bound to the chromosome. This is important as insertion of a plasmid affects the metabolism of the bacterium and therefore the growth rate, which we have shown to be important in the development of colonies.

To ensure that a comparison can be made between the strain used in this thesis and that used by Lloyd, I compared a strain of chromosomal fluorescing bacteria identical to that used in Lloyd's experiments, but expressing GFP, by imaging under identical conditions to the plasmid strain used in this thesis (Chapter 3, p. 19). For colonies grown on 2 % M9 agarose at 22 °C I find that $\mathrm{Num_{bac}}$ is the same as for other experiments conducted at 22 °C (Figure 6.18, p. 95) confirming the reduction in $\mathrm{Num_{bac}}$ is attributable to the rate of growth of the bacteria in the colony, not an artefact of the strain.

6.5 Discussion and conclusions

The ability to resolve bacterial colonies at a single cellular resolution when densely packed opens up many possible avenues of investigation into bacterial colony growth and development. Extraction of the physical parameters of the bacteria in the microcolony clears the way to producing a full 4D (three spatial dimensions plus time) sectioned micrograph of a bacterial colony, from seed bacterium to death, analogous to the lineage of other biological samples such as *C. elegans* [1]. Furthermore, understanding the

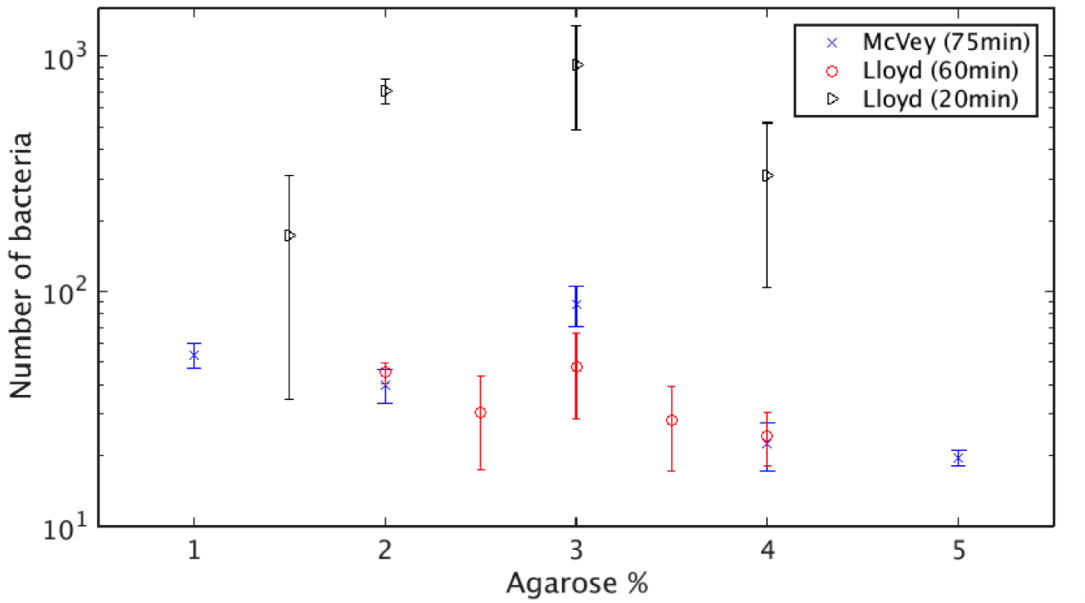

Figure 6.17: Comparison of number of bacteria present in the colony at the point of buckling for bacteria growing with different doubling rates (shown in brackets). Data for doubling rates 60 min and 20 min are adapted from work carried out by Diarmuid Lloyd as part of work undertaken in his postgraduate studies [91]. Errors are standard errors on the mean.

development of individual bacteria in the microcolony when compared to their isolated state will increase understanding of how microcolonies and biofilms help to protect and nurture the bacteria ensconced within them.

Throughout this chapter, I have highlighted areas where additional investigation would provide insight into the development of buckling colonies, but perhaps the most interesting of these is the ability to track the movement of individual bacteria in the colony. This would prove useful in obtaining more information on the nature of the growth of the secondary layers of bacteria in the colony, in order to determine whether they grow as a result of new bacteria arriving from the primary layer or as a result of division of bacteria already in the secondary layers. Additionally, being able to track the location of bacteria in the colony will lead to an enhancement of the models used to describe these structures, for instance, should the bacteria be seen to be moving considerably along the surface of the agarose as bacteria divide, it will determine the suitable models for investigation of the mechanical forces exerted on the bacteria in the colony. Finally, extraction of curvature information from the bacteria (Chapter 4, p. 48), both when isolated and in the microcolony, will produce information on the structure of the bacterial cell membrane, the elastic properties of the bacteria when

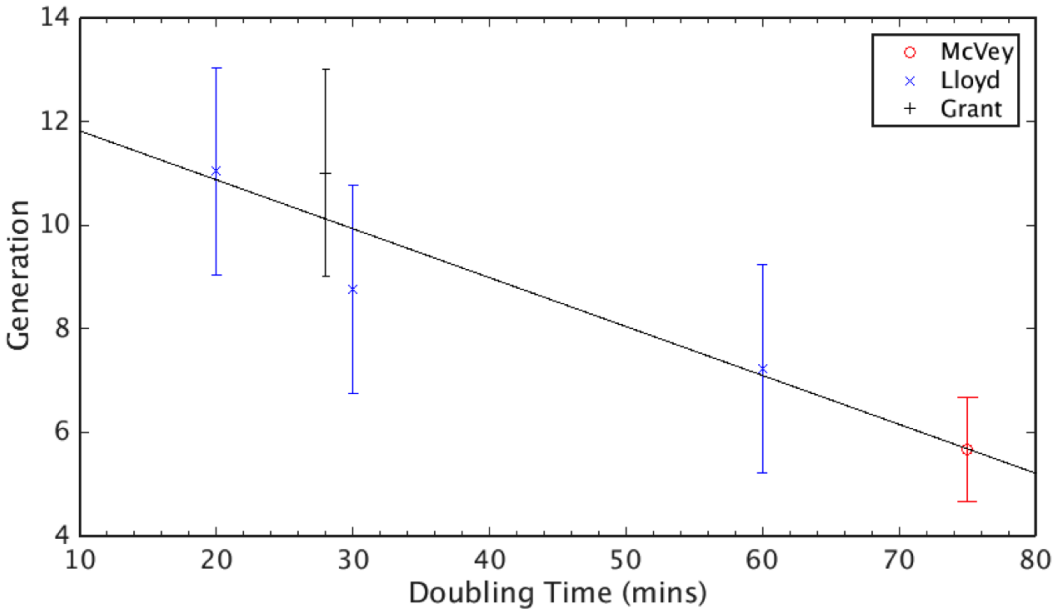

Figure 6.18: Number of bacteria present in the colony at buckling (Num_{bac}) as a function of the colony doubling rate. There is a clear decrease in Num_{bac} as the doubling time of the bacteria within the colony increases. Data from this thesis (red) is included here along with data adapted from Grant *et al.*(black) [48] and Lloyd (blue) [91]. Error bars are standard error on the mean.

in macrostructures such as colonies and the effect neighbouring bacteria have on the external stresses exerted on individuals when in closely packed structures.

In this chapter I have shown confocal microscopy is capable of resolving an individual bacterium in bacterial colonies grown on agarose and that, even when the colony is a single layer of bacteria growing on the surface, there is deviation of individual bacteria in 3D. As the bacteria grow and extend on the surface they not only alter their position in the xy plane but they invade the agarose pad, with an increase in θ_{max} immediately after division. Additionally, after this sharp increase at division θ_{max} decreases, indicating the bacteria relax to lie approximately parallel to the agarose surface. The mean angle of the bacteria from the surface ($\langle\theta\rangle$) is seen to increase as the number of bacteria increases, indicating the buckling event is not an isolated occurrence but is the result of a continuous accumulation of pressure in the colony. The term 'buckling point' is therefore misleading since the buckling event is not a step transition where a 2D colony suddenly develops three-dimensionality. Instead, a 2D layer of bacteria on agarose exhibits 3D structure very early in the colony formation, and increases steadily throughout the colony development generating additional layers of bacteria as part of this process.

Similarly, as the colony develops on the surface, the bacteria at the centre of the colony are confined on all sides by other bacteria and, as this happens, the central bacteria are forced higher into the agarose in order to grow and divide. This results in the creation of a secondary layer of bacteria above the primary layer and by resolving the bacterial colony at an individual bacterial level, the development of the colony through the buckling point can be probed on a single cell resolution, rather than relying on population level interpretations (such as the area of the colony at the point of intrusion into the agarose). The number of bacteria present at the buckling event ($\mathrm{Num_{bac}}$) is seen to vary with agarose concentration, with a peak at 3 % agarose (weight) concentrations. This is in agreement with previous studies by Grant *et al.* [48] and Lloyd [91] who found peaks at 2.5 % and 3 % agarose concentrations respectively. Additionally, the growth rate of individual bacteria is also seen to peak at agarose concentrations of 3 % (Chapter 5, p. 57), suggesting that the rate of growth of a bacterium is a dominant factor in the invasion of the bacterial colony into the agarose pad.

Finally, comparison of studies by Grant *et al.* [48] and Lloyd [91] indicates $\mathrm{Num_{bac}}$ decreases as a function of doubling time, again suggesting that growth rate is important in bacterial invasion into the agarose.

Chapter 7

FtsZ and its role in the division of a bacterium

7.1 Introduction

FtsZ is one of the key proteins associated with the division process of bacteria. In this chapter, I report a study of FtsZ structures in a growing *E. coli* colony, and compare my results with previous work on isolated cells.

FtsZ was first identified by Bi *et al.* in 1991 [138]. Since then there has been concerted effort to understand FtsZ and associated proteins, particularly the Min proteins, which cooperate to produce septation [100, 139–142]. FtsZ is believed to be the only protein that exerts an inward-directed force on the cell wall of between 20 pN/monomer and 30 pN/monomer, presumably causing septation [143]. As with other proteins in the bacterium, it is believed that FtsZ transfers between sites helically along a cytoskeleton on the cell membrane [144–146]. It is highly mobile, with a diffusion coefficient similar to monomeric membrane proteins [142, 147]. Studies are conflicting on the nature of FtsZ association with the cytoskeleton. Thanedar *et al.* suggested that the proteins oscillate along the cytoskeleton before localising at the division site [145], while Peters *et al.* found no evidence for such an oscillation in *Bascillus subtilis* [147]. Jennings *et al.* found clear evidence that FtsZ forms a helix in *Bascillus subtilis* [148]; however subsequent investigations of other cytoskeletal proteins have cast doubt. Ursell *et al.* saw no evidence of helical arrangement of MreB, a protein closely identified with the cytoskeleton [149]. The conflicting literature highlights the difficulty of visualising subcellular structures in bacteria, due in part to limitations in imaging (Chapter 2, p. 7), although these have been alleviated in recent years through the application of advanced microscopy techniques such as nonlinear microscopy [51] and confocal

microscopy (Chapter 4, p. 35).

Recently it has been suggested that the helical patterns observed in MreB are an artefact of overexpression of the protein being imaged [150]. Swulius *et al.* used electron cryotomography to show that adding the fluorescent protein YFP to MreB caused it to form helical patterns in *E. coli* while untagged (native) MreB does not. Overexpression arises from the need to obtain high signal from small relatively small concentrations of fluorophores. In order to maximise the fluorescent signal obtained from these concentrations, experimentalists cultivate samples in such a way as to encourage greater concentrations of fluorescent protein in the sample. As fluorescent tags are fused to the proteins being investigated this also increases the expression of the protein under investigation resulting in more protein being present in the bacterium than under normal conditions. Superresolution techniques such as STORM, PALM and FPALM have been used recently to investigate this discovery as they are capable of extracting information on individual proteins rather than larger structures [151,152]. These methods have shown that rather than a full helix throughout the length of the bacterium, MreB forms discrete patches that move circumferentially around the cell, questioning the idea of MreB cables forming an actin-like cytoskeleton [153].

Despite being smaller than the diffraction limit, single molecules can be imaged as PSF-sized spots in the detector. However, if the proteins assemble into superstructures, such as rings or helices, with dimensions of the order of the resolution of confocal microscopy, imaging is in principle more robust. Nevertheless, there are only a limited number of studies of the structures formed by FtsZ, although several studies have claimed to observe helices [144, 146]. Based on these studies, Andrews *et al.* propose a model predicting that the FtsZ helix should form with an angle of $\theta = 81^\circ$ to the long axis of the bacterium [154]. In their model, the helix is a rigid structure in the bacterium, displaying constant θ as the cell grows. This is surprising, as *E. coli* grows axially by the insertion of peptidoglycan into the existing cell wall in a predominantly helical pattern [155]. Thus, any helical structure already present in the bacterium should be stretched. Fischer-Friedrich *et al.* propose a different model with several helices in the bacterium, giving flexibility for the FtsZ to travel through the cell and therefore varying the helical angle relative to the long axis [156].

To initiate division FtsZ proteins form a ring-like structure at the division site with the help of a concentration gradient of MipZ and MinC [139], which act as negative regulators for FtsZ, as does the nucleoid [157]. Upon formation of the ring, FtsZ attracts other proteins to this site, which together generate septation [139]. As this occurs, the

locally cylindrical wall of the centre of a rod-shaped bacterium starts to close in on itself, separating the bacterium into two approximately equal-sized daughters. This causes the oscillating Min proteins to start to concentrate at the new caps as well as the poles of the original bacterium, gradually dislodging the FtsZ proteins from the ring site. Consequently, as the septation process begins, the Z ring is slowly disbanded, causing the FtsZ to return to a helical oscillation pattern. The whole process is then repeated [142,146]. How the FtsZ converts from a helix to a ring to initiate the septation process is not clearly understood. Theoretical studies suggest models for the different patterns of FtsZ organisation (ring and helix), but the transition between them remains undefined [154]. It is possible (and in fact common) for multiple Z rings to form in a bacterium. Upon being dislodged from the Z ring, the FtsZ proteins are believed to oscillate helically through the bacterium until they locate a low concentration of the negative regulators (e.g. MinC or nucleoid) within the bacterium and establish another ring site. As the division process is not instantaneous, the formation of this secondary ring occurs while remnants of the primary ring still exist [142,158], a phenomenon that is often observed in longer cells [159].

Much of the current literature on FtsZ and the Z ring has focussed on ways of inhibiting Z ring formation to halt septation, either by deletion of proteins [160] or by introduction of antigens [97]. However, there have also been attempts to quantify the location of the division point. Trueba first did so using brightfield microscopy [161], and found mid-point division in wild-type *E. coli* K-12 with a standard deviation of 2.5 % of the cell length at 37 °C. Guberman *et al.* used brightfield and fluorescence imaging [162], and found for wild-type *E. coli* a standard deviation of 2.9 % of the cell length from the midpoint; deletion of the genes associated with MinC expression increases the deviation to 11.5 % of cell length, all at 37 °C. Yu *et al.* performed a similar study comparing wild-type *E. coli* K-12 MG1655 with anucleate cells, and found the division to be ±2.6 % of the cell length for wild-type and ±12.4 % for the anucleated cells [159]. They also measured Z ring location at 28 °C finding no difference in the distribution. However, Gupta *et al.* found Z ring distribution increased to 7.8 % when under oxidative stress at 24 °C [163]. All of these studies were limited to measurements of isolated bacteria on agarose.

Similar studies have been conducted with *B. subtilis*, Migocki *et al.* found the location of the Z ring to be within ±6 % of the middle in units of cell length for wild-type, and ±6.7 % for $MinC^-$ (bacteria without MinC proteins) and $MinD^-$ (without MinD) cells, and ±8.4 % for $MinCD^-$ cells [164]. The use of super-resolution systems has provided some additional insight into the protein structure of bacteria, particularly in

identifying helix structures, but these studies are limited by the relative expense and the complexity of the systems necessary for image acquisition as well as the higher powers required to generate enough signal [165, 166].

A theoretical model by Tostevin *et al.* has shown that very high precision of location can be achieved by proteins that evaluate a protein gradient for a minimum, as is the case for FtsZ in Z ring formation, provided time-averaging occurs [167]. Similarly, Howard *et al.* have shown that confinement of the Z ring to a central location can be achieved if the number of MinD and MinE proteins totals 1500 each [168]. Obtaining a better understanding of the concentration of both FtsZ and Min proteins within *E. coli* is necessary to further develop models of this sort. Several studies have been conducted with this goal. Pla *et al.* measured two strains of *E. coli* K-12, finding that both MC1061 and W3110 contained approximately 5000 molecules of FtsZ per cell [169], while Rueda *et al.* found similarly that *E. coli* K-12 B/rK strains contain an average of 3200 molecules of FtsZ per cell [170]. In comparison, Lu *et al.* [171] calculate there are 15000 molecules at a concentration of $400\,\mathrm{mg\,ml^{-1}}$ in *E. coli* BL21.[1] In contrast, determination of concentrations of Min proteins has proved difficult, although an early study by de Boer [172] found that *E. coli* UT481 contained approximately 3000 molecules. Independent studies by Shih, Lutkenhaus and Ishihama [173–175] each find similar but slightly smaller values of 2000 and 1320 molecules per cell respectively for different strains of *E. coli* (Shih and Lutkenhaus MC1000 and Ishihama MC4100). This apparent reduction most likely reflects the increased measurement accuracy.[2]

To the best of our knowledge, all previous experiments have studied isolated bacteria. While this simplifies the measurement of the FtsZ ring, it leaves open the question of whether growth in a colony is different in any way. In this chapter I present results of experiments probing the FtsZ protein in growing bacteria in a 2D colony.

[1] Comparison of all of these strains using the *E. coli* Open-Wiki [102] suggests that W3110 is most closely related to MG1655 sharing two deletions and having only six different deletions (both MG1655 and W3110 have three additional deletions all of which are different).

[2] Comparison to MG1655 has shown that the MC4100 and MG1655 strains are closely related [176] and analysis of a derivative of MC4100 (BW2952) shows there are 15 variations between the two strains [177]. MC1000 is even closer having only ten genetic variations between it and MG1655

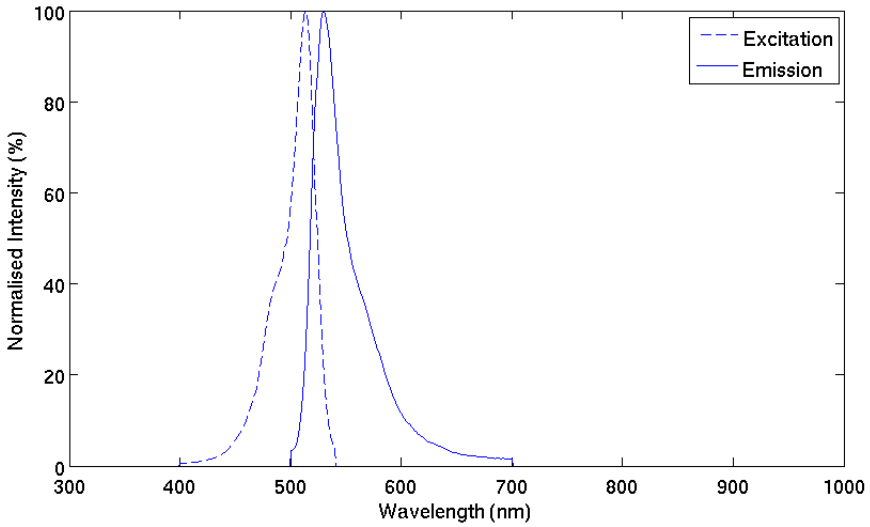

Figure 7.1: Excitation (dotted) and Emission (solid) spectra for yellow-fluorescent protein (YFP). Excitation was performed using a laser wavelength of 488 nm, in order to limit cross-talk between the excitation and emission wavelength.

7.2 Methods

7.2.1 Strains

Cytoskeletal Investigations

For experiments studying FtsZ when it is not in the ring state, *E. coli* K-12 MG1655 was transduced with pLAU80, a yellow-fluorescent protein (YFP) expressing plasmid from the Sherrat laboratory [96].[3] Figure 7.1 shows the excitation and emission spectra of YFP. Excitation was performed on a Zeiss Confocal LSM 700 microscope at 488 nm in order to limit cross-talk between incident and emitted light. Cells were grown to exponential phase in M9 media at 37 °C (Chapter 3, p. 19), diluted to concentrations of 10^7 cells/ml and placed on a rigid agarose surface of identical M9 media with 2 % (weight) agarose contained within a GeneFrame (Thermo Scientific) mounted on a microscope slide. The chamber was sealed using a coverslip, which compresses the bacteria into the surface of the agarose.

Z ring positioning

To investigate the location of the Z ring, *E. coli* K-12 YD133 with pLAU80 [96] is grown to exponential phase in M9 minimal media with 2 % glucose. Cultures are diluted to concentrations of 10^7 cells/ml in PBS and placed on agarose with identical M9 media

[3] Transduction of pLAU80 into all *E. coli* strains was conducted by Dr. Angela Dawson.

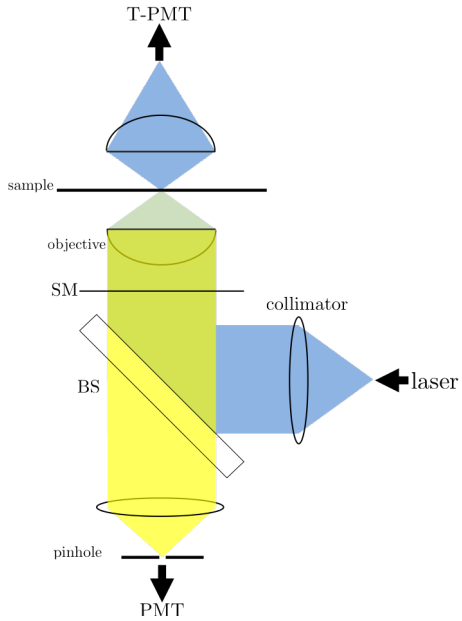

Figure 7.2: Schematic of confocal setup for imaging of FtsZ ring within *E. coli* using simultaneous YFP fluorescence (yellow) and transmitted incident (blue) laser light.

with 2 % agarose contained within a GeneFrame (Thermo Scientific) mounted on a microscope slide. As with the cytoskeletal investigations the sample is sealed using a coverslip.

7.2.2 Imaging

Image slices are taken using a Zeiss Confocal LSM 700 at resolution $\delta x = \delta y \simeq 30\,\text{nm}$, $\delta z = 100\,\text{nm}$. Three-dimensional stacks are acquired at intervals of 2 min or 5 min, much faster than the doubling time of the bacterium. Simultaneous acquisition of YFP fluorescence and part of the transmitted excitation laser light permit the location of the FtsZ. The transmission image shows the outline of the bacterium and is used without fluorescent tags associated with the cell membrane. The setup used to acquire the YFP (yellow) and transmitted images (blue) is shown in Figure 7.2. The YFP fluorescence was acquired by epi-detection in a PMT located in Channel 2 of the Zeiss Confocal LSM 700 and image analysis was performed using ImageJ [106]. The pixel dimensions were calibrated and images acquired from the two channels (transmitted and YFP) were merged and rendered for measuring.

7.3 FtsZ in the cytoskeleton

YFP is arabinose induced in our cells. We therefore need to starve *E. coli* MG1655 of glucose, which inhibits the uptake of arabinose [98]. Prolonged starvation ($\sim$ 1hr) gives rise to filamentous cells that fail to divide. Fluorescence imaging of FtsZ-yfp

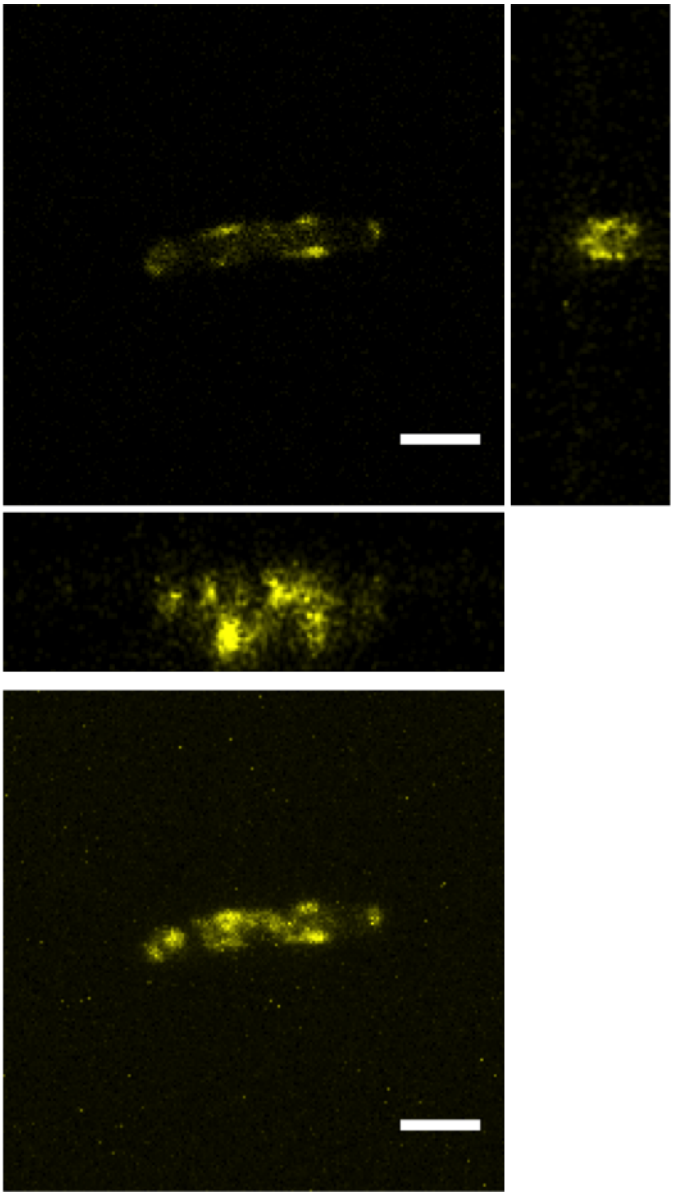

Figure 7.3: [Top] YFP-fluorescence image (xy plane and accompanying orthogonal images) of FtsZ cytoskeletal structure in *E. coli* MG1655 through prolonged removal of glucose from M9 growth media ($\sim$1 hr) during exponential growth phase. Scale bar is 2.0 µm. [Bottom] 2D projection of the 3D stack clearly showing the helical structure FtsZ utilises to travel through the cell between Z ring formations. Scale bar is 2.0 µm.

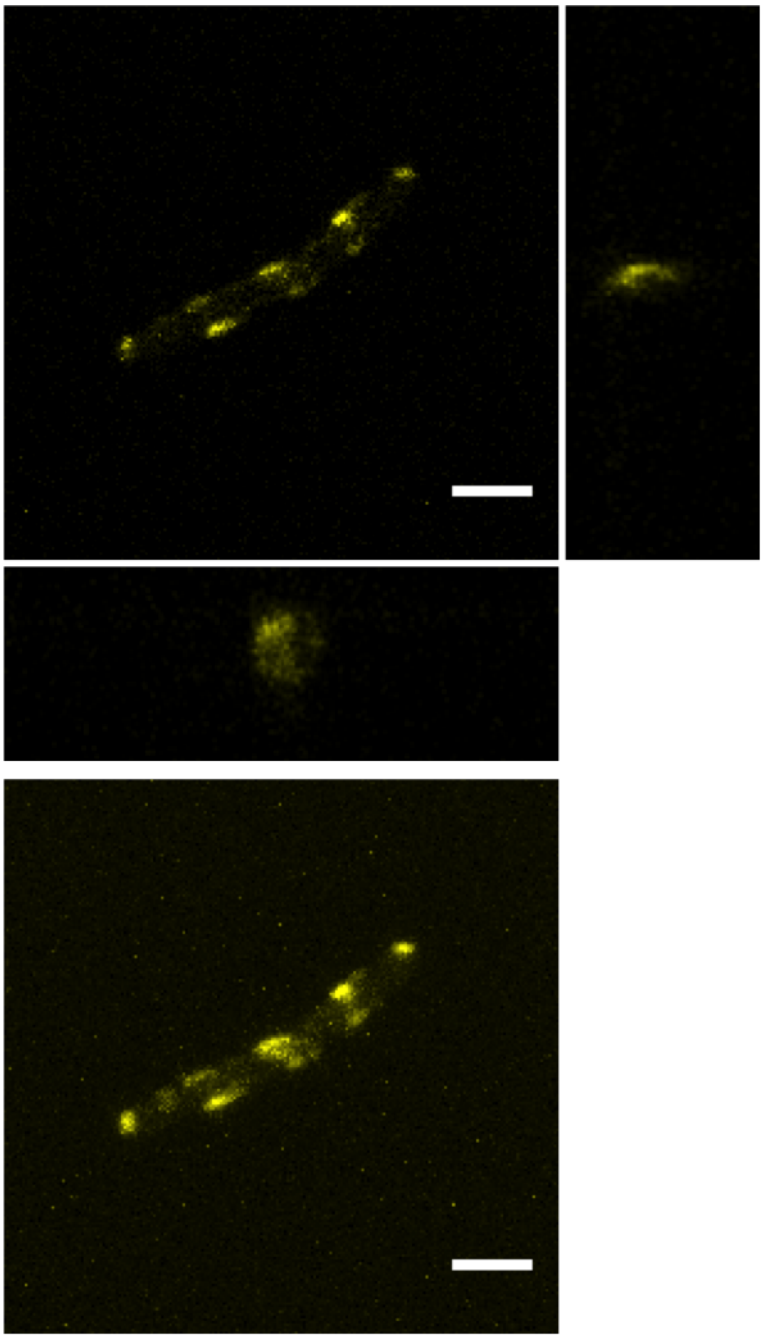

Figure 7.4: [Top] YFP-fluorescence image of FtsZ cytoskeletal structure in filamentous *E. coli* MG1655 with accompanying orthogonal images. Scale bar is 2.0 µm. [Bottom] 2D projection of the 3D stack through the bacterium produced in ImageJ by summing the pixel intensity across the entire stack. The FtsZ proteins fail to successfully form a Z ring within the bacterium which subsequently grow filamentous. A helical structure is seen as the proteins oscillate through the bacterium. Scale bar is 2.0 µm.

in the bacteria during this period allows investigation of how FtsZ moves through the bacterium. Figure 7.3 shows structures formed by FtsZ immediately after cells are placed on agarose. An apparent helical structure is seen spanning from one pole to

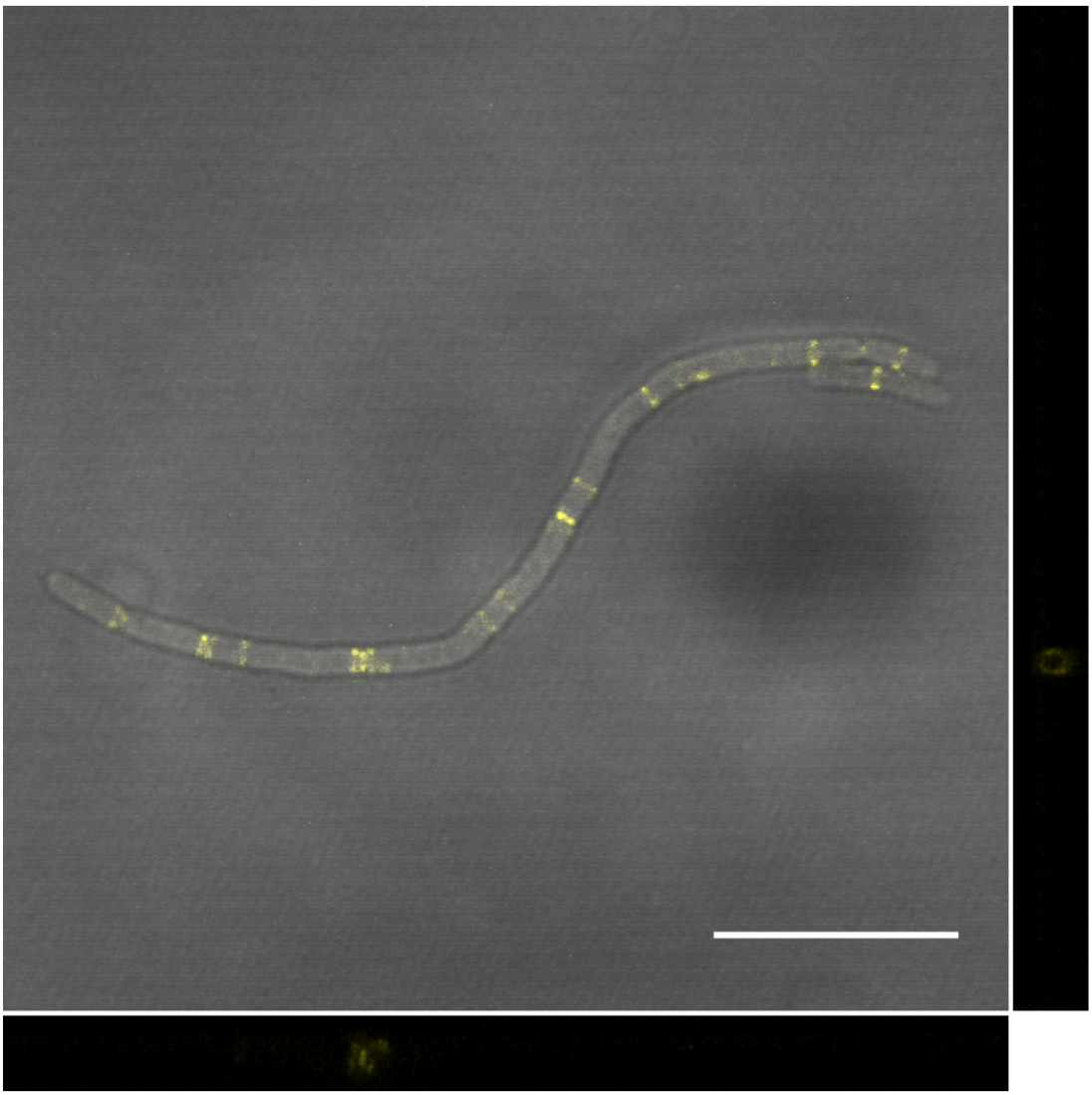

Figure 7.5: YFP-fluorescence (yellow) and brightfield (xy plane only) composite image of formation of Z ring in filamentous *E. coli* MG1655. Clear evidence the FtsZ protein is now forming rings is seen in the orthogonal slices through the bacterium. Despite growing to rod-lengths far greater than unstarved bacteria these filamentous bacteria are still viable as reproducing cells. Scale bar is 10.0 µm.

the other, particularly in the bottom image, which is a 2D projection of the three-dimensional stack (top figure) and accompanying orthogonal slices.

Due to starvation conditions, over the prolonged imaging period (up to 2hrs) bacteria

grow into filamentous states, Figure 7.4 (p. 104), with FtsZ helices. In these filamentous cells, FtsZ is still capable of Z ring formation. Figure 7.5 (p. 105) shows the sudden collapse of the type of structure shown in Figure 7.4 into multiple rings. This process

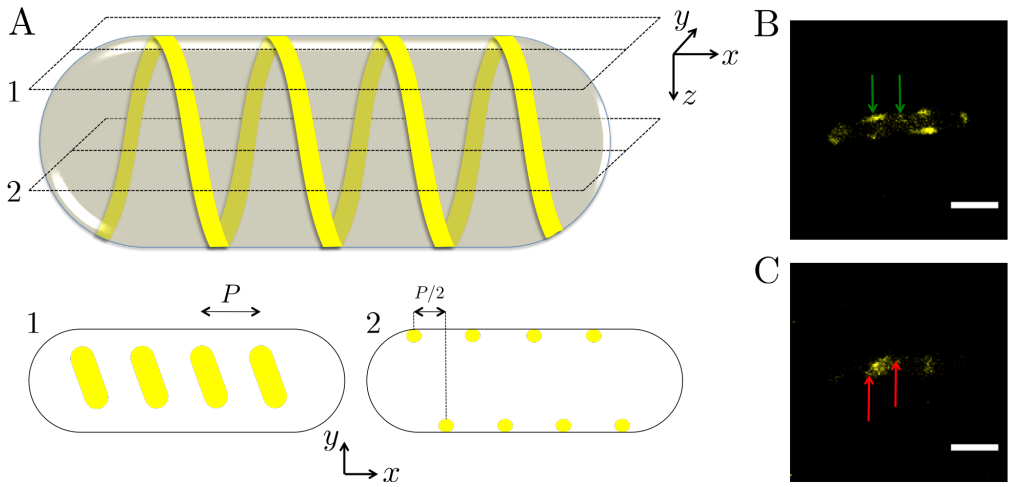

Figure 7.6: (A) Schematic detailing the 3D nature of the cytoskeleton (yellow) within an *E. coli*. In the sample two focal planes (dotted lines) are specified. (1) Linear structures are seen detailing part of the helical structure in apparent spirals when imaging at the 'top' of the bacterium. (2) With a focal plane within the bacterial structure, points are seen on either side wall of the bacterium which correspond to a half-period distance of the subsequent helical structure. Period (P) and half-period ($P/2$) measurements are shown in schematic 1 and 2 respectively. (B) YFP (yellow) image corresponding to focal plane (1). Green arrows indicate the full period measurement made. Scale bar is 2.0 µm. (C) YFP (yellow) image corresponding to focal plane (2). Red arrows indicate a half-period measurement. Scale bar is 2.0 µm.

was very rapid (<5 min), below the time resolution of this experiment. What brings about these two different states is unclear, but a disruption in the replication of the nucleoid would lead to a spread of nucleoid material along the length of the bacterium, inhibiting Z ring formation. This could be tested by the introduction of a fluorescent tag to the nucleoid. Alternatively, disruption to the Min protein cycle may mean that FtsZ cannot assemble at concentrations high enough to induce septation. This hypothesis is similarly testable using a fluorescent tag. Likewise, a reduction in the production of FtsZ could result in a similar phenomenon, where FtsZ is unable to assemble at high enough concentrations to induce septation. With the exception of the final supposition, which is unlikely when considering Figures 7.4 and 7.5 where the fluorescent intensity remains constant beyond the doubling time, either of these factors may account for the filamentous growth.

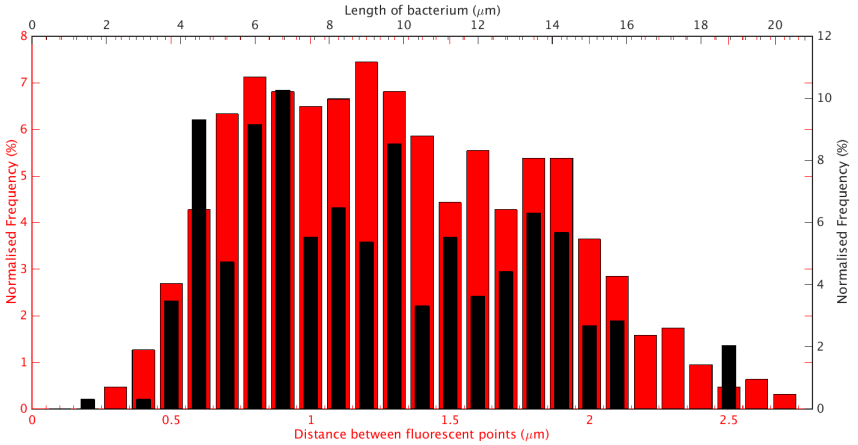

Figure 7.7: Histogram of cytoskeletal period of FtsZ protein. The broad peak of the distance between fluorescent points (red) is closely correlated to the length of the bacteria (black) suggesting that the helix expands as a function of the length of the bacterium. Measurements were performed for 80 individual bacteria.

7.3.1 Determination of the helix angle

Using images such as Figure 7.3 (p. 103) it is possible to test the constant-helix-angle theory of Andrews *et al.* [154] by measuring the distance between bright fluorescent spots in the long axis of the bacterium. However, the use of confocal microscopy to image these bacteria provided an unwelcome problem in the determination of the helical structure of the cytoskeleton. Figure 7.6 shows the challenge of deducing quantitative information on helically-organised FtsZ proteins inside a bacterium. What is seen in a 2D slice critically depends on the position of the slice in the bacterium. A focal plane near the top wall of the bacterium (1) means fluorescent spots are a full period (P) apart, whereas a focal plane in the centre of the bacterium (2) results in half period spots. As distinction between the period and the half period is difficult from the images, measurements of the distance between all adjacent fluorescent spots were made (Figure 7.6B-C), in order to determine the period of the cytoskeleton.

Figure 7.7 shows a wide distribution of distances between fluorescent points (red). This broad peak is in close agreement with the distributions of the lengths of the bacteria (black). A sharp peak distribution of the period of FtsZ only emerges if the period of the helix is normalised by the length of the bacterium (Figure 7.8). Two peaks are evident at 0.070× and 0.145× the length of the bacterium and correspond to the half-period and period of the FtsZ helix respectively, suggesting the helix expands with the bacterium. Thus, our observations contradict the assumptions made by Andrews in his model.

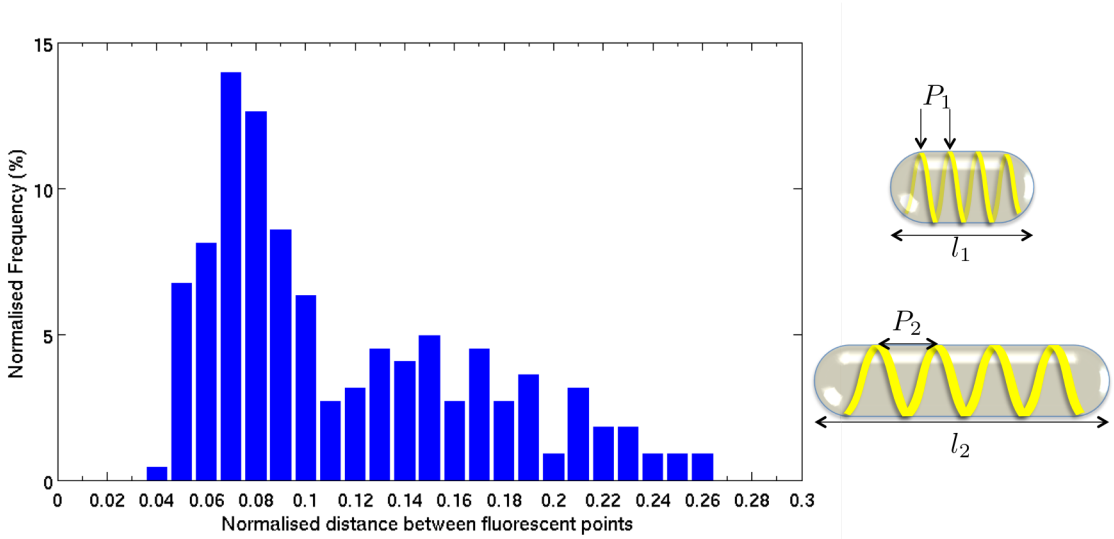

Figure 7.8: Histogram of cytoskeleton period and half-period distributions (left). Peaks are seen at 0.070× and 0.145× the length of the bacterium, which we identify as the half-period and full period of the cytoskeleton.Schematic of the expansion of the helical period (P_1 to P_2) as the bacterium grows (l_1 to l_2). The change in the period is proportional to the length of the bacterium, $\frac{P_1}{l_1} = \frac{P_2}{l_2}$. Measurements were made for 80 individual bacteria.

7.3.2 Rapid division of filamentous bacteria

Figure 7.9 (p. 109) shows a time-course of stacks taken at 5 min intervals of a filamentous bacterium that has formed Z ring structures along its length. The filamentous bacterium divides rapidly into a chain of smaller bacteria with the time between division at the first ring and subsequent rings being far shorter than the division time of bacteria grown under typical growth conditions[4] so that the bacterium is seen to progress through approximately 3 generations in the time a single division would be expected. In filamentous bacteria analysed in this study, the formation of more than one Z ring is seen simultaneously (<5 min) with these Z rings quickly developing into septation points. Consequently, the cell divides far more quickly than the normal doubling time, from one very long bacterium into a chain of *E. coli* of similar length to unstarved cells on agarose. This transition from filamentous bacteria to a rapidly dividing chain is likely to be caused by the change of nutrient availability to the bacterium. Since the bacteria are starved in order to induce fluorescence, they will undergo stress. Starvation disrupts the division site (namely FtsZ location) of a bacterium so that when the bacterium is reintroduced to a nutrient rich environment it is unable to divide despite continuing to grow. I speculate that as this occurs the internal structures of the bacterium (the

[4]For this strain grown on M9 agarose at room temperature (22 °C) the division time is of the order of 60 min.

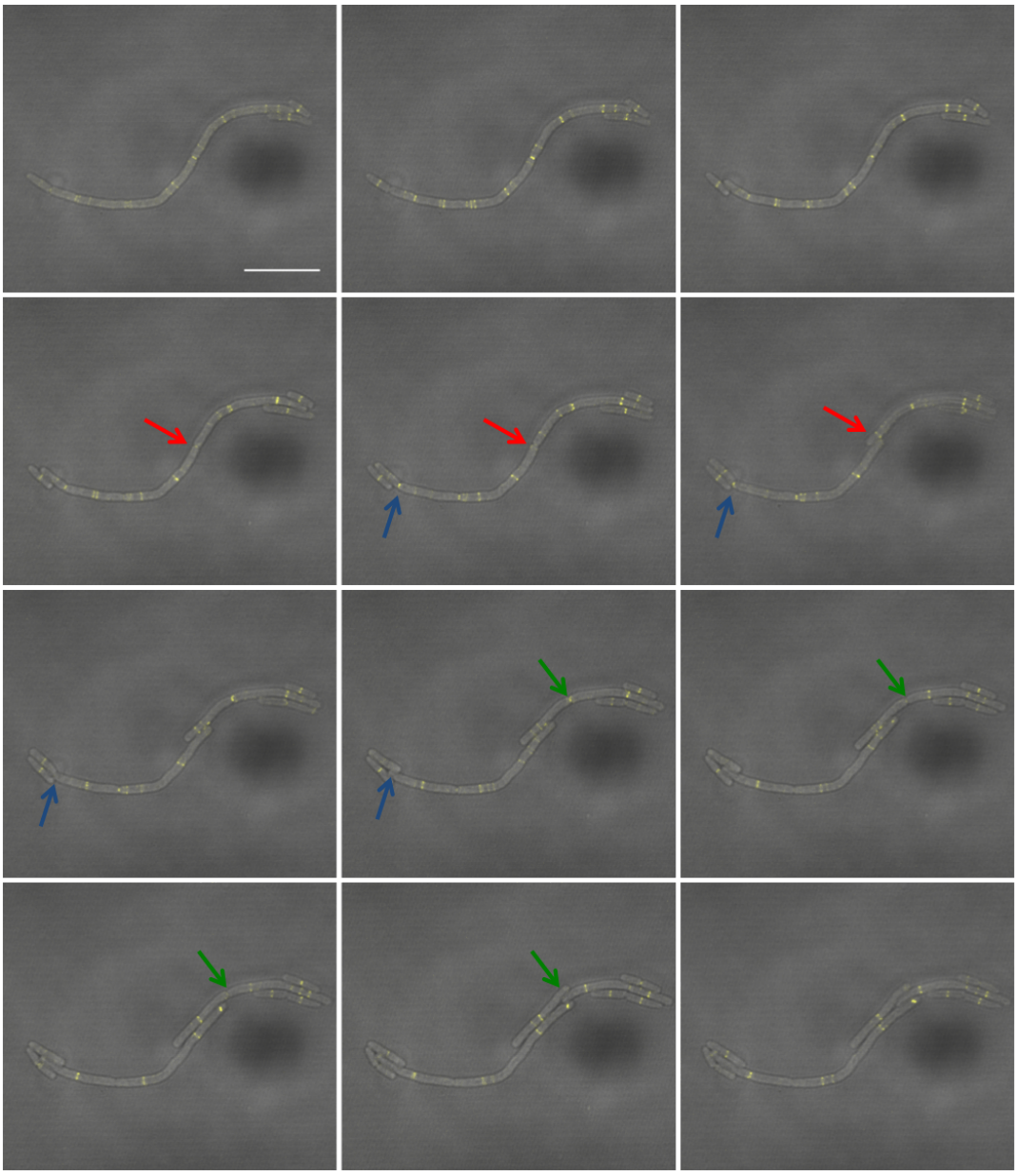

Figure 7.9: YFP-fluorescence (yellow) and brightfield composite image of a single filamentous bacterium as it transitions through the division instigated by Z ring formation. The series runs from left to right, top to bottom and each image is separated by 5 min. The bacterium is seen to divide (example divisions are indicated by a coloured arrow) into multiple smaller cells over a period far less than a typical life-time of a bacterium grown under typical growth conditions (approximately 60 min). Scale bar is 10.0 µm.

nucleoid in particular) continue to replicate as normal so that after a period of time in a nutrient rich environment, defined by the time when FtsZ can organise into rings, septation occurs rapidly. This leads to the rapid division of a filamentous bacterium into a chain. This is one of the reasons why filamentous cells growing on chilled food pose a serious health hazard when the food is warmed up.

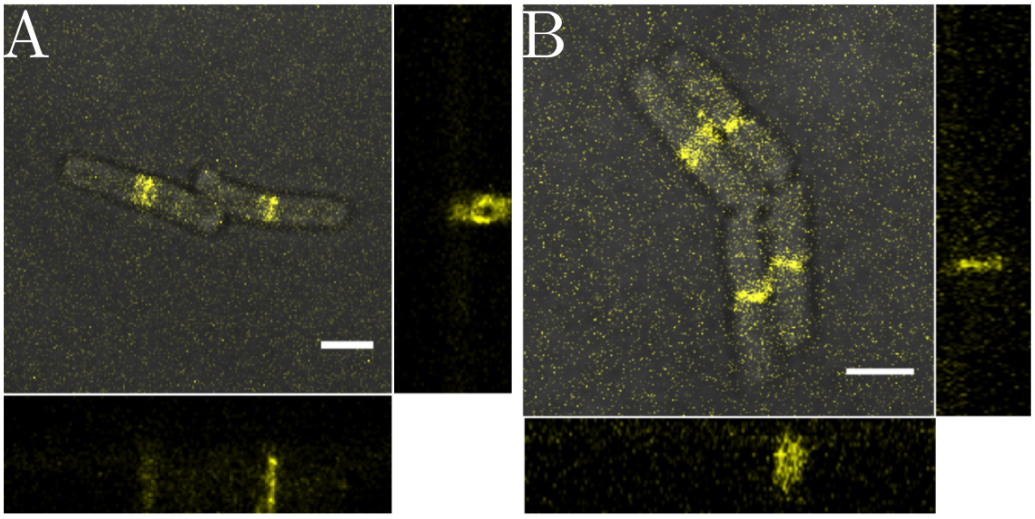

Figure 7.10: Three-dimensional YFP-fluorescence (yellow) image of Z ring formation in second (A) and third (B) generation bacteria on M9 agarose (2 %). The YFP-fluorescence is overlaid in the *xy* plane with a brightfield image generated by picking some of the transmitted laser beam off onto a photomultiplier tube (PMT) positioned for transmitted imaging. Image slices were taken through the sample at 0.1 µm steps allowing clear determination of the protein structure of the Z ring within the bacterium. Orthogonals are taken through the right hand of the bacteria in second generation bottom right bacterium of third generation, both show the ring structure of FtsZ. 3D reconstructions of these bacteria are available as Supplementary Movies A.13 (p. 137) and Supplementary Movie A.14, (p. 138). Scale bars are 2.0 µm.

7.4 FtsZ septation

7.4.1 Development of the FtsZ ring in time

Before septation, FtsZ is seen to collect in a ring approximately at midcell, but until this study no clear optical sectioning of this structure has been successfully performed for either single cells or cells in colony. Figure 7.10 shows the YFP-fluorescent protein tagged to FtsZ in second (A) and third (B) generation bacteria on agarose. FtsZ is seen to aggregate into rings in both bacteria, with the orthogonal image showing a bright central ring structure formed in the right hand bacterium (A) and bottom right (B), as seen in the *xy* plane projection. However, in the *xy* plane the central rings are seen to not form singular rings, but rather appear to form a double ring or partial double

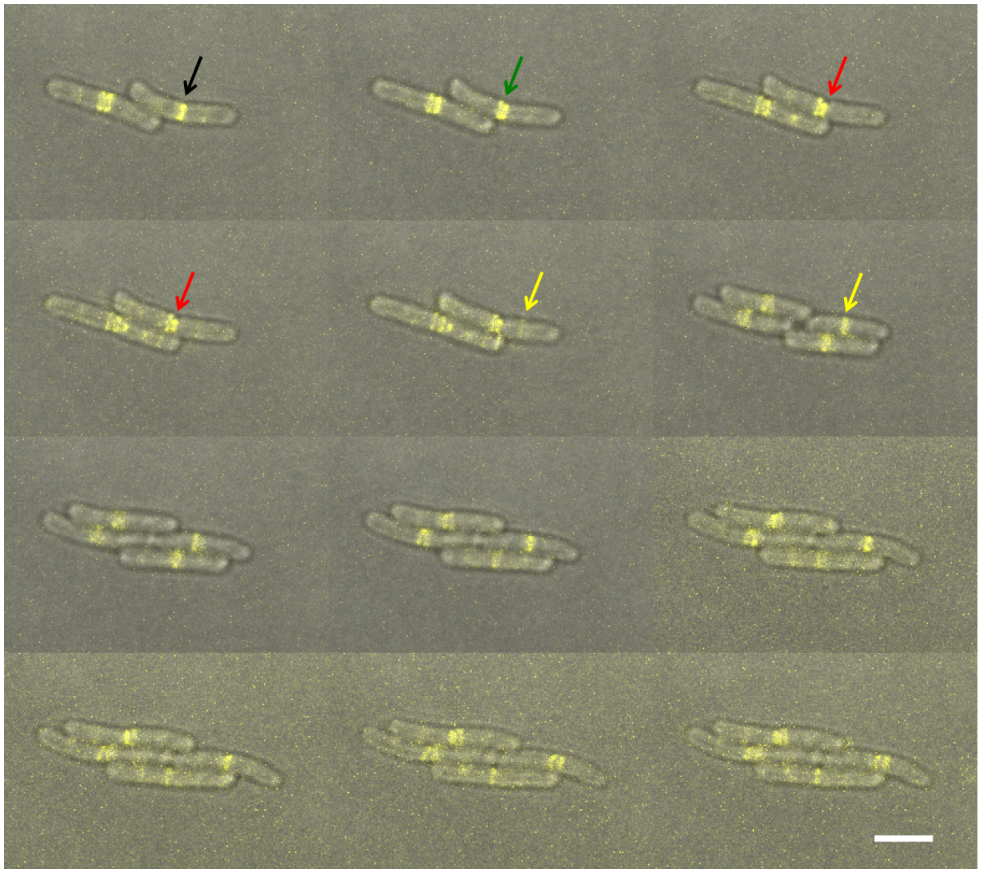

Figure 7.11: Z ring formation and disruption in *E. coli* grown on 2 % M9 agarose as a function of time. Transmitted PMT (grey scale) images are overlaid with YFP signal (yellow) indicating the location of concentrations of FtsZ protein. FtsZ rings are seen to form at approximately the midcell of each bacterium (black arrow), then form a double ring structure (green arrow) where one of the rings contracts as the septation process is initiated (red arrow). Upon initiation of the septation process the ring disbands, forming at the midcell of the daughter bacteria (yellow). Initially, this secondary ring is faint indicating the concentration of FtsZ proteins present is small, but within 5 min returns to a similar intensity to the original ring. Sequence of images is left to right and top to bottom and scale bar is 2 µm. Supplementary Movie A.15, p. 138 provides a 2D rendering of this figure as a function of time.

rings. Viewing the 3D reconstructions of these images (Supplementary Movies A.13, p. 137 and A.14, p. 138 in Appendix A), produced by loading confocal stacks of the YFP-FtsZ into Vaa3D [178], these double ring structures develop from the Z ring after the septation process has been instigated.

Using confocal microscopy we are able to image a single bacterial colony over several generations (imaging of a single bacterium has been performed for up to approximately 3 hrs without loss of fluorescence). This makes it possible to visualise FtsZ as it forms and disbands Z rings as the bacterium develops from a single isolated cell surrounded

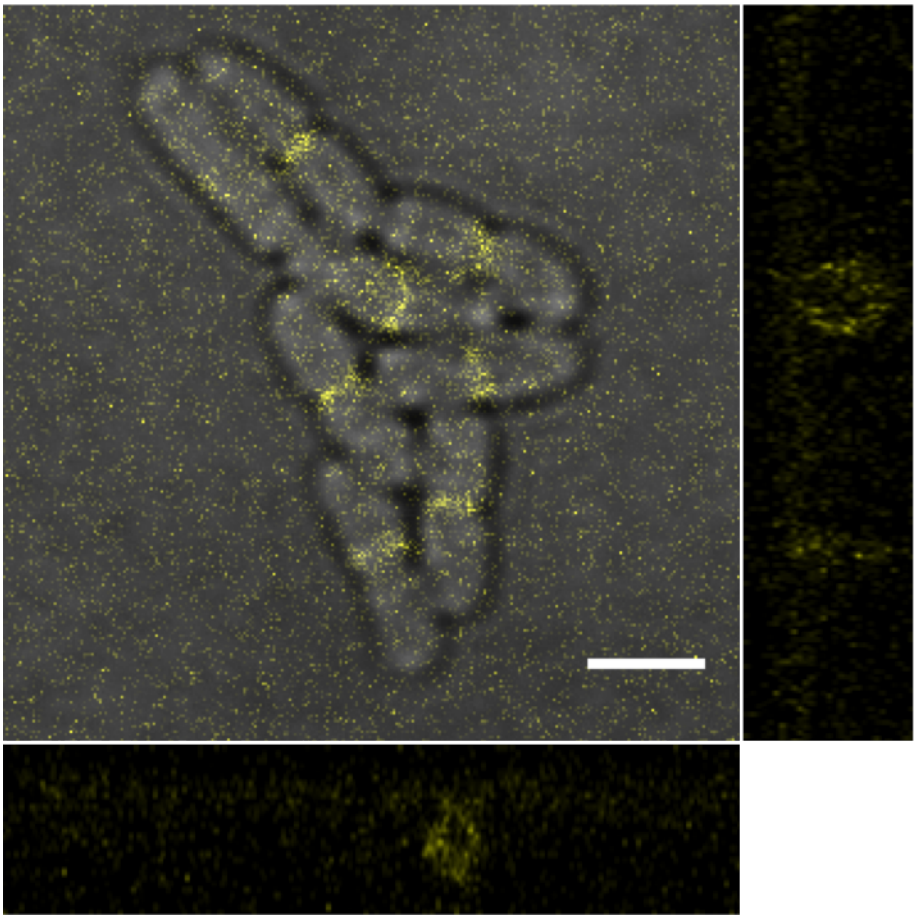

Figure 7.12: Three-dimensional YFP-fluorescence image of Z ring formation in an *E. coli* bacterial colony. The YFP-fluorescence (yellow) image is overlaid in the x-y plane with a brightfield image of the bacterial colony obtained from transmitted incident laser light used to excite the fluorescent protein. Image slices were taken through the sample at 0.1 µm steps allowing clear determination of the ring structure. Orthogonal images show FtsZ continues to form a ring structure in the bacteria. Scale bar is 2.0 µm.

by agarose into a colony. Figure 7.11 (p. 111) shows the transmitted PMT signal (grey scale) overlaid with the YFP signal (yellow) of a bacterial colony as the cells grow and divide. FtsZ rings (bright yellow) are seen to form at approximately the midcell of the bacterium (black arrow), then form a double ring structure (green) before one of the rings contracts as the septation process is initiated (red). Upon initiation of the septation process the ring begins to disband, forming at the midcell of the daughter bacteria (yellow). Initially, this secondary ring is faint indicating the concentration of FtsZ proteins present is small, but within 5 min returns to a similar intensity to the original ring. Imaging over 3 hrs results in a loss of fluorescence (Figure 7.12) due to photodamage caused by the intensity of the incident laser beam on such a small volume of sample, however, part of this reduction in intensity may be explained by

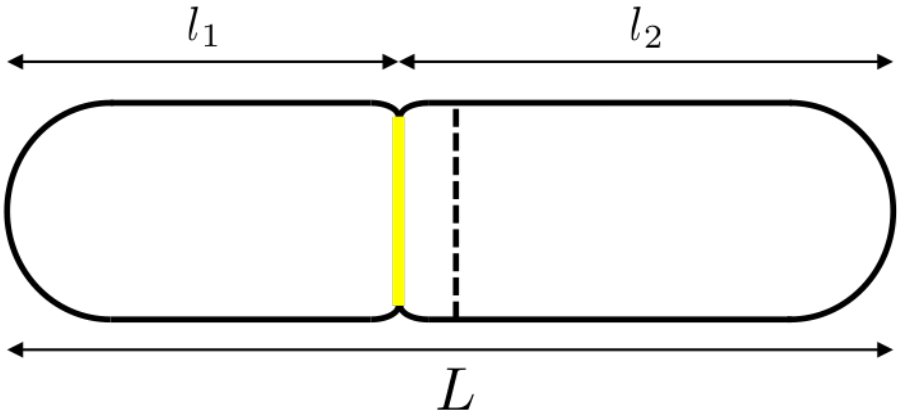

Figure 7.13: Schematic of measurements made for Z ring location. For each bacterium the linear distance between each pole and the YFP expressing Z ring (yellow) were made using ImageJ [106] (l_1 and l_2 respectively). The difference between these two measurements was then taken and normalised by half the length of the bacterium, L as outlined in Eq. 7.1 (p. 113). This allowed precise measurement of the deviation from the midpoint of the bacterium (black dotted line).

physical factors, for example a depletion of the number of proteins, a concept discussed in greater detail later in this chapter.

7.4.2 Distribution of Z ring position widens with generation

To obtain information on the position of the Z ring (P_z) relative to the centre of the bacterium, measurements of the distance between each pole and the YFP expressing Z ring were made (Figure 7.13, l_1 and l_2) by manually drawing lines between the identified points in ImageJ. Manual measurements were made due to the need to measure points across the two parts of the composite image (transmitted and YFP), and due to the large variation in intensity associated with the YFP fluorophores, resulting in difficulty in thresholding the image. The magnitude of the difference between the two distances was taken and normalised by twice the total length of the bacterium (L),

$$P_z = \frac{\mid l_1 - l_2 \mid}{2L} \tag{7.1}$$

where l_1 and l_2 are the distances between each pole and the FtsZ ring respectively (Figure 7.13).

Separation of the bacteria into approximate generations from the seed bacterium (generation 1) is made based upon the number of bacteria present in the colony at each time point. This approximation is possible for relatively new colonies of bacteria as the doubling time remains synchronised beyond the first five generations [50], however,

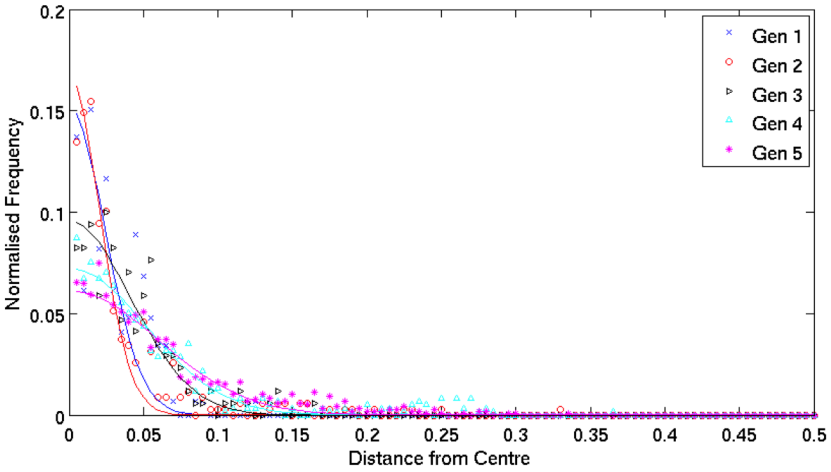

Figure 7.14: Normalised distribution of Z ring location relative to the midcell of the bacterium for different generations of bacteria on M9, 2 % agarose pads. The position of the Z ring (P_z) is calculated using Equation 7.1 (p. 113). The distribution is seen to increase as the generation increases from the seed bacterium (blue crosses) to fifth generation (pink *).

for a more thorough separation into bacterial generations, or if imaging was performed over more generations, single bacterial tracking to determine the generation of each individual in the population would be necessary.

The resulting distributions of Z ring position, Figure 7.14, resemble one-sided Gaussian distributions and consequently, for each generation a half Gaussian distribution is fitted to the data (solid lines). Since the difference in Z ring distribution is small, for clarification, Figure 7.14 is replotted with data excluded as Figure 7.15. It is clear the distribution of the Z ring location increases as the generation increases from the seed bacterium (blue) to generation 5 (pink) and from the fits performed for each generation it is possible to obtain a value, σ, for the distribution width from the Gaussian distribution, $P(x)$,

$$P(x) = e^{\frac{-x^2}{2\sigma^2}} \tag{7.2}$$

where x is the distance of the Z ring from the midcell of the bacterium and σ is the deviation from the midpoint.

Plotting $\log_{10} P(x)$ against x^2 (Figure 7.16) allows a determination of the distribution width, σ (Table 7.1), using

$$\sigma = \sqrt{\frac{1}{2m}} \tag{7.3}$$

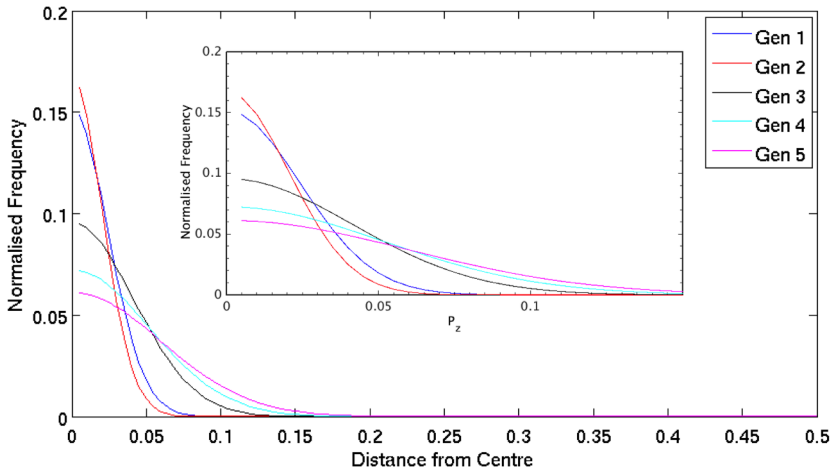

Figure 7.15: Gaussian fits for FtsZ location relative to midcell for bacteria of different generations. P_z is calculated from Equation 7.1 (p. 113). Generation 1 (blue) is the seed bacterium used to start the colony growth on the agarose pad. A clear trend is evident in the broadening of the distribution from generation 1 to generation 5 (pink).

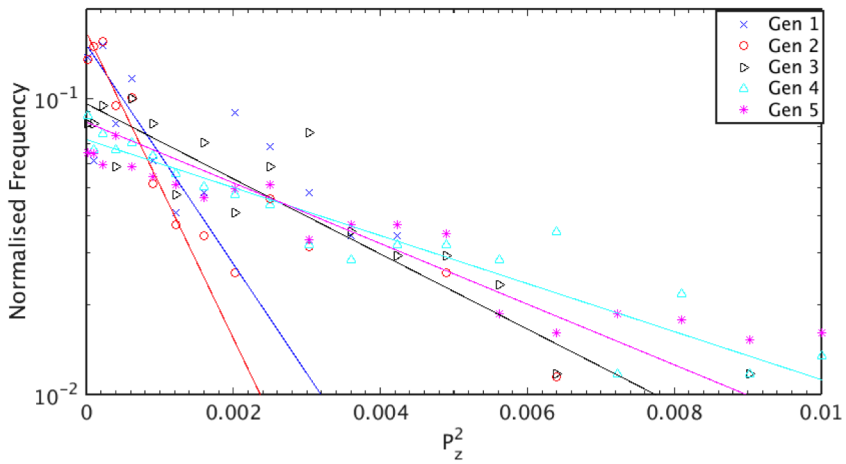

Figure 7.16: Fitting of $\log_{10} P(x)$ in order to obtain the Gaussian width of distribution of Z ring of each generation of bacteria. The calculated widths (σ) are summarised in Table 7.1

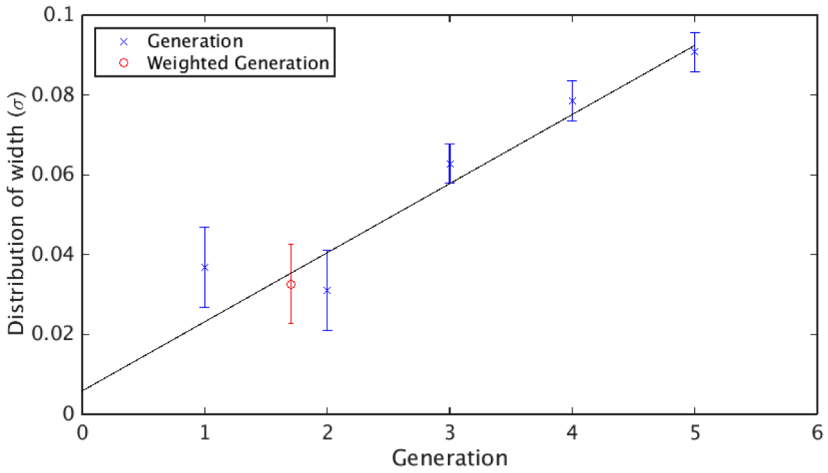

Figure 7.17: Distribution width (σ) as a function of bacterial generation. σ increases linearly with generation. A weighted value (red circle) is provided for generation 1 and 2 due to the close proximity of these distributions to the resolution of the confocal microscope.

where m is the gradient of the straight line obtained from linearising Eq. 7.2.

The width of the distribution increases with the generation from 0.50 ± 0.04 for generation 1 to 0.50 ± 0.09 for generation 5 (Figure 7.17). The decrease in the distribution width from generation 1 to 2 is not attributed to the reduced number of measurements used (146) since generation 3 has a similar sized population but gives a distribution width 1.5× greater. Rather, the distribution widths of generations 1 and

Bacterial Generation	Sigma	Error on sigma	Number of measurements
1	0.037	0.005	146
2	0.031	0.002	349
3	0.063	0.003	170
4	0.079	0.004	596
5	0.091	0.003	1174

Table 7.1: Calculations of σ for Z ring distributions in different generations of bacteria grown on M9 2 % agarose. Values for σ are obtained through fitting a Gaussian distribution to the data set for each generation of bacteria and linearising using Eq. 7.3 (p. 114). The reduced number of measurements obtained for generation 1 is not believed to account for the decrease in distribution width seen between generation 1 and 2, but rather is an artefact of the proximity of the diffraction limit of confocal microscopy. The reduced number of measurements for generation 3 is attributed to loss of fluorescence in this time region.

2 are at the diffraction limit of confocal microscope; a bacterium of length 3 µm with $\sigma = 0.037$ means the ring is located ±120 nm from the midcell, (r_{confocal} =139 nm (Eq. 2.3, p. 10)).

Figure 7.17 shows a linear increase in the distribution width at a rate of 0.018 ± 0.008 per bacterial generation. The data for generation 1 and 2 are combined (red circle) since both measurements are at the diffraction limit of the confocal microscope. There are three possible explanations for the widening in distribution of the Z ring location within colonies; a reduction in the temperature during the experiment; the introduction of external stresses on the bacterium created by the surrounding bacteria; or the relaxation of negative regulators of Z ring formation. The next section of this Chapter examines these possible explanations.

7.4.3 Explanations for widening distribution

(A) Temperature variation during experiment

Experiments probing the effect of temperature on the location of the Z ring are conflicting, Yu *et al.* measured σ at 37 °C and 28 °C finding no difference in the distribution of the Z ring in their bacteria [159]. Gupta *et al.* found σ increased when the temperature was reduced from 37 °C to 24 °C [163] indicating a variation in the temperature during the experiment could cause σ to widen.[5] While a relaxation of temperature on the time-scale of the experiment (approximately 5 hrs) is unlikely, cultures may retain heat from the growth phase during the initial measurements (i.e. the first generations) before cooling as the generation increases. Agarose may retain heat and slowly release this to the sample, or the *E. coli* may only react to the temperature variation on a similar time-scale to the experiment. Incubating samples at 37 °C between measurements allows this to be tested.

37 °C sample preparation

Five identical samples of *E. coli* YD133 were prepared (§3.2.3, p. 26) and placed in a static incubator at 37 °C until required for measurement, when they were removed, imaged and replaced in the incubator. For each measurement, samples were only exposed to 22 °C for the period of the experiment (approximately 10 min) before being replaced in the incubator.

37 °C measurements

Due to the small scale of this experiment, the number of bacteria in each generation was too small to compare generation directly (generation 1 contained only 39 bacteria) and, consequently, generations were collated into two distinct groups, early generation

[5] Cultures are grown at 37 °C, while experiments are conducted at 22 °C.

and colony bacteria, in order to perform statistical analysis on the population.

Early generation bacteria are generations 1 and 2 (seed and immediate daughters). Combining these two generations is possible since the bacteria are not confined by bacteria surrounding them. Additionally for experiments conducted at 22 °C both distributions measured are at the resolution limit of the confocal microscope. In contrast, colony bacteria are defined as bacteria which are in the third generation or above (i.e. have undergone two or more divisions from the seed bacterium) and while these bacteria exhibit varying Gaussian distributions in Figure 7.15 (p. 115), if we are only interested in verifying that an increase in σ is not an artefact of temperature variation, we need only determine whether a similar phenomenon is observed at 37 °C as at room temperature. Additionally, it can be presumed that the relative weighting of the three distributions (generation 3, 4 and 5) will be similar for both temperatures.[6]

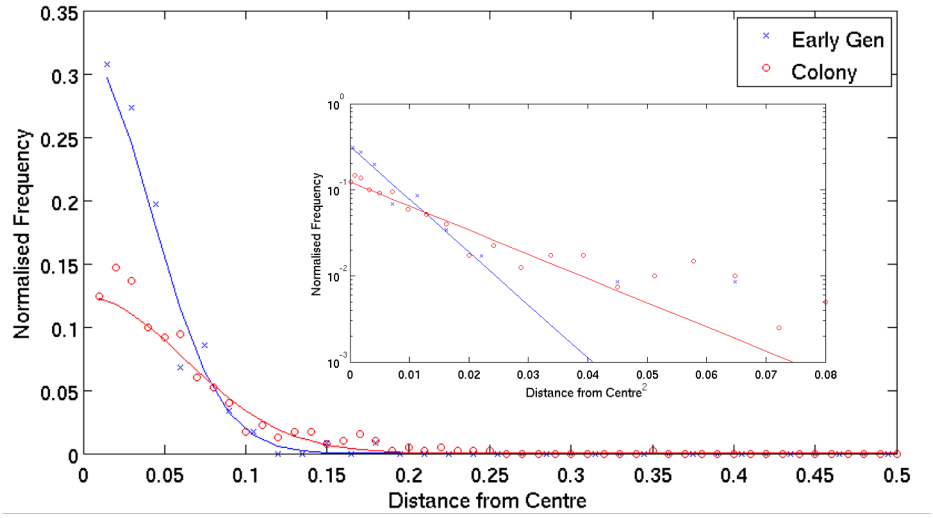

Figure 7.18: Distribution of Z ring location relative to the centre of the bacterium in both early generation (blue crosses) and colony (red circles) at 37 °C. Although binning is more noisy, a similar difference in distribution is observed between early generation and colony growth, with the early generation distribution being more tightly centred on the mid-cell of the bacterium.

Figure 7.18 shows that P_z for bacteria in early generation (blue crosses) is far narrower than bacteria in colony (red circles). To provide direct comparison Figure 7.19 shows a

[6]The assumption is valid since for each colony imaged the number of bacteria in generation 3 will be 8, for generation 4, 16 and for generation 5, 32. These ratios will remain constant to each other so long as all colonies being imaged are imaged over all three generations. While it should be noted that the statistical drop in generation 3 experienced in the room temperature measurements (Table 7.1, p. 116) will not be evident in these experiments as a result of the decreased imaging time at each location on the agarose, the skew of the statistics to generation 4 and 5 is small.

	37°C	Room
Early Generation	0.50 ± 0.05	0.50 ± 0.06
Colony	0.50 ± 0.08	0.50 ± 0.09

Table 7.2: Z ring distribution from the mid-cell of the bacterium as calculated for different growth temperatures. All units are normalised to the unit length of a bacterium.

similar distribution is observed when considering early generation and colony bacteria at 22 °C. Calculating σ (Equation 7.3, p. 114) for early generation and colony bacteria

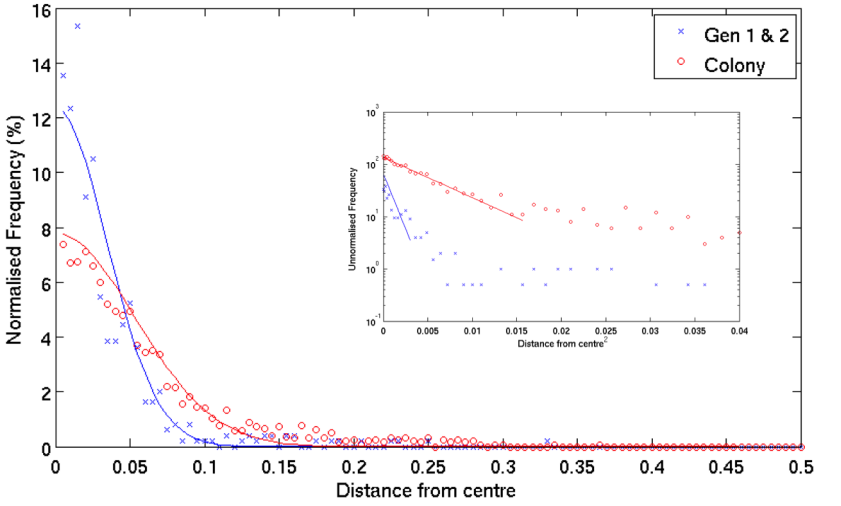

Figure 7.19: Fitting of Gaussian distribution to early generation (blue crosses) and colony (red circles) bacteria distributions. For both early generation and colony bacteria the gaussian fit is very good. The inset shows the region over which the fit is performed.

produces 0.50 ± 0.05 and 0.50 ± 0.08 (Table 7.2) respectively. Similarly, for 22 °C σ is found to be 0.50 ± 0.06 and 0.50 ± 0.09 for early generation and colony respectively. Comparing results for 37 °C with 22 °C (Figure 7.20, p. 120) there is little difference between σ for both early generation (A) and colony (B) between the two temperatures, confirming that the increase in σ is not an artefact of temperature variation during the experiment.

(B) External stress from surrounding bacteria

The increasing width of σ may be the result of surrounding bacteria in a dense colony exerting mechanical stress on each other. External stresses, causing deformations of the cell wall, could result in a disruption of the Min oscillation. This can be tested using time-lapse fluorescence microscopy of MinD to determine the location of MinD as a function of time in isolated and colony bacteria [179]. Additionally, bending of

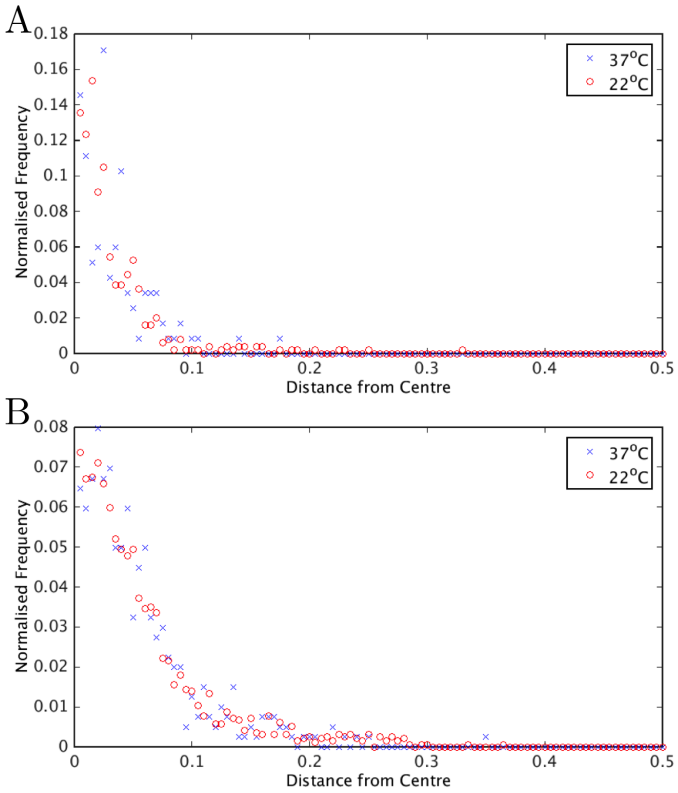

Figure 7.20: Z ring distribution as a function of temperature for bacteria in (A) early generation and (B) colony growth. Comparison between 37 °C (blue crosses) and room temperature (red circles)(approximately 22 °C) show there is no discernible difference between the Z ring distribution as the temperature is varied. This confirms that the temperature is not the cause of the difference in distribution between early generation and colony growth.

bacteria in the colony may result in asymmetrical distribution of the nucleoid, which leads to an increase in the distribution of the Z ring. A relatively simple test of this would be an expansion of the experiment conducted by Fisher *et al.* [157], where they fluorescently tagged the nucleoid of an isolated bacterium, to bacteria in a colony.

(C) Relaxation of negative regulators of Z ring formation

Alternatively, the increase in σ as the generation increases could be attributed to a depletion of Min proteins in the bacterium caused by an increased metabolic cost in growth as spatial confinement increases. It is possible to estimate the number of MinD proteins required to cause these measured values of σ for the Z ring from Howard's model by assuming a one-to-one correlation between the measured values of σ and those predicted by Howard (Figure 7.21).

As expected the number of Min proteins decreases as the generation increases but

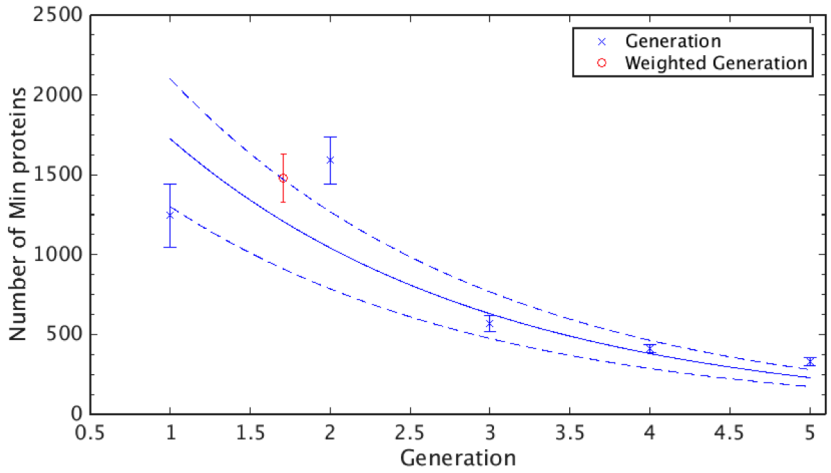

Figure 7.21: Estimated number of Min proteins present in bacteria as the generation increases from seed bacterium (generation 1) to full colonies (generation 5). A clear reduction in the number of proteins present as the generation increases would explain the increase in σ. Fitting $N = N_0 \times a^{-(x-1)}$ (solid line) provides coefficients, $N_0 = 1700 \pm 400$ and $a = 1.7 \pm 0.7$ respectively. N_0 corresponds to the number of Min proteins present in an isolated bacterium, while a defines the rate Min proteins are lost in each division. Dashed lines indicate 95 % confidence in fit.

the trend is not linear, as it is for σ (Figure 7.17). If we assume the number of proteins halves at each division the number of Min present as a function of generation (x) is defined as

$$N = N_0 \times a^{-(x-1)} \tag{7.4}$$

where N_0 is the number of proteins present at generation 1 and a is the rate at which Min proteins are lost and should vary between 0 and 2. If no proteins are produced while in colony $a = 2$.

Fitting the data to Eq. 7.4 (Figure 7.17 solid line) produces $N_0 = 1700 \pm 400$ and $a = 1.7 \pm 0.7$. N_0 is smaller than literature values (between 2000 and 3000) but the 95 % confidence in fit (dashed lines) fall within the lower limit of literature. Noticeably a is not equal to 2, implying there is some production of Min while in colony but very little.

While it is clear that there is a similar trend between the increasing σ width and the reduction in Min proteins, these two parameters do not have a direct one-to-one correlation. Howard notes this and states additional factors are important in determining σ, particularly the nucleoid, which has already been shown to influence the location of the Z ring [159, 163]. As such we are only able to suggest that there is

a reduction in Min protein concentration as generation increases.

7.4.4 Consequences of depletion of Min proteins

However, if the increase in σ with generation is at least partly caused by a reduction in the number of proteins it is difficult to see how this could be beneficial to the bacterium as there will be an increase in the production of anucleated cells in the colony. But, since the bacterium must displace the agarose media in order to grow, there is an external stress exerted on the bacterium. Thus it is conceivable that there is a metabolic cost to the bacterium causing a reduction in the growth rate, but also reducing its ability to replenish internal proteins since additional energy must be diverted to growth. Since Min proteins are not crucial to the division process of the bacterium they may be some of the first to be limited.[7] A simple way to test this hypothesis would be to label another protein in the bacterium and measure the intensity of the expression through the growth cycle, quantifying the number of proteins present. This is non-trivial experimentally as other factors will play a part, such as fluorescent bleaching and counting of such small proteins below diffraction limit but several other studies have successfully measured the number of proteins present in a bacterium using immunofluorescence [169–175,180,181].

7.5 Future work

From this study several properties of FtsZ have been identified that will require further research.

7.5.1 How does FtsZ travel through the bacterium?

By maximising the resolution of a confocal microscope in all three spatial dimensions while maintaining acquisition times short enough to provide time-course information on the structures in a bacterium, the methods outlined above are capable of resolving the true structure of FtsZ when not in a ring. It will therefore be possible to test rigorously how FtsZ travels through the bacterium as well as acquiring time-averaged images to visualise the entire structure of FtsZ outside of the Z ring.

7.5.2 Reduction of FtsZ to ring

Studying the 3D images of FtsZ several events in the life-cycle of the bacterium have been identified including initial investigations into the transfer from travelling

[7] While the FtsZ protein is required for division of bacteria, Migocki *et al.* have shown that in the absence of Min proteins in *Bascillus subtilis* the bacterium will still divide to produce two viable daughter cells [164].

structures to Z ring formation. It is already clear qualitatively that the ring is formed by a condensing of a double ring, rather than forming independently, and that the disruption of the Z ring is not instantaneous. However, in order to quantify the nature of these processes and provide information suitable for rigorous model testing, such as the model proposed by Andrews [154], a more comprehensive study must be undertaken.

7.5.3 Use of additional fluorescence to provide increased accuracy

To provide an additional check of the broadening of P_z with generation increase, the addition of a fluorescent protein that binds to the bacterial membrane of *E. coli* should be undertaken. The increased localisation of the signal provided by a fluorescent tag such as Wheat Germ Agglutinin[8] when compared to the transmitted incident laser beam will allow more precise positioning of the edge of the bacterium. Consequently it should be far easier to resolve any differences in P_z as a function of generation.

7.5.4 Extension of the technique to other proteins

Throughout this chapter experiments have been focussed upon FtsZ in *E. coli*, through which I have shown it is possible to achieve sub-cellular resolution of bacterial cells when isolated and in colony on agarose. However, the technique is not limited to a single protein and in principle any protein to which a fluorescent tag can be attached and that aggregates in the bacterium can be visualised in this way. Of particular interest to this study is investigation of the Min oscillating proteins as a function of generation in order to determine whether variation of the oscillation pattern of these proteins is the cause of the broadening of P_z.

7.6 Discussion and conclusions

In this chapter I have shown confocal microscopy can achieve sub-cellular resolution of bacterial cells in three spatial dimensions at acquisition rates well below the doubling time. I have successfully imaged and reconstructed the 3D superstructure of FtsZ throughout a bacterial lifecycle and have applied these methods to image protein structures in both single-cell and colony regimes of the bacterium. I have shown the period of the helix is a function of the length of the bacterium, in contrast to Andrews' model [154] and the period has been measured as 0.145× the length of the bacterium.

Furthermore, the distribution of the Z ring from midcell (P_z) has been measured

[8]Commercially available from LifeTechnologies `www.lifetechnologies.com/order/catalog/product/W11262`

as a function of generation, with the distribution width (σ) increasing linearly with generation from ± 0.04 (generation 1) to ± 0.09 (generation 5). This increase in σ is not an artefact of temperature, but rather it is most probably caused by a combination of two factors: external stresses exerted on the bacterium by surrounding bacteria leading to an increased metabolic cost of growth and a relaxation of negative regulators governing the location of the Z ring at midcell, through depletion of Min proteins. Using a one-to-one model linking σ directly to the number of Min proteins, the reduction in Min after each division is found to be $1.7 \pm 0.7\times$ per generation indicating there is some production of Min during growth on agarose but an additional metabolic cost to bacteria in colony stops full replenishment. The initial number of Min present in the bacterium at generation 1 (1700 ± 400) is slightly lower than literature values measured by immunofluorescence [172, 175] but is within 95 % confidence levels.

Chapter 8

Concluding Remarks

In this thesis I have shown laser scanning confocal microscopy is capable of single-cell resolution of densely packed micron-sized particles. In Chapter 4 I outlined improvements made to sample preparation and image acquisition which make this possible. By combining deconvolution processes with high resolution images of bacteria growing on a viscoelastic (agarose) surface or submerged in the viscoelastic bulk, I have shown the technique is a suitable imaging platform for obtaining high-precision single-cell resolution of bacteria when in isolated and colony growth. Additionally, through the use of reconstruction software [111], spatial and geometrical parameters of all individuals in the colony can be extracted, thus making significant steps towards the production of full cell lineages of bacterial colonies.

In Chapter 5 I have shown that bacteria growing at the air/agarose interface (i.e. not sealed by a coverslip) are submerged in the agarose. By equating the force exerted on a cylindrical body with that caused by surface tension, a value of $E \approx 300\,\mathrm{kPa}$ is calculated, in close agreement with literature (Appendix D, p. 143). Additionally, precise measurement of the length of isolated bacteria on agarose shows the concentration of agarose surrounding the bacterium affects the rate of growth, with peak growth at weight concentrations of 3 % agarose of 0.00770 ± 0.00003 unit length per minute. At agarose concentrations of 5 % the growth rate of bacteria falls to 0.00010 ± 0.00005 unit length per minute, suggesting the force exerted by the agarose on the bacterium is approaching that necessary for insertion of peptidoglycan into the cell wall. Investigating the elastic properties of M9 agarose using atomic force microscopy (AFM), the Young's modulus of 5 % (weight) agarose has been measured as $5.7 \pm 1.2\,\mathrm{MPa}$ using a pyramid tip. This is high compared to literature (Appendix D, p. 143), however, AFM measurements are highly dependent upon the geometry of the probe, and therefore measurements with a probe of similar geometry to the

hemispherical cap of the bacterium (i.e. a spherical bead of diameter 800 nm) would provide a more relevant comparison.

In Chapter 6 I have shown the mean angle of the bacteria relative to the initial growth plane ($\langle\theta\rangle$) increases linearly with the generation of bacteria up to the buckling point. This indicates the buckling point, where the colony develops additional layers of growth, is not an isolated event, but is part of a continuous increase in pressure in the colony. The maximum angle of bacteria relative to the initial growth plane ($\theta_{\max}$) also increases sharply at each division point, indicating one or both of the bacteria are not aligned with the initial growth plane. After division $\theta_{\max}$ initially decreases sharply as a function of time, suggesting the bacterium returns to parallel alignment with the initial growth phase, before increasing slowly towards the next division. $\theta_{\max}$ also trends towards 0.5π, where the buckling point occurs.

The number of bacteria present at the buckling point varies nonlinearly with the concentration of agarose, with a peak at 3 %. This is in agreement with previous studies by Grant *et al.* [48] and Lloyd [91] who found peaks at 2.5 % and 3 % respectively. This peak in number of bacteria also correlates with the peak in growth rate of an individual bacteria, (Chapter 5) suggesting the rate of growth of a bacterium is a dominant factor in the invasion of the bacterial colony into the agarose.

Finally, by imaging the septation point of *E. coli*, in Chapter 7 I have shown confocal microscopy can achieve sub-cellular resolution of bacterial cells in three spatial dimensions well below the doubling time. I have successfully imaged and reconstructed the 3D superstructure of FtsZ throughout a bacterial lifecycle and have applied these methods to image FtsZ structures in both single-cell and colony growth regimes. I have shown the FtsZ helix is a function of the length of the bacterium, in contrast to Andrews' model [154], and measured the period of the helix as 0.145× the length of the bacterium.

At the point of septation, FtsZ forms a ring at approximately the midcell of the bacterium, and instigates septation by reducing in diameter before dispersing into the new daughter bacteria. The distribution of the Z ring from the midcell (P_z) has been measured as a function of generation, with the distribution width (σ) increasing linearly with generation from ± 0.04 (generation 1) to ± 0.09 (generation 5). Increasing σ is not an artefact of temperature but is likely caused by an increase in external stress on the bacterium with generation, resulting in increased energy cost for growth and a depletion in the number of non-critical proteins produced during the lifecycle. Using a one-to-one

model linking σ directly to the number of Min proteins, the reduction in Min proteins after each division is found to be $1.7 \pm 0.7\times$ per generation indicating there is some production of Min in each generation but not enough for complete replenishment. The initial number present in the bacterium at generation 1 (1700 ± 400) is slightly lower than literature values measured by immunofluorescence [172, 175] but falls within 95 % confidence.

By showing that confocal microscopy is capable of resolving all individual bacteria in a 3D colony as a function of time, significant inroads have been made towards the goal of producing a four-dimensional sectioned micrograph of a bacterial microcolony. These advances open up many new avenues for investigation, notably providing information on the advantages experienced by bacteria when in a biofilm or colony compared to isolated growth. Additionally, by visualising protein structures contained in a bacterium, I have shown confocal microscopy can be used to obtain quantitative information from any structure which localises in a bacterium as a function of time. Consequently, as well as extending the investigations into FtsZ superstructures in a bacterium, the possible applications of confocal microscopy to the imaging of protein superstructures in the bacterium (and the effect colony growth has on them) is limited only by the number of protein types present in the bacterium.

Appendix A

Supplementary Movies

This appendix is a compendium of movie files to supplement the main body of this thesis. Given the nature of the projects undertaken as part of this thesis, there is only a finite amount of information that can be condensed from three or four dimensions into 2D representation. As such, included below are movie files that will aid the comprehension of the thesis, showing results of imaging and reconstruction in 3D and in four.

The viewing of these files is possible directly from this document by clicking on each of the images if using a version of Adobe Reader version 6 or later (available here `http://get.adobe.com/reader/`). However, some pdf viewers (Apple Preview for instance) do not support integrated video and consequently viewing of these files directly via this document is not possible. A soft-copy of movie files can be obtained by direct correspondence with the author of this thesis.[1]

[1] a.f.mcvey@ed.ac.uk

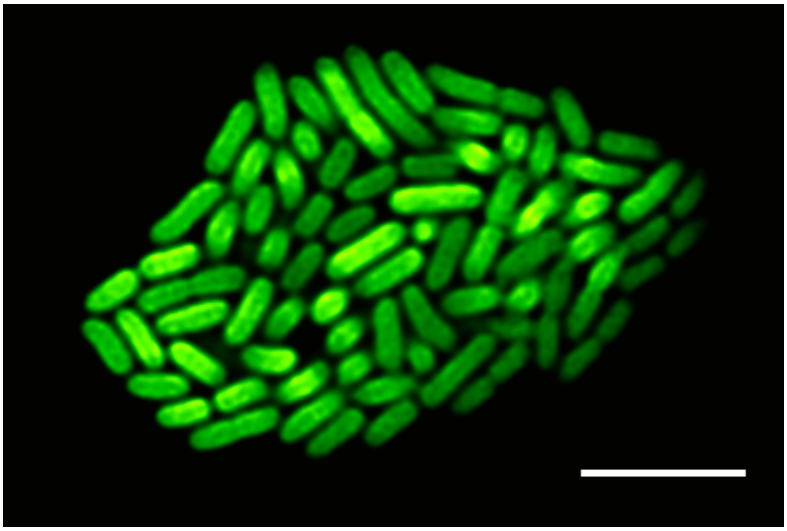

Figure A.1: Supplementary Movie for Figure 4.7 (p. 44). Bacterial colony grown on 2 % M9 agarose, deconvolved using measured point spread function (Figure 4.6, p. 43). Individual bacteria are clearly distinguishable in the xy projection, as in the case of the raw confocal stacks. The distinction between bacteria in the axial direction is greatly enhanced. Despite some bacteria appearing to be merged together due to the deconvolution, the points of local maxima (used to locate the backbone for the bacterium) are far more clearly separated than in the case of the raw confocal stack. Scale bar is 5.0 µm.

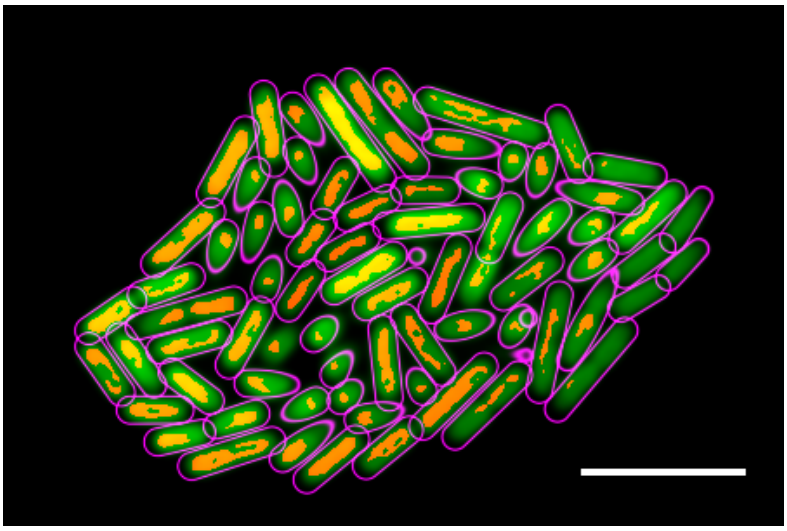

Figure A.2: Supplementary Movie for Figure 4.8 (p. 46). Reconstruction output of a bacterial colony grown on 2 % M9 agarose which has been deconvolved using the measured PSF (Figure 4.6, p. 43). The code successfully identifies two layers of bacteria fitting backbones (yellow) to the local maxima within each bacteria (green) before fitting a spherocylinder outline (purple) to each. Despite the apparent merging of bacteria (seen in Figure 4.7) the code successfully distinguishes all bacteria in recognisable form. Scale bar is 5.0 µm.

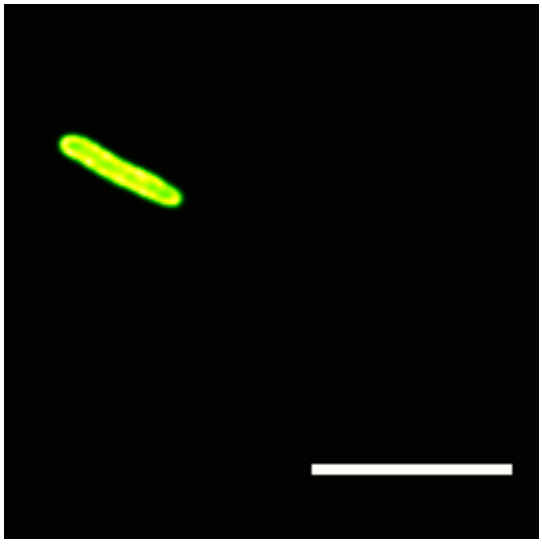

Figure A.3: Supplementary Movie for Figure 4.9 (p. 48). Time-lapse confocal microscopy image of a bacterial colony grown on 3 % M9 agarose. Stacks are recorded every 5 min showing 2D growth of the colony. Study of the images reveals some bacteria exhibit deviation from the normal spherocylinder geometry. Scale bar is 5.0 µm.

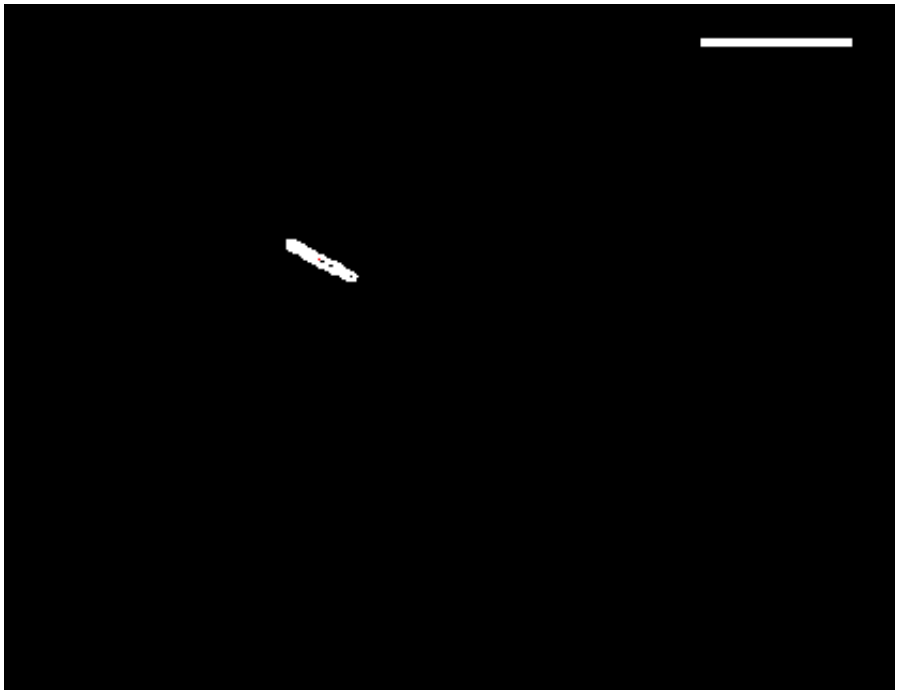

Figure A.4: Supplementary Movie for Figure 4.11 (p. 50). Code developed by Dario Miroli, fitting directly to the outline of the bacterium rather than fitting a spherocylinder. The code successfully identifies the deviation from a straight line. Red lines show the historical position of individual bacteria within the colony. Scale bar is 5.0 µm.

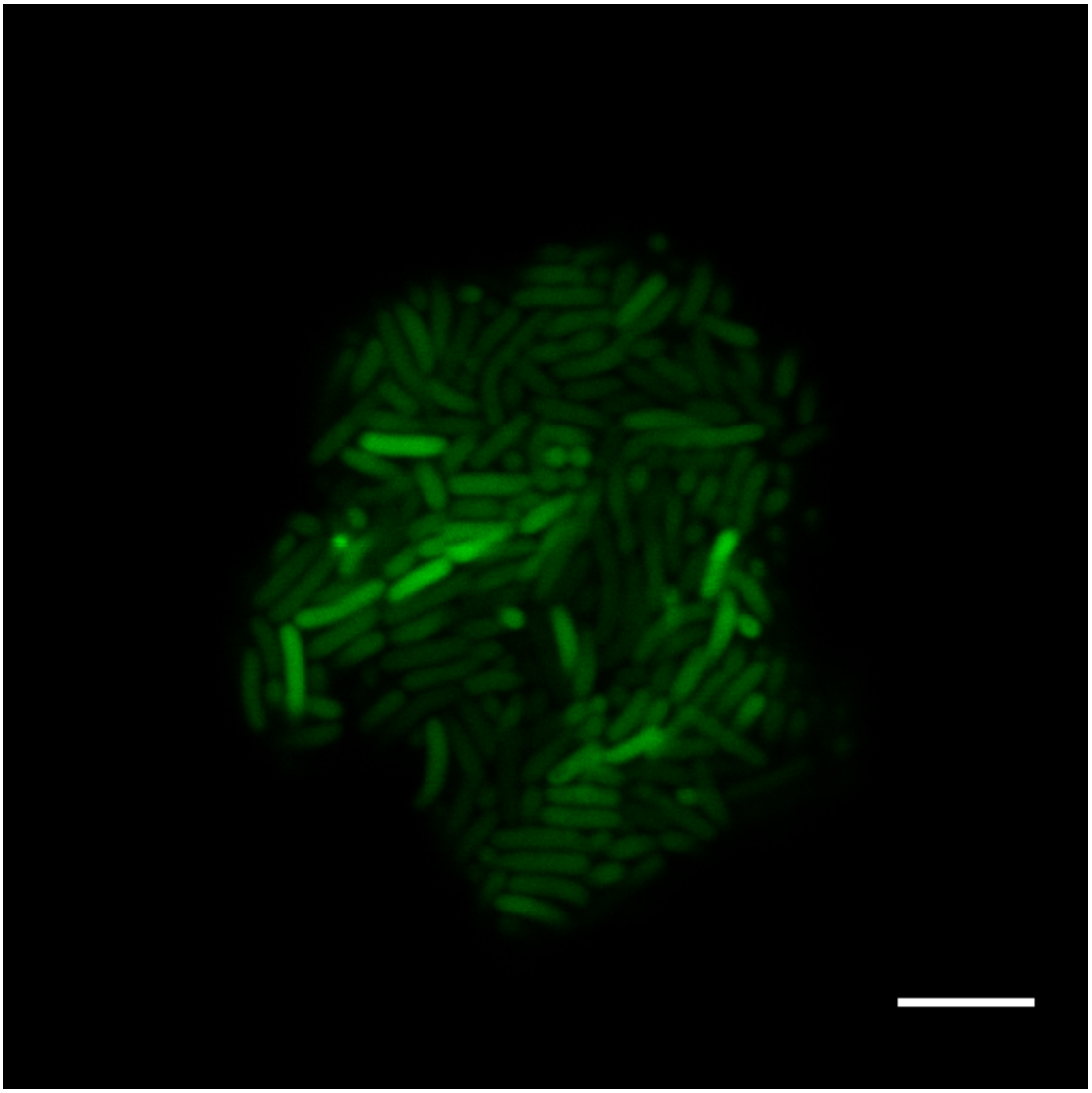

Figure A.5: Supplementary Movie for Figure 4.12 (p. 52). A single *E. coli* MG1655 bacterial colony grown fully submerged within 2 % M9 agarose gel. Individual bacteria are distinguishable throughout the colony, even when imaging through multiple layers of bacteria, which are highly divergent media. Colonies such as these have been successfully reconstructed using code [111] (Supp. Movie A.7), as with the surface bacterial colonies showing the possibility of the extension of the method to investigating fully 3D systems. Scale bar is 5.0 µm.

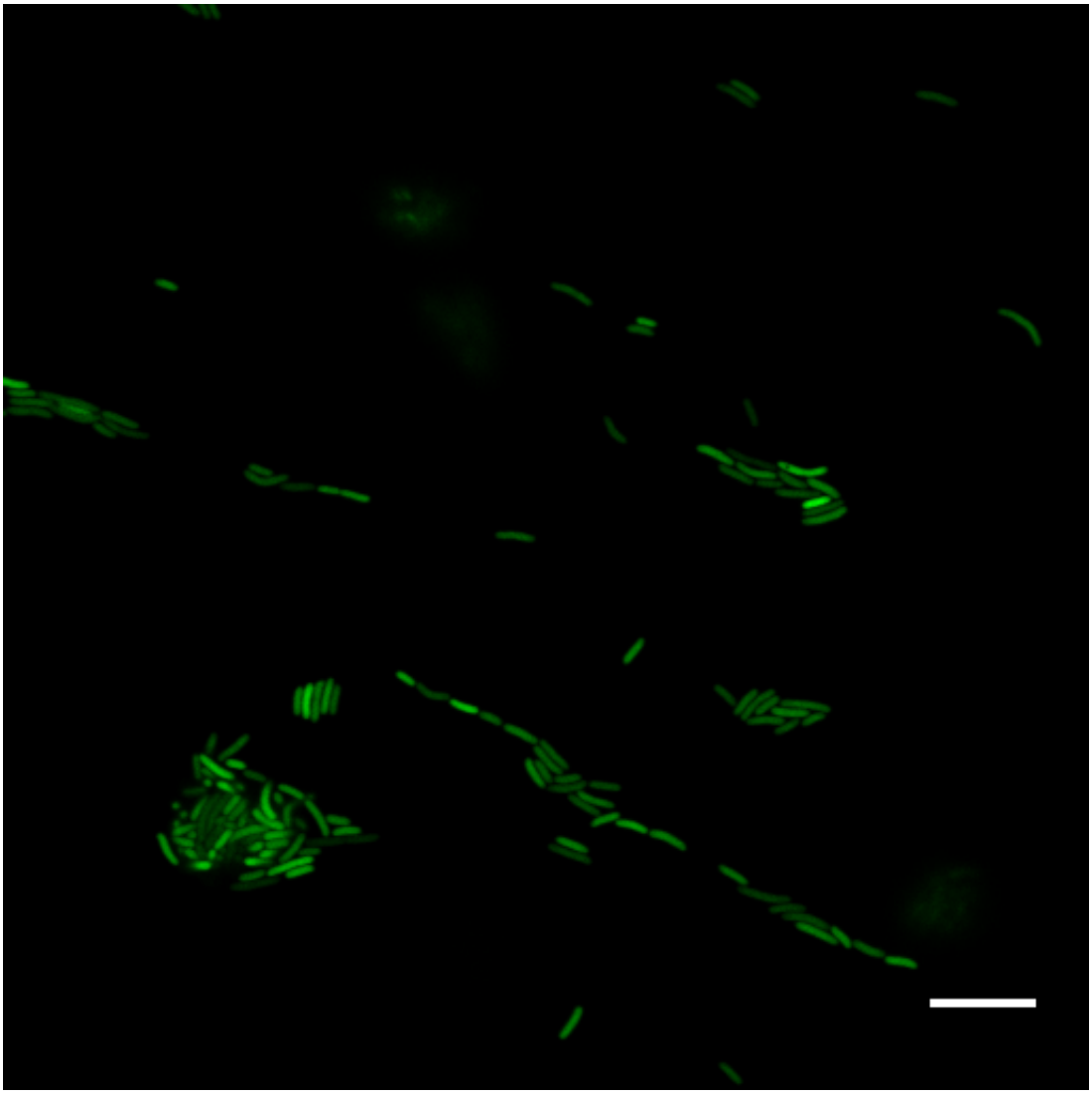

Figure A.6: Supplementary Movie for Figure 4.13 (p. 53). *E. coli* MG1655 bacterial colonies grown fully submerged in 2 % M9 agarose gel. Individual bacteria present on the surface of the agarose are seen to grow in chains, whilst those submerged in the agarose have formed spherical colonies. Individual bacteria are distinguishable within each colony. Scale bar is 10.0 µm.

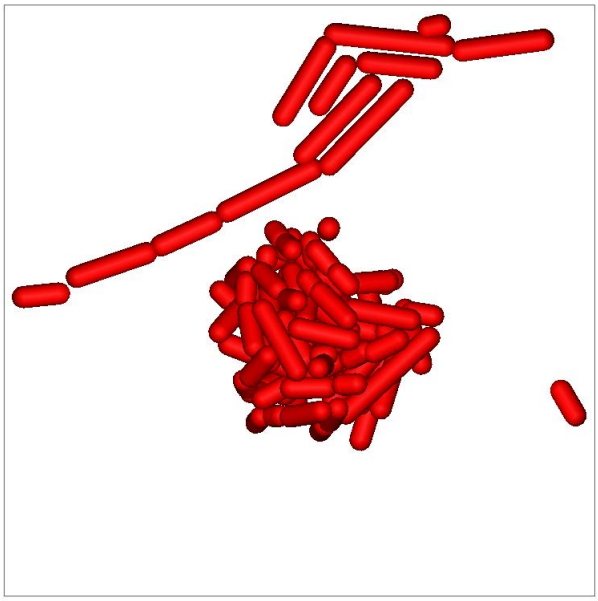

Figure A.7: Supplementary Movie for Figure 4.14 (p. 55). Reconstruction of fully submerged bacterial colony buried in 2 % (weight) M9 agarose. The reconstruction is formed using software developed by Michiel Hermes to visualise the output from his reconstruction code [111] used within this thesis. Bacteria are clearly distinguishable on a single bacterial resolution. The bacteria form a spherical colony and are seen to be submerged below the surface of the agarose (identifiable by the linear bacteria structure visible in the frames). No clear bias can be seen for the growth of the bacterial colony in any direction in this case.

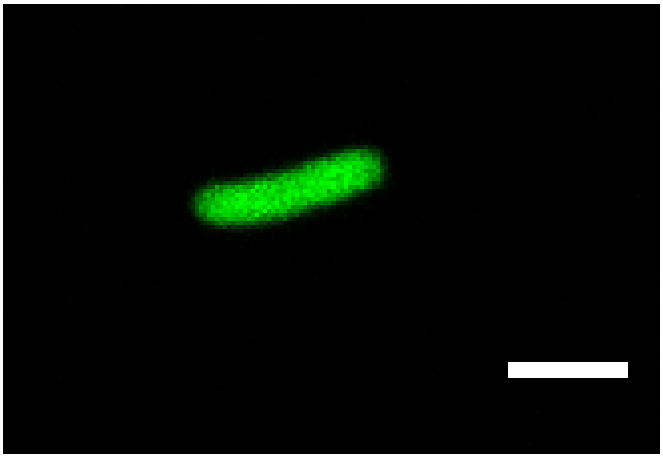

Figure A.8: Supplementary Movie for Figure 5.9 (p. 67). The growth of a single bacterium on M9 agarose at a weight concentration of 3 %. Stacks through the sample are acquired every 2 min. The bacterium is seen to approximately double in size from initial conditions until the point where the division occurs. Scale bar is 2.0 µm.

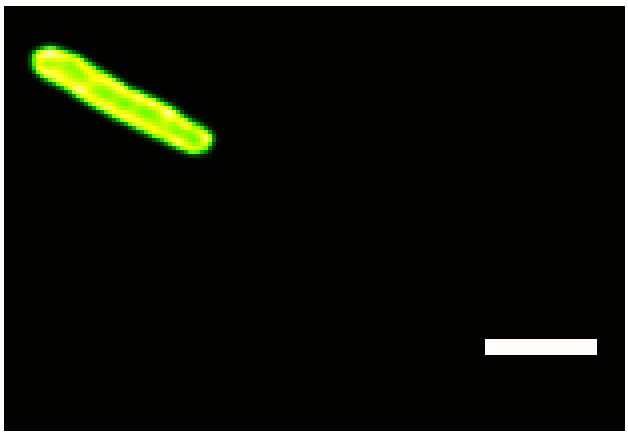

Figure A.9: Supplementary Movie for Figure 6.4 (p. 81). Bacterial colony growth from seed bacterium to first division (generation 2) on 2 % M9 agarose gel. Stacks of images are recorded every 5 min. The bacterium grows in the long axis in a 2D plane along the surface of the agarose before dividing to produce two daughter bacteria. Scale is 2.0 µm

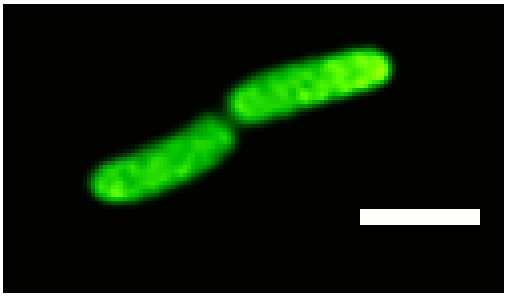

Figure A.10: Supplementary Movie for Figure 6.11 (p. 88). Bacterial growth of *E. coli* MG1655 with pcH60 GFP plasmid growing on 2 % (weight) M9 agarose surface. Images are taken every 2 min. The colony is seen to grow in a 2D plane along the surface of the agarose. After the initial division, the two bacteria are seen to push past each other searching for space to grow into from the newly formed poles in the centre. Similarly, as the third generation forms, the bacteria push past each other to form a two-by-two matrix as observed by Su *et al.* [46]. Scale bar is 2.0 µm.

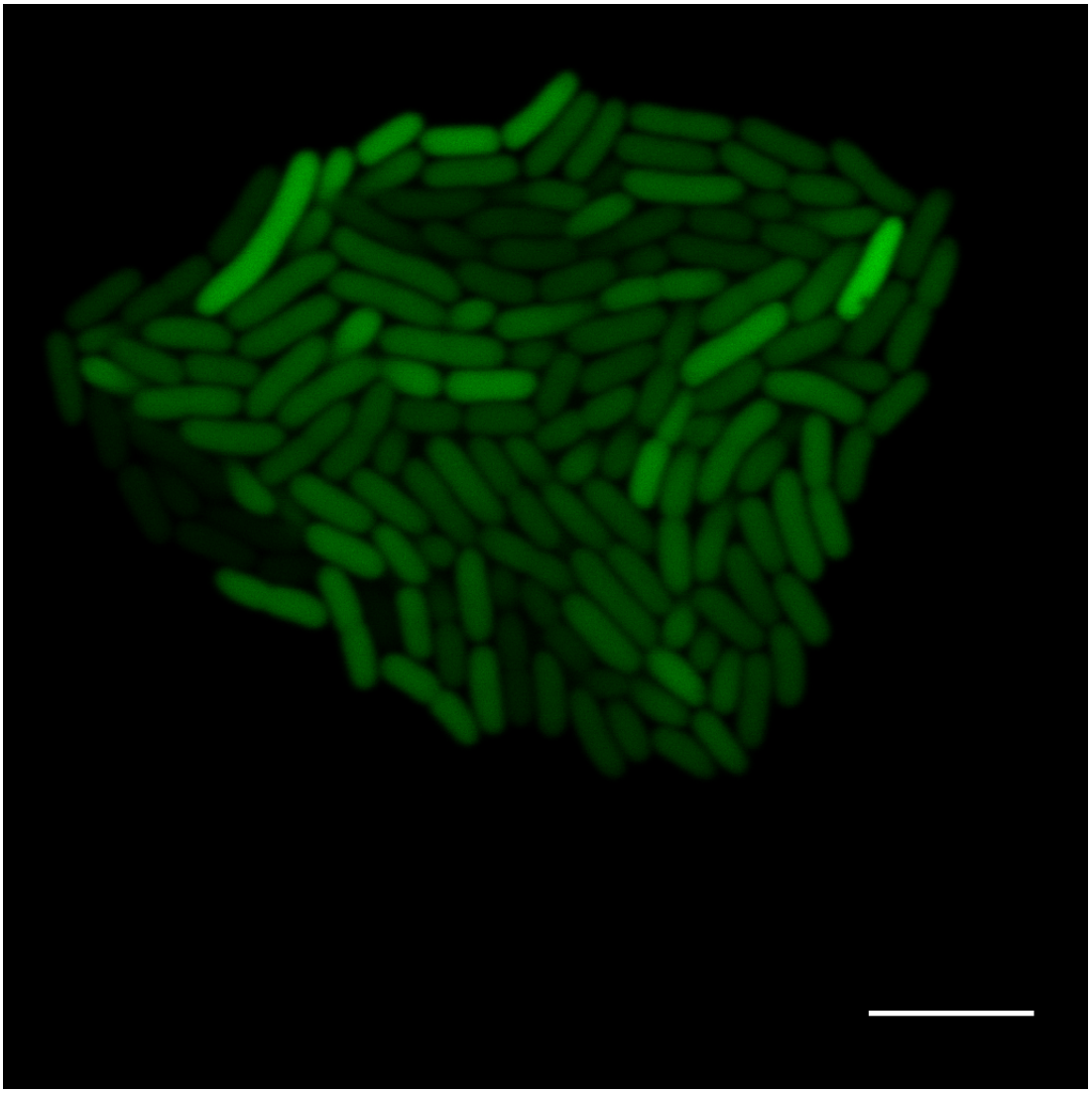

Figure A.11: Supplementary Movie for Figure 6.15 (p. 92). Raw confocal stack of an *E. coli* MG1655 with pcH60 GFP bacterial colony grown on 3 % (weight) M9 agarose after additional layer generation. Images are taken through the colony at 0.1 µm slices in the axial direction. Scale bar is 5.0 µm.

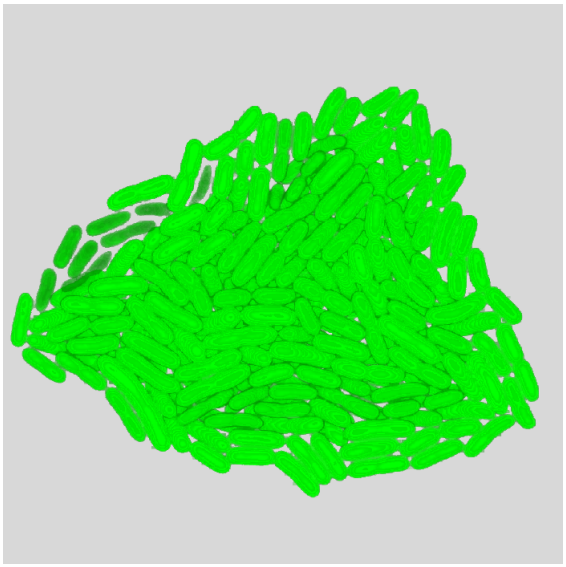

Figure A.12: Supplementary Movie for Figure 6.15 (p. 92). 3D reconstruction of *E. coli* MG1655 with pcH60 GFP plasmid bacterial colony grown on 3 % M9 agarose surface at single cell resolution after 24 hr. Additional to the initial growth layer, two distinct layers of bacteria are seen submerged in the agarose, with all bacteria in the colony distinguishable. The darker bacteria visible in the top left initially are the result of loss of fluorescence experienced over 24 hr imaging of the colony.

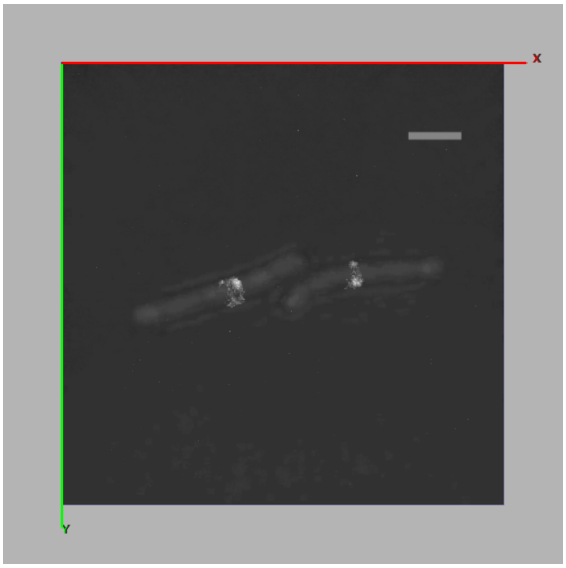

Figure A.13: 3D rendering of FtsZ rings in *E. coli* grown on M9 with 2 % agarose concentrations. The transmitted PMT image of the bacteria on the agarose surface is overlaid on the YFP-fluorescence in the xy plane. The 3D stack of images showing the YFP-fluorescence clearly shows two ring structures forming at the approximate midcell of both bacteria, with one exhibiting a double ring and the other a part helix structure. 3D movies are produced by loading confocal stacks of the YFP-FtsZ into Vaa3D [178]. Scale bar is 2.0 µm.

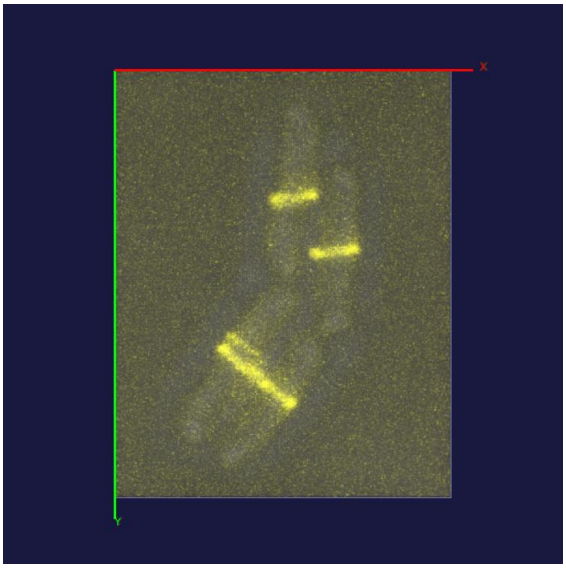

Figure A.14: 3D rendering of FtsZ rings in a microcolony of *E. coli* grown on M9 with 2 % agarose concentrations. Transmitted PMT images of the bacteria (grey scale) are overlaid with the YFP expression (yellow) showing clear ring structures forming at the midcell of the bacteria. 3D movies are produced by loading confocal stacks of the YFP-FtsZ into Vaa3D [178].

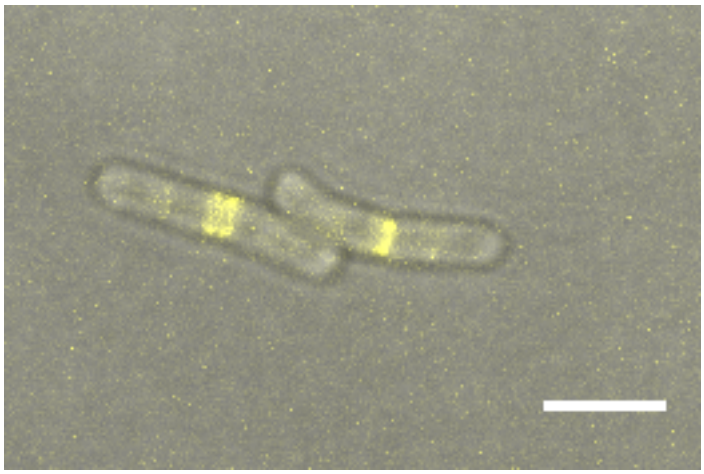

Figure A.15: FtsZ ring formation and disruption in *E. coli* grown on 2 % (weight) M9 agarose. Transmitted PMT (grey scale) images are overlaid with YFP (yellow) showing the position of concentrations of FtsZ proteins within the bacteria. The ring is seen to form and instigate septation in the bacterium before disbanding to create an apparent double ring or small helix, before transferring to another site within both the daughter bacteria at approximately the midcell. Stacks of images were recorded every 5 min providing suitable time resolution to resolve the process of disruption of the Z ring in the bacterium. Scale bar is 2.0 µm.

Appendix B

M9 growth media protocol

M9 media is used in these experiments due to the low autofluorescence generated by the constituents of the media. The media is nutrient rich and ensures the samples are not limited by external food sources whilst experiments are undertaken.

Below is the protocol followed for preparation of both liquid and agarose M9 media

M9 liquid media protocol

Preparation of M9 media must be conducted in sterile conditions.

To make 100 ml of M9 media

- Pour 71.79 ml of de-ionised & distilled (d.d.) water into a sterile 250 ml bottle
- Add 25 ml of 4× M9 Salts
- Autoclave sample at temperature greater than 100 °C for 15 min[1]
- Place in warm water bath at 50 °C for 15 min
- Add 200 µl of 1M $MgSO_4$
- Add 2 ml of 20 % glucose
- Add 10 ml of 1M $CaCl_2$ (A precipitate may form but shake the bottle for this to be dissolved in solution)
- Allow to cool and store at room temperature

[1] The entire autoclaving process takes longer than 15 min. 15 min refers to the time the samples must spend at a temperature of 100 °C or greater. Remember to loosen lids of bottles to ensure pressure equilibrium.

M9 agarose media protocol

Preparation of M9 media must be conducted in sterile conditions.

To make 100 ml of M9 media

- Pour 71.79 ml of de-ionised & distilled (d.d.) water into a sterile 250 ml bottle
- Add 25 ml of 4× M9 Salts
- Add agarose at the required weight percent concentration (for 2 % agarose 2 g of agarose is required)
- Autoclave sample at temperature greater than 100 °C for 15 min
- Place in warm water bath at 50 °C for 15 min
- Add 200 µl of 1M $MgSO_4$
- Add 2 ml of 20 % glucose
- Add 10 µl of 1M $CaCl_2$ (A precipitate may form but shake the bottle for this to be dissolved in solution
- Decant the agarose in 2 ml parts into falcon tubes for use in the experiments

The agarose must then be heated again to just above the melting point before being placed onto the microscope slide.

Appendix C

M9 media preparation for AFM experiments

The protocol for preparation of agarose samples for atomic force microscopy (AFM) experiments is outlined below.

Equipment

- M9 media made to correct agarose concentrations
- Waterbath
- 1000 µl Pipette
- 1000 µl Pipette Tips
- AFM Petri dishes
- Hotplate
- Tinfoil

Protocol

Preparation of agarose should be conducted as for all other experiments of colony growth (Appendix B). After introduction of the glucose, $CaCl_2$ and $MgSO_4$ the agarose media (bulk store) should be placed again into the water bath set to a temperature of 80 °C.

The hot plate should be switched on and heated to a temperature of 90 °C. A piece of

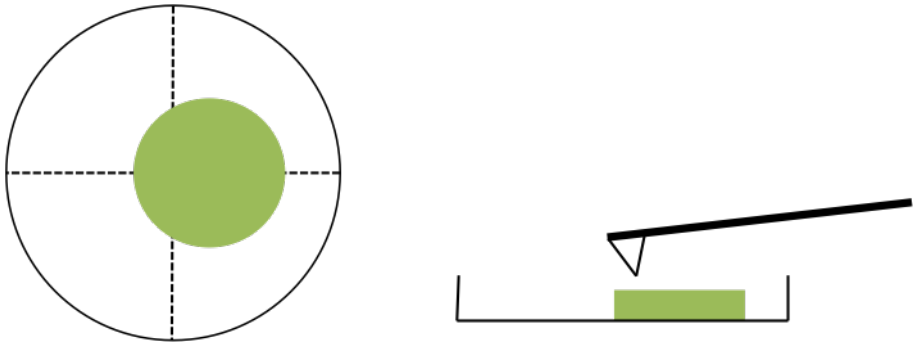

Figure C.1: Schematic showing position of agarose (green) on the petri dish for AFM measurements in xy (left) and xz (right) profile. The agarose should be positioned off centre on the petri dish in order to allow easy transfer between the agarose surface and the plastic (used as a rigid calibration surface).

tinfoil should be placed onto the hot plate and onto this place the AFM petri dish for the sample.

500 µl of M9 agarose at desired concentration should be removed from the bulk store and pipetted into the petri dish. The agarose should then be spread around the petri dish in order to produce a very thin layer of agarose in the centre of the petri dish. **NB the agarose layer should not cover the entire petri dish as a solid surface is needed next to the sample in order to provide a calibration of the AFM tip used. Best practice is to place the agarose off centre in the petri dish so that easy transfer between the agarose and the plastic surface can be achieved (Figure C.1)**.

The petri dish should be removed from the hot plate and allowed to cool on the desk. Once solidified, the pad must be covered with d.d.H_2O in order to reduce the effect of surface tension between the AFM tip and the sample. It will also limit the effect of drying of the sample to the measurements. The sample is then ready for measurements using AFM.

Appendix D

Young's modulus measurements of agarose

Measurements of the Young's modulus of agarose vary dramatically depending on the method used for measurement and on the geometry of the mechanism used to measure the sample. In this appendix I outline literature measurements of the Young's modulus for agarose gels.

D.1 Young's modulus

Table D.1 outlines methods used to measure the Young's modulus of agarose gels at different concentrations.

Sample	Conc_n (%)	Method	Stress (kPa)	Study
Agarose	1 %	Microindentation (diameter 2 mm)	13 ± 2	[182]
		OCT-ball indentation (diameter 1 mm)	12 ± 1	[182]
		Indentation (diameter 2 mm)	13 ± 1	[183]
		Indentation (diameter 4 mm)	17 ± 0.25	[183]
		Indentation (diameter 80 µm)	100 ± 10	[184]
Agarose	2 %	Compression (0 days)	16 ± 1	[185]
		Compression (14 days)	8 ± 1	
		Compression (28 days)	14 ± 3	
		Microindentation (diameter 3 mm)	48 ± 4	[182]

		Indentation (cylindrical punch)	$35 - 54$	[186]
		Indentation (diameter 80 µm)	350 ± 50	[184]
Agarose	3 %	Indentation (cylindrical punch)	52	[187]
Agarose	5 %	Indentation (diameter 80 µm)	700 ± 100	[184]
		Nanoindentation (tip 10 µm)	550 ± 75	[188]
		Nanoindentation (tip 50 µm)	1050 ± 50	
		Nanoindentation (tip 100 µm)	825 ± 50	
		Nanoindentation (tip 800 µm)	875 ± 100	

Table D.1: Young's modulus measurements of agarose gels at concentrations from 1 % to 5 % using different techniques. The measurements are very wide-ranging & dependent upon the method used and the geometry of the probe.

The measurements of the Young's modulus are very dependent upon the method used as well as the geometry of the probe.

D.2 AFM measurements of Young's modulus

Atomic force microscopy (AFM) measurements are similarly dependent upon the geometry of the probe used to investigate the surface. Table D.2 summarises measurements in literature of the Young's modulus when using different probe geometries and sizes.

Sample	Conc_n (%)	Tip Size	Stress (kPa)	Study
PVA gel	1 %	Sharp tip	> 30	[189]
		2 µm bead	3.1 ± 0.1	
		5 µm bead	3.7 ± 0.4	
	1.6 %	Sharp tip	8.2 ± 1.3	
		2 µm bead	5.2 ± 0.8	
		5 µm bead	5.4 ± 0.9	
	1.9 %	Sharp tip	24.9 ± 0.5	
		2 µm bead	9.4 ± 0.1	
		5 µm bead	8.8 ± 0.6	
	3.3 %	Sharp tip	76.1 ± 3.7	
		2 µm bead	24.2 ± 2.0	
		5 µm bead	19.4 ± 3.1	

Agarose	1 %	2 µm sphere	979 ± 45	[190]
			936 ± 95	
			1315 ± 57	
	1.5 %	Pyramid tip	9.8 ± 1.5	[191]
		10 µm sphere	3.7 ± 1.8	
	2 %	4 µm	52 ± 10	[192]
	2.5 %	Pyramid tip	22 ± 2	[193]
		5 µm sphere	36 ± 5	
	3 %	Pyramid tip	26.3 ± 4.2	[191]
		10 µm sphere	28.1 ± 6.7	

Table D.2: Young's modulus measurements of agarose gels made using atomic force microscopy (AFM). The measurements are heavily dependent upon the geometry of the sample.

Again the difference between measurements is dramatic with values varying over more than an order of magnitude.

Bibliography

[1] J. E. Sulston, E. Schierenberg, J. G. White, and J. N. Thomson. The embryonic cell lineage of the nematode Caenorhabditis elegans. *Developmental biology*, 100(1):64–119, 1983.

[2] W. B. Whitman, D. C. Coleman, and W. J. Wiebe. Prokaryotes: the unseen majority. *Proceedings of the National Academy of Sciences of the United States of America*, 95(12):6578–6583, 1998.

[3] Alys Jepson, Vincent A. Martinez, Jana Schwarz-Linek, Alexander Morozov, and Wilson C K Poon. Enhanced diffusion of nonswimmers in a three-dimensional bath of motile bacteria. *Physical Review E - Statistical, Nonlinear, and Soft Matter Physics*, 88(4), 2013.

[4] Amit Rabani, Gil Ariel, and Avraham Be'er. Collective motion of spherical bacteria. *PLoS ONE*, 8(12), 2013.

[5] Kimberly K. Jefferson. What drives bacteria to produce a biofilm? *FEMS Microbiology Letters*, 236(2):163–173, July 2004.

[6] James K. Fredrickson, John M. Zachara, David L. Balkwill, David Kennedy, Shu Mei W. Li, Heather M. Kostandarithes, Michael J. Daly, Margaret F. Romine, and Fred J. Brockman. Geomicrobiology of high-level nuclear waste-contaminated vadose sediments at the Hanford Site, Washington State. *Applied and Environmental Microbiology*, 70(7):4230–4241, 2004.

[7] Karen Olsson-Francis and Charles S. Cockell. Experimental methods for studying microbial survival in extraterrestrial environments. *Journal of Microbiological Methods*, 80(1):1–13, 2010.

[8] M. J. Willis, T. J. Ahrens, L. E. Bertani, and C. Z. Nash. Bugbuster-survivability of living bacteria upon shock compression. *Earth and Planetary Science Letters*, 247(3-4):185–196, 2006.

[9] Sophie L. Nixon, Claire R. Cousins, and Charles S. Cockell. Plausible microbial metabolisms on Mars. *Astronomy and Geophysics*, 54(1):13–16, 2013.

[10] M. B. Miller and B. L. Bassler. Quorum sensing in bacteria. *Annual review of microbiology*, 55:165–199, 2001.

[11] Wai-Leung Ng and Bonnie L. Bassler. Bacterial quorum-sensing network architectures. *Annual review of genetics*, 43:197–222, 2009.

[12] R. E. Kunkee. Selection and modification of yeasts and lactic acid bacteria for wine fermentation. *Food Microbiology*, 1(4):315–332, 1984.

[13] Aline Lonvaud-Funel. Lactic acid bacteria in the quality improvement and depreciation of wine. In *Antonie van Leeuwenhoek, International Journal of General and Molecular Microbiology*, volume 76, pages 317–331, 1999.

[14] L. Monfredini, L. Settanni, E. Poznanski, A. Cavazza, and E. Franciosi. The spatial distribution of bacteria in Grana-cheese during ripening. *Systematic and Applied Microbiology*, 35(1):54–63, 2012.

[15] A. R. Hill. Yoghurt Science and Technology. *Food Research International*, 33(9):807, 2000.

[16] S. Sarkar. Effect of probiotics on biotechnological characteristics of yoghurt: A review. *British Food Journal*, 110(7):717–740, 2008.

[17] Brian A. Federici. Insecticidal bacteria: An overwhelming success for invertebrate pathology. In *Journal of Invertebrate Pathology*, volume 89, pages 30–38, 2005.

[18] Julian R. Marchesi. Human distal gut microbiome, 2011.

[19] Jean Guy LeBlanc, Christian Milani, Graciela Savoy de Giori, Fernando Sesma, Douwe van Sinderen, and Marco Ventura. Bacteria as vitamin suppliers to their host: A gut microbiota perspective. *Current Opinion in Biotechnology*, 24(2):160–168, 2013.

[20] Yehuda Cohen. Bioremediation of oil by marine microbial mats, 2002.

[21] Luiz Carlos Martins Das Neves, Tábata Taemi Miazaki Ohara Miyamura, Dante Augusto Moraes, Thereza Christina Vessoni Penna, and Attilio Converti. Biofiltration methods for the removal of phenolic residues. *Applied biochemistry and biotechnology*, 129-132:130–152, 2006.

[22] Andreas Liese and Murillo Villela Filho. Production of fine chemicals using biocatalysis. *Current Opinion in Biotechnology*, 10(6):595–603, 1999.

[23] Elizabeth Pennisi. Leaf bacteria fertilize trees, researchers claim. *Science*, 348(6237):844–845, May 2015.

[24] A. K. Vidaver and P. A. Lambrecht. Bacteria as plant pathogens. *The Plant Health Instructor*, 2004.

[25] G. H. K. Lawson. Pathogenesis of bacterial infections in animals, 1988.

[26] Robert H. Mak and Huey-Ju Kuo. Pathogenesis of urinary tract infection: an update. *Current opinion in pediatrics*, 18(2):148–152, 2006.

[27] J. W. Costerton, P. S. Stewart, and E. P. Greenberg. Bacterial biofilms: a common cause of persistent infections. *Science (New York, N.Y.)*, 284(5418):1318–1322, 1999.

[28] Hans-Curt Flemming and Jost Wingender. The biofilm matrix. *Nature reviews. Microbiology*, 8(9):623–33, September 2010.

[29] Sara Reardon. Antibiotic resistance sweeping developing world. *Nature News*, 509(7499):141–142, 2014.

[30] Hilary Cadman and Lindsay Martinez. Antimicrobial Resistance; Global Report on Surveillance. Technical report, World Health Organization, Geneva, 2014.

[31] Paula Watnick and Roberto Kolter. Biofilm, city of microbes. *Journal of Bacteriology*, 182(10):2675–2679, 2000.

[32] George A. O'Toole and Roberto Kolter. Flagellar and twitching motility are necessary for Pseudomonas aeruginosa biofilm development. *Molecular Microbiology*, 30(2):295–304, 1998.

[33] Leslie A. Pratt and Roberto Kolter. Genetic analysis of Escherichia coli biofilm formation: Roles of flagella, motility, chemotaxis and type I pili. *Molecular Microbiology*, 30(2):285–293, 1998.

[34] Bo Song and Laura G. Leff. Influence of magnesium ions on biofilm formation by Pseudomonas fluorescens. *Microbiological research*, 161(4):355–61, January 2006.

[35] Danial N. Hohne, John G. Younger, and Michael J. Solomon. Flexible microfluidic device for mechanical property characterization of soft viscoelastic solids such as bacterial biofilms. *Langmuir : the ACS journal of surfaces and colloids*, 25(13):7743–51, July 2009.

[36] Thomas R. Neu, Bertram Manz, Frank Volke, James J. Dynes, Adam P. Hitchcock, and John R. Lawrence. Advanced imaging techniques for assessment of structure, composition and function in biofilm systems. *FEMS Microbiology Ecology*, 72(1):1–21, 2010.

[37] Joe J Harrison, Howard Ceri, Jerome Yerly, Carol A Stremick, Yaoping Hu, Robert Martinuzzi, and Raymond J Turner. The use of microscopy and three-dimensional visualization to evaluate the structure of microbial biofilms cultivated in the Calgary Biofilm Device. *Biological procedures online*, 8:194–215, 2006.

[38] Ranganathan Vasudevan. Biofilms : Microbial Cities of Scientific Significance. *Journal of Microbiology & Experimentation*, 1(3):1–16, 2014.

[39] M .E. Davey and G. A. O'Toole. Microbial biofilms: from ecology to molecular genetics. *Microbiology and molecular biology reviews : MMBR*, 64(4):847–867, 2000.

[40] J. R. Lawrence, D. R. Korber, B. D. Hoyle, J. W. Costerton, and D. E. Caldwell. Optical sectioning of microbial biofilms. *Journal of Bacteriology*, 173(20):6558–6567, October 1991.

[41] Janus A. J. Haagensen, Birgitte Regenberg, and Claus Sternberg. Advanced microscopy of microbial cells. *Advances in biochemical engineering/biotechnology*, 124(November 2010):21–54, January 2011.

[42] A. Bridier, T. Meylheuc, and R. Briandet. Realistic representation of Bacillus subtilis biofilms architecture using combined microscopy (CLSM, ESEM and FESEM). *Micron (Oxford, England : 1993)*, 48:65–9, May 2013.

[43] Tim Tolker-Nielsen and Claus Sternberg. Methods for studying biofilm formation: flow cells and confocal laser scanning microscopy. *Methods in molecular biology (Clifton, N.J.)*, 1149:615–29, January 2014.

[44] D. E. Caldwell, D. R. Korber, and J. R. Lawrence. Analysis of biofilm formation using 2D vs 3D digital imaging. *Journal of Applied Microbiology*, 74:52S—-66S, June 1993.

[45] M. A. Lakins, J. L. Marrison, P. J. O'Toole, and M. W. van der Woude. Exploiting advances in imaging technology to study biofilms by applying multiphoton laser scanning microscopy as an imaging and manipulation tool. *Journal of microscopy*, 235(2):128–37, August 2009.

[46] Pin-Tzu Su, Pei-Wen Yen, Shao-Hung Wang, Chi-Hung Lin, Arthur Chiou, and Wan-Jr Syu. Factors affecting daughter cells' arrangement during the early bacterial divisions. *PloS one*, 5(2):e9147, January 2010.

[47] Pin-Tzu Su, Chih-Tang Liao, Jiunn-Ren Roan, Shao-Hung Wang, Arthur Chiou, and Wan-Jr Syu. Bacterial colony from two-dimensional division to three-dimensional development. *PloS one*, 7(11):e48098, January 2012.

[48] Matthew A A Grant, Bartomiej Wacaw, Rosalind J Allen, and Pietro Cicuta. The role of mechanical forces in the planar-to-bulk transition in growing Escherichia coli microcolonies. *Journal of the Royal Society, Interface / the Royal Society*, 11(97):20140400, August 2014.

[49] Veysel Berk, Jiunn C. N. Fong, Graham T. Dempsey, Omer N. Develioglu, Xiaowei Zhuang, Jan Liphardt, Fitnat H. Yildiz, and Steven Chu. Molecular architecture and assembly principles of Vibrio cholerae biofilms. *Science (New York, N.Y.)*, 337(6091):236–9, July 2012.

[50] Eric J. Stewart, Richard Madden, Gregory Paul, and Franc Taddei. Aging and death in an organism that reproduces by morphologically symmetric division. *PLoS Biology*, 3(2):0295–0300, 2005.

[51] A. McVey and J. Crain. Nonlinear optical methods for cellular imaging and localization. *Methods (San Diego, Calif.)*, 68(2):371–377, April 2014.

[52] K. S. Stowe. *An introduction to thermodynamics and statistical mechanics*. Cambridge University Press, 2nd edition, 2007.

[53] Franz Mandl. *Statistical Physics*. John Wiley & Sons, 3rd edition, 2013.

[54] J. W. Strutt. Some General Theorems relating to Vibrations. *Proceedings of the London Mathematical Society*, s1-4(1):357–368, 1871.

[55] Lars Onsager. Reciprocal relations in irreversible processes. I. *Physical Review*, 37(4):405–426, 1931.

[56] David M. Thomasson, Ahmed Gharib, and King C. P. Li. A primer on molecular biology for imagers: VIII. Equipment for imaging molecular processes. *Academic Radiology*, 11(10):1159–1170, 2004.

[57] Wei Ning Lee, Christopher M. Ingrassia, Simon D. Fung-Kee-Fung, Kevin D. Costa, Jeffrey W. Holmes, and Elisa E. Konofagou. Theoretical quality assessment of myocardial elastography with in vivo validation. *IEEE Transactions on Ultrasonics, Ferroelectrics, and Frequency Control*, 54(11):2233–2245, 2007.

[58] Xiaowei S. Liu, Paul Sajda, Punam K. Saha, Felix W. Wehrli, and X. Edward Guo. Quantification of the roles of trabecular microarchitecture and trabecular type in determining the elastic modulus of human trabecular bone. *Journal of bone and mineral research : the official journal of the American Society for Bone and Mineral Research*, 21(10):1608–1617, 2006.

[59] Felix W. Wehrli, Mary B. Leonard, Punam K. Saha, and Bryon R. Gomberg. Quantitative high-resolution magnetic resonance imaging reveals structural implications of renal osteodystrophy on trabecular and cortical bone. *Journal of magnetic resonance imaging : JMRI*, 20(1):83–89, 2004.

[60] Robia G. Pautler and Scott E. Fraser. The year(s) of the contrast agent - Micro-MRI in the new millennium. *Current Opinion in Immunology*, 15(4):385–392, 2003.

[61] C Muhr, M Bergström, P O Lundberg, K Bergström, P Hartvig, H Lundqvist, G Antoni, and B Långström. Dopamine receptors in pituitary adenomas: PET visualization with 11C-N-methylspiperone. *Journal of computer assisted tomography*, 10(2):175–180, 1986.

[62] M. Piert, T. T. Zittel, G. A. Becker, M. Jahn, A. Stahlschmidt, G. Maier, H. J. Machulla, and R. Bares. Assessment of porcine bone metabolism by dynamic. *Journal of nuclear medicine : official publication, Society of Nuclear Medicine*, 42(7):1091–1100, 2001.

[63] G. M. Blake, S. J. Park-Holohan, G. J. Cook, and I. Fogelman. Quantitative studies of bone with the use of 18F-fluoride and 99mTc-methylene diphosphonate. *Seminars in nuclear medicine*, 31(1):28–49, 2001.

[64] C. J. Anderson, F. Dehdashti, P. D. Cutler, S. W. Schwarz, R. Laforest, L. A. Bass, J. S. Lewis, and D. W. McCarthy. 64Cu-TETA-octreotide as a PET imaging agent for patients with neuroendocrine tumors. *Journal of nuclear medicine : official publication, Society of Nuclear Medicine*, 42(2):213–221, 2001.

[65] Armen R. Kherlopian, Ting Song, Qi Duan, Mathew A. Neimark, Ming J. Po, John K. Gohagan, and Andrew F. Laine. A review of imaging techniques for systems biology. *BMC systems biology*, 2:74, 2008.

[66] Sang-June Park, W. Leslie Rogers, Sam Huh, Harris Kagan, Klaus Honscheid, Don Burdette, Enrico Chesi, Carlos Lacasta, Gabriela Llosa, Marko Mikuz, Andrej Studen, Peter Weilhammer, and Neal H. Clinthorne. A prototype of very high resolution small animal PET scanner using silicon pad detectors. *Nuclear instruments & methods in physics research. Section A, Accelerators, spectrometers, detectors and associated equipment*, 570(3):543–555, 2007.

[67] Vilma Gabbay, David A. Hess, Songtao Liu, James S. Babb, Rachel G. Klein, and Oded Gonen. Lateralized caudate metabolic abnormalities in adolescent major depressive disorder: A proton MR spectroscopy study. *American Journal of Psychiatry*, 164(12):1881–1889, 2007.

[68] Klaus Strobel, Joerg van den Hoff, and Jens Pietzsch. Localized proton magnetic resonance spectroscopy of lipids in adipose tissue at high spatial resolution in mice in vivo. *Journal of lipid research*, 49(2):473–480, 2008.

[69] Nikolaus Kriegeskorte and Peter Bandettini. Analyzing for information, not activation, to exploit high-resolution fMRI. *NeuroImage*, 38(4):649–662, 2007.

[70] L. Ciobanu and C. H. Pennington. 3D micron-scale MRI of single biological cells. *Solid State Nuclear Magnetic Resonance*, 25(1-3):138–141, 2004.

[71] Y. Meng, C. C. Shaw, X. Liu, M. C. Altunbas, T. Wang, L. Chen, S. J. Tu, S. C. Kappadath, and C. J. Lai. Comparison of two detector systems for cone beam CT small animal imaging - a preliminary study. *Proc Soc Photo Opt Instrum Eng*, 6142:nihpa21188, 2006.

[72] Ralph Weissleder. Scaling down imaging: molecular mapping of cancer in mice. *Nature reviews. Cancer*, 2(1):11–18, 2002.

[73] E. I. Tocheva, Z. Li, and G. J. Jensen. Electron Cryotomography. *Cold Spring Harbor Perspectives in Biology*, 2(6):a003442–a003442, 2010.

[74] Zoya V. Leonenko, Eric Finot, and David T. Cramb. Atomic force microscopy to study interacting forces in phospholipid bilayers containing general anesthetics. *Methods in molecular biology (Clifton, N.J.)*, 400:601–609, 2007.

[75] Y. R. Shen. Surface properties probed by second-harmonic and sum-frequency generation, February 1989.

[76] Martin Oheim, Darren J. Michael, Matthias Geisbauer, Dorte Madsen, and Robert H. Chow. Principles of two-photon excitation fluorescence microscopy and other nonlinear imaging approaches. *Advanced drug delivery reviews*, 58(7):788–808, September 2006.

[77] Andreas Zumbusch, Gary R. Holtom, and X. Sunney Xie. Three-Dimensional Vibrational Imaging by Coherent Anti-Stokes Raman Scattering. *Physical Review Letters*, 82(20):4142–4145, May 1999.

[78] Marvin Minsky. Memoir on Inventing the Confocal Scanning Microscope. *Scanning*, 10:128–138, 1988.

[79] M Minsky. Microscopy Apparatus, 1961.

[80] W. B. Amos and J. G. White. How the Confocal Laser Scanning Microscope entered Biological Research. *Biology of the Cell*, 95(6):335–342, September 2003.

[81] Steve Paddock. Over the rainbow: 25 years of confocal imaging. *BioTechniques*, 44(5):643–4, 646, 648, April 2008.

[82] Guy Cox. Biological confocal microscopy. *Materials Today*, 5(3):34–41, April 2002.

[83] John M. Murray, Paul L. Appleton, Jason R. Swedlow, and Jennifer C. Waters. Evaluating performance in three-dimensional fluorescence microscopy. *Journal of microscopy*, 228(Pt 3):390–405, December 2007.

[84] Jeff W. Lichtman and José-Angel Conchello. Fluorescence microscopy. *Nature methods*, 2(12):910–919, 2005.

[85] Jonathan W. Young, James C. W. Locke, Alphan Altinok, Nitzan Rosenfeld, Tigran Bacarian, Peter S. Swain, Eric Mjolsness, and Michael B. Elowitz. Measuring single-cell gene expression dynamics in bacteria using fluorescence time-lapse microscopy. *Nature protocols*, 7(1):80–8, January 2012.

[86] Jerome Mertz. Confocal Microscopy. In *Introduction to Confocal Microscopy*, chapter 14. Roberts and Company Publishers, Boston University, 2009.

[87] T. Wilson and A. R Carlini. Three-dimensional imaging in confocal imaging systems with finite sized detectors. *Journal of Microscopy*, 149(1):51–66, 1988.

[88] Renliang Xu. Light scattering: A review of particle characterization applications, 2014.

[89] Fritjof Helmchen and Winfried Denk. Deep tissue two-photon microscopy. *Nature methods*, 2(12):932–40, December 2005.

[90] V. E. Centonze and J. G. White. Multiphoton excitation provides optical sections from deeper within scattering specimens than confocal imaging. *Biophysical Journal*, 75(4):2015–2024, October 1998.

[91] Diarmuid Padraig Lloyd. *Microscopic studies of surface growing bacterial populations.* PhD thesis, The University of Edinburgh, 2014.

[92] J. Sambrook and D. W. Russel. *Molecular Cloning: A Laboratory Manual, Volume 3.* Cold Spring Harbour, Laboratory Press, Cold Spring, New York, 2001.

[93] F. R. Blattner, G. Plunkett, C. A. Bloch, N. T. Perna, V. Burland, M. Riley, J. Collado-Vides, J. D. Glasner, C. K. Rode, G. F. Mayhew, J. Gregor, N. W. Davis, H. A. Kirkpatrick, M. A. Goeden, D. J. Rose, B. Mau, and Y. Shao. The complete genome sequence of Escherichia coli K-12. *Science (New York, N.Y.)*, 277(5331):1453–1462, 1997.

[94] Hai Ping Cheng and Graham C. Walker. Succinoglycan is required for initiation and elongation of infection threads during nodulation of alfalfa by Rhizobium meliloti. *Journal of Bacteriology*, 180(19):5183–5191, 1998.

[95] J Sambrook, E F Fritsch, and T Maniatis. *Molecular Cloning: A Laboratory Manual.* Cold Spring Harbour, Laboratory Press, Cold Spring, 1989.

[96] Ivy F. Lau, Sergio R. Filipe, Britta Søballe, Ole-Andreas Økstad, Francois-Xavier Barre, and David J. Sherratt. Spatial and temporal organization of replicating Escherichia coli chromosomes. *Molecular Microbiology*, 49(3):731–743, January 2004.

[97] Jaroslaw M. Boberek, Jem Stach, and Liam Good. Genetic evidence for inhibition of bacterial division protein FtsZ by berberine. *PloS one*, 5(10):e13745, January 2010.

[98] Robert Schleif. AraC protein, regulation of the l-arabinose operon in Escherichia coli, and the light switch mechanism of AraC action. *FEMS microbiology reviews*, 34(5):779–96, September 2010.

[99] Tasha A. Desai and Christopher V. Rao. Regulation of arabinose and xylose metabolism in Escherichia coli. *Applied and Environmental Microbiology*, 76(5):1524–1532, 2010.

[100] Kevin D. Young. The selective value of bacterial shape. *Microbiology and molecular biology reviews : MMBR*, 70(3):660–703, September 2006.

[101] Teuta Pilizota and Joshua W. Shaevitz. Fast, multiphase volume adaptation to hyperosmotic shock by Escherichia coli. *PloS one*, 7(4):e35205, January 2012.

[102] OpenWetWare. E. coli genotypes - OpenWetWare, 2014.

[103] Yu-Zhong Zhang and David Carter. Multicolor Fluorescent Microspheres as Calibration Standards for Confocal Laser Scanning Microscopy. *Applied Immunohistochemistry & Molecular Morphology*, 7(2):156–163, 1999.

[104] Vijay Narayan, Narayanan Menon, and Sriram Ramaswamy. Nonequilibrium steady states in a vibrated-rod monolayer: tetratic, nematic, and smectic correlations. *Journal of Statistical Mechanics: Theory and Experiment*, 2006(01):P01005–P01005, January 2006.

[105] W. S. Rasband. ImageJ. *U. S. National Institutes of Health, Bethesda, Maryland, USA*, page //imagej.nih.gov/ij/, 2012.

[106] Caroline A Schneider, Wayne S Rasband, and Kevin W Eliceiri. NIH Image to ImageJ: 25 years of image analysis. *Nature Methods*, 9(7):671–675, June 2012.

[107] Kai Uwe Barthel. Volume Viewer, ImageJ Plugin, 2005.

[108] Benjamin Schmid. 3D Viewer, ImageJ Plugin, 2007.

[109] Michael Doube, Micha M. Kosowski, Ignacio Arganda-Carreras, Fabrice P. Cordelières, Robert P. Dougherty, Jonathan S. Jackson, Benjamin Schmid, John R. Hutchinson, and Sandra J. Shefelbine. BoneJ: Free and extensible bone image analysis in ImageJ. *Bone*, 47(6):1076–9, December 2010.

[110] Philippe Andrey and Thomas Boudier. 3D Processing and Analysis with ImageJ e, 2015.

[111] T. H. Besseling, M. Hermes, A. Kuijk, B. de Nijs, T. S. Deng, M. Dijkstra, A. Imhof, and A. van Blaaderen. Determination of the positions and orientations of concentrated rod-like colloids from 3D microscopy data. June 2014.

[112] W. D. Donachie and K. J. Begg. Growth of the Bacterial Cell. *Nature*, 227(5264):1220–1224, September 1970.

[113] Shanika A. Crusz, Roman Popat, Morten Theil Rybtke, Miguel Cámara, Michael Givskov, Tim Tolker-Nielsen, Stephen P. Diggle, and Paul Williams. Bursting the bubble on bacterial biofilms: a flow cell methodology. *Biofouling*, 28(8):835–42, January 2012.

[114] Sattar Taheri-Araghi, Serena Bradde, John T. Sauls, Norbert S. Hill, Petra Anne Levin, Johan Paulsson, Massimo Vergassola, and Suckjoon Jun. Cell-Size Control and Homeostasis in Bacteria. *Current Biology*, 25(3):385–391, 2015.

[115] Shoji Takeuchi, Willow R DiLuzio, Douglas B Weibel, and George M Whitesides. Controlling the shape of filamentous cells of Escherichia coli. *Nano Letters*, 5(9):1819–23, September 2005.

[116] Galina Reshes, Sharon Vanounou, Itzhak Fishov, and Mario Feingold. Cell shape dynamics in Escherichia coli. *Biophysical journal*, 94(1):251–64, January 2008.

[117] Ranjan Mukhopadhyay and Ned Wingreen. Curvature and shape determination of growing bacteria. *Physical Review E*, 80(6):062901, December 2009.

[118] Joshua W Shaevitz and Daniel A Fletcher. Enhanced three-dimensional deconvolution microscopy using a measured depth-varying point-spread function. *Journal of the Optical Society of America. A, Optics, image science, and vision*, 24(9):2622–2627, 2007.

[119] J. Crocker and D. Grier. Methods of Digital Video Microscopy for Colloidal Studies. *Journal of Colloid and Interface Science*, 179(179):298–310, 1996.

[120] F. J. Trueba and C. L. Woldringh. Changes in cell diameter during the division cycle of Escherichia coli. *Journal of Bacteriology*, 142(3):869–78, 1980.

[121] O. Pierucci. Dimensions of Escherichia coli at various growth rates : model for envelope growth . *Journal of bacteriology*, 135(2):559–574, 1978.

[122] Willem P. Van De Merwe, József Czégé, Merrill E. Milham, and Burt V. Bronk. Rapid optically based measurements of diameter and length for spherical or rod-shaped bacteria in vivo. *Applied optics*, 43(28):5295–5302, 2004.

[123] Ana Margarida Sousa, Idalina Machado, Ana Nicolau, and Maria Olívia Pereira. Improvements on colony morphology identification towards bacterial profiling. *Journal of Microbiological Methods*, 95(3):327–335, 2013.

[124] Robert Bucki, Jennifer J. Pastore, Paramjeet Randhawa, Rolands Vegners, Daniel J. Weiner, and Paul A. Janmey. Antibacterial Activities of Rhodamine B-Conjugated Gelsolin-Derived Peptides Compared to Those of the Antimicrobial Peptides Cathelicidin LL37, Magainin II, and Melittin. *Antimicrobial Agents and Chemotherapy*, 48:1526–1533, 2004.

[125] G. Ya. Wiederschain. *The Molecular Probes handbook. A guide to fluorescent probes and labeling technologies*, volume 76. 2011.

[126] E. Geissler and A. M. Hecht. The Poisson ratio in polymer gels. *Macromolecules*, 13:1276–1280, 1980.

[127] Hannah H. Tuson, George K. Auer, Lars D. Renner, Mariko Hasebe, Carolina Tropini, Max Salick, Wendy C. Crone, Ajay Gopinathan, Kerwyn Casey Huang, and Douglas B. Weibel. Measuring the stiffness of bacterial cells from growth rates in hydrogels of tunable elasticity. *Molecular microbiology*, 84(5):874–91, June 2012.

[128] L. Mignot and G. A. Junter. Diffusion in immobilized-cell agar layers: influence of bacterial growth on the diffusivity of potassium chloride. *Applied microbiology and biotechnology*, 33:167–171, 1990.

[129] C. Odin, J. P. Aimé, Z. El Kaakour, and T. Bouhacina. Tip's finite size effects on atomic force microscopy in the contact mode: simple geometrical considerations for rapid estimation of apex radius and tip angle based on the study of polystyrene latex balls. *Surface Science*, 317:321–340, 1994.

[130] T. Neumann. Determining the elastic modulus of biological samples using atomic force microscopy. *JPK Instruments Application Report*, pages 1–9, 2008.

[131] C. O. Gill and N. Penney. Penetration of bacteria into meat. *Applied and Environmental Microbiology*, 33:1284–1285, 1977.

[132] P. D. Marsh. Dental plaque as a microbial biofilm. In *Caries Research*, volume 38, pages 204–211, 2004.

[133] Hannah H. Tuson and Douglas B. Weibel. Bacteriasurface interactions. *Soft Matter*, 9(18):4368, 2013.

[134] Rodney M. Donlan. Biofilms: Microbial life on surfaces, 2002.

[135] K. Vickery, A. Deva, A. Jacombs, J. Allan, P. Valente, and I. B. Gosbell. Presence of biofilm containing viable multiresistant organisms despite terminal cleaning on clinical surfaces in an intensive care unit. *Journal of Hospital Infection*, 80:52–55, 2012.

[136] Martin Gardner. Mathematical Games, 1971.

[137] Jeffrey R. Moffitt, Jeffrey B. Lee, and Philippe Cluzel. The single-cell chemostat: an agarose-based, microfluidic device for high-throughput, single-cell studies of bacteria and bacterial communities. *Lab on a Chip*, 12(8):1487, 2012.

[138] E. F. Bi and J. Lutkenhaus. FtsZ ring structure associated with division in Escherichia coli. *Nature*, 354(6349):161–4, November 1991.

[139] Joe Lutkenhaus. Assembly dynamics of the bacterial MinCDE system and spatial regulation of the Z ring. *Annual review of biochemistry*, 76:539–62, January 2007.

[140] David W. Adams and Jeff Errington. Bacterial cell division: assembly, maintenance and disassembly of the Z ring. *Nature reviews. Microbiology*, 7(9):642–53, September 2009.

[141] Lawrence Rothfield, Aziz Taghbalout, and Yu-Ling Shih. Spatial control of bacterial division-site placement. *Nature reviews. Microbiology*, 3(12):959–68, December 2005.

[142] Harold P. Erickson, David E. Anderson, and Masaki Osawa. FtsZ in bacterial cytokinesis: cytoskeleton and force generator all in one. *Microbiology and molecular biology reviews : MMBR*, 74(4):504–28, December 2010.

[143] Jen Hsin, Ajay Gopinathan, and Kerwyn C. Huang. Nucleotide-dependent conformations of FtsZ dimers and force generation observed through molecular dynamics simulations. *Proceedings of the National Academy of Sciences of the United States of America*, 109(24):9432–7, June 2012.

[144] Sigal Ben-Yehuda and Richard Losick. Asymmetric Cell Division in B. subtilis Involves a Spiral-like Intermediate of the Cytokinetic Protein FtsZ. *Cell*, 109(2):257–266, April 2002.

[145] Swapna Thanedar and William Margolin. FtsZ exhibits rapid movement and oscillation waves in helix-like patterns in Escherichia coli. *Current biology : CB*, 14(13):1167–73, July 2004.

[146] William Margolin. Bacterial division: another way to box in the ring. *Current biology : CB*, 16(20):R881–4, October 2006.

[147] Phoebe C. Peters, Margaret D. Migocki, Carola Thoni, and Elizabeth J. Harry. A new assembly pathway for the cytokinetic Z ring from a dynamic helical structure in vegetatively growing cells of Bacillus subtilis. *Molecular microbiology*, 64(2):487–99, April 2007.

[148] Phoebe C. Jennings, Guy C. Cox, Leigh G. Monahan, and Elizabeth J. Harry. Super-resolution imaging of the bacterial cytokinetic protein FtsZ. *Micron (Oxford, England : 1993)*, 42(4):336–41, June 2011.

[149] Tristan S. Ursell, Jeffrey Nguyen, Russell D. Monds, Alexandre Colavin, Gabriel Billings, Nikolay Ouzounov, Zemer Gitai, Joshua W. Shaevitz, and Kerwyn Casey Huang. Rod-like bacterial shape is maintained by feedback between cell curvature and cytoskeletal localization. *Proceedings of the National Academy of Sciences of the United States of America*, 111(11):E1025–34, March 2014.

[150] Matthew T. Swulius and Grant J. Jensen. The helical mreb cytoskeleton in Escherichia coli MC1000/pLE7 is an artifact of the N-terminal yellow fluorescent protein tag. *Journal of Bacteriology*, 194(23):6382–6386, 2012.

[151] Julie S. Biteen, Michael A. Thompson, Nicole K. Tselentis, Lucy Shapiro, and W. E. Moerner. Superresolution imaging in live Caulobacter crescentus cells using photoswitchable enhanced yellow fluorescent protein. *Proceedings of SPIE*, 7185:71850I1–11, 2009.

[152] Philipp V. Olshausen, Hervé Joël Defeu Soufo, Kai Wicker, Rainer Heintzmann, Peter L. Graumann, and Alexander Rohrbach. Superresolution imaging of dynamic MreB filaments in B. subtilis - A multiple-motor-driven transport? *Biophysical Journal*, 105(5):1171–1181, 2013.

[153] Arnaud Chastanet. The actin-like MreB proteins in Bacillus subtilis: a new turn, 2012.

[154] Steven S. Andrews and Adam P. Arkin. A mechanical explanation for cytoskeletal rings and helices in bacteria. *Biophysical journal*, 93(6):1872–84, September 2007.

[155] Dj Scheffers and Mg Pinho. Bacterial cell wall synthesis: new insights from localization studies. *Microbiology and Molecular Biology Reviews*, 69(4):585–607, 2005.

[156] Elisabeth Fischer-Friedrich, Benjamin M. Friedrich, and Nir S. Gov. FtsZ rings and helices: physical mechanisms for the dynamic alignment of biopolymers in rod-shaped bacteria. *Physical biology*, 9(1):016009, February 2012.

[157] Jay K. Fisher, Aude Bourniquel, Guillaume Witz, Beth Weiner, Mara Prentiss, and Nancy Kleckner. Four-dimensional imaging of E. coli nucleoid organization and dynamics in living cells. *Cell*, 153(4):882–95, May 2013.

[158] Andrew K. Fenton and Kenn Gerdes. Direct interaction of FtsZ and MreB is required for septum synthesis and cell division in Escherichia coli. *The EMBO journal*, 32(13):1953–65, July 2013.

[159] Xuan-Chuan Yu and William Margolin. FtsZ ring clusters in Min and partition mutants: role of both the Min system and the nucleoid in regulating FtsZ ring localization. *Molecular Microbiology*, 32(2):315–326, April 1999.

[160] Gitte Ebersbach, Elisa Galli, Jakob Møller-Jensen, Jan Löwe, and Kenn Gerdes. Novel coiled-coil cell division factor ZapB stimulates Z ring assembly and cell division. *Molecular microbiology*, 68(3):720–35, May 2008.

[161] Frank J. Trueba. On the precision and accuracy achieved by Escherichia coli cells at fission about their middle. *Archives of Microbiology*, 131(1):55–59, February 1982.

[162] Jonathan M. Guberman, Allison Fay, Jonathan Dworkin, Ned S. Wingreen, and Zemer Gitai. PSICIC: noise and asymmetry in bacterial division revealed by computational image analysis at sub-pixel resolution. *PLoS computational biology*, 4(11):e1000233, November 2008.

[163] Abhishekh Gupta, Jason Lloyd-Price, Samuel M. D. Oliveira, Olli Yli-Harja, Anantha-Barathi Muthukrishnan, and Andre S. Ribeiro. Robustness of the division symmetry in Escherichia coli and functional consequences of symmetry breaking. *Physical biology*, 11(6):066005, December 2014.

[164] Margaret D. Migocki, Marcelle K. Freeman, R. Gerry Wake, and Elizabeth J. Harry. The Min system is not required for precise placement of the midcell Z ring in Bacillus subtilis. *EMBO reports*, 3(12):1163–7, December 2002.

[165] Christoph Spahn, Ulrike Endesfelder, and Mike Heilemann. Super-resolution imaging of Escherichia coli nucleoids reveals highly structured and asymmetric segregation during fast growth. *Journal of structural biology*, 185(3):243–9, March 2014.

[166] Paolo Natale, Manuel Pazos, and Miguel Vicente. The Escherichia coli divisome: born to divide. *Environmental microbiology*, 15(12):3169–82, December 2013.

[167] Filipe Tostevin, Pieter Rein ten Wolde, and Martin Howard. Fundamental limits to position determination by concentration gradients. *PLoS computational biology*, 3(4):e78, April 2007.

[168] Martin Howard and Andrew Rutenberg. Pattern Formation inside Bacteria: Fluctuations due to the Low Copy Number of Proteins. *Physical Review Letters*, 90(12):128102, March 2003.

[169] J. Pla, M. Sanchez, P. Patacios, M. Vicente, and M. Aldea. Preferential cytoplasmic location of FtsZ, a protein essential for Escherichia coli septation. *Molecular Microbiology*, 5(7):1681–1686, July 1991.

[170] S. Rueda, M. Vicente, and J. Mingorance. Concentration and Assembly of the Division Ring Proteins FtsZ, FtsA, and ZipA during the Escherichia coli Cell Cycle. *Journal of Bacteriology*, 185(11):3344–3351, June 2003.

[171] Chunlin Lu, Jesse Stricker, and Harold P Erickson. FtsZ from Escherichia coli, Azotobacter vinelandii, and Thermotoga maritima–quantitation, GTP hydrolysis, and assembly. *Cell motility and the cytoskeleton*, 40(1):71–86, January 1998.

[172] P. A. de Boer, R. E. Crossley, Arthur R. Hand, and Lawrence I. Rothfield. The MinD protein is a membrane ATPase required for the correct placement of the Escherichia coli division site. *The EMBO journal*, 10(13):4371–80, December 1991.

[173] Yu-ling Shih, Xiaoli Fu, Glenn F. King, Trung Le, and Lawrence Rothfield. Division site placement in E.coli: mutations that prevent formation of the MinE ring lead to loss of the normal midcell arrest of growth of polar MinD membrane domains. *The EMBO journal*, 21(13):3347–57, July 2002.

[174] Joe Lutkenhaus. Min Oscillation in Bacteria. In Miguel Marato and Nick Monk, editors, *Cellular Oscillatory Mechanisms*, chapter 4, pages 49–61. Springer, 2008.

[175] Yasushi Ishihama, Thorsten Schmidt, Juri Rappsilber, Matthias Mann, F Ulrich Hartl, Michael J Kerner, and Dmitrij Frishman. Protein abundance profiling of the Escherichia coli cytosol. *BMC genomics*, 9:102, January 2008.

[176] J. E. Peters, T. E. Thate, and N. L. Craig. Definition of the Escherichia coli MC4100 Genome by Use of a DNA Array. *Journal of Bacteriology*, 185(6):2017–2021, March 2003.

[177] Thomas Ferenci, Zhemin Zhou, Thu Betteridge, Yan Ren, Yu Liu, Lu Feng, Peter R. Reeves, and Lei Wang. Genomic sequencing reveals regulatory mutations and recombinational events in the widely used MC4100 lineage of Escherichia coli K-12. *Journal of bacteriology*, 191(12):4025–9, June 2009.

[178] Hanchuan Peng, Zongcai Ruan, Fuhui Long, Julie H. Simpson, and Eugene W. Myers. V3D enables real-time 3D visualization and quantitative analysis of large-scale biological image data sets. *Nature biotechnology*, 28:348–353, 2010.

[179] D. M. Raskin and P. A. de Boer. Rapid pole-to-pole oscillation of a protein required for directing division to the middle of Escherichia coli. *Proceedings of the National Academy of Sciences of the United States of America*, 96(9):4971–6, April 1999.

[180] L. Shapiro, H. H. McAdams, and R. Losick. Why and how bacteria localize proteins. *Science (New York, N.Y.)*, 326(5957):1225–1228, 2009.

[181] Jeffery Errington. Dynamic proteins and a cytoskeleton in bacteria. *Nature cell biology*, 5(3):175–178, 2003.

[182] Ying Yang, Pierre O. Bagnaninchi, Mark Ahearne, Ruikang K. Wang, and Kuo-Kang Liu. A novel optical coherence tomography-based micro-indentation technique for mechanical characterization of hydrogels. *Journal of the Royal Society, Interface / the Royal Society*, 4(17):1169–73, December 2007.

[183] M. Ahearne, Y. Yang, and K-k. Liu. Mechanical Characterisation of Hydrogels for Tissue Engineering Applications. In N. Ashammakhi, R. Reis, and F. Chiellini, editors, *Topics in Tissue Engineering*, chapter 12. 4 edition, 2008.

[184] V. T. Nayar, J. D. Weiland, C. S. Nelson, and A. M. Hodge. Elastic and viscoelastic characterization of agar. *Journal of the mechanical behavior of biomedical materials*, 7:60–8, March 2012.

[185] Hani A. Awad, M. Quinn Wickham, Holly A. Leddy, Jeffrey M. Gimble, and Farshid Guilak. Chondrogenic differentiation of adipose-derived adult stem cells in agarose, alginate, and gelatin scaffolds. *Biomaterials*, 25(16):3211–22, July 2004.

[186] Malcolm C. Bourne. Method for obtaining compression and shear coefficients of food using cylindrical punches. *Journal of Texture Studies*, 5(4):459–469, January 1975.

[187] K. A. Ross and M. G. Scanlon. Analysis of the elastic modulus of agar gel by indentation. *Journal of Texture Studies*, 30(1):17–27, May 1999.

[188] D. M. Ebenstein and L. A. Pruitt. Nanoindentation of soft hydrated materials for application to vascular tissues. *Journal of biomedical materials research. Part A*, 69(2):222–32, May 2004.

[189] Emilios K. Dimitriadis, Ferenc Horkay, Julia Maresca, Bechara Kachar, and Richard S. Chadwick. Determination of elastic moduli of thin layers of soft material using the atomic force microscope. *Biophysical journal*, 82(5):2798–810, May 2002.

[190] S. Tripathy and E. J. Berger. Measuring viscoelasticity of soft samples using atomic force microscopy. *Journal of biomechanical engineering*, 131(9):094507, September 2009.

[191] KD Costa, MMY Ho, and CT Hung. Multi-scale measurement of mechanical properties of soft samples with atomic force microscopy. *Summer Bioengineering Conference*, page 2, 2003.

[192] Marco Salerno, Silvia Dante, Niranjan Patra, and Alberto Diaspro. AFM measurement of the stiffness of layers of agarose gel patterned with polylysine. *Microscopy research and technique*, 73(10):982–90, October 2010.

[193] Martin Stolz, Roberto Raiteri, A. U. Daniels, Mark R. Van Landingham, Werner Baschong, and Ueli Aebi. Dynamic elastic modulus of porcine articular cartilage determined at two different levels of tissue organization by indentation-type atomic force microscopy. *Biophysical journal*, 86(5):3269–83, May 2004.